UNIVERSITY COLLEGE LONDON

Modelling Colloidal Particles Adsorbed at Fluid-Fluid Interfaces

by

Gary Bryan Davies

A thesis submitted in partial fulfillment for the degree of Doctor of Philosophy

in the

Faculty of Mathematical and Physical Sciences

Department of Chemistry

June 2015

Declaration of Authorship

I, Gary Davies, declare that this thesis titled, 'Modelling Colloidal Particles Adsorbed at Fluid-Fluid Interfaces' and the work presented in it are my own. I confirm that:

- This work was done wholly or mainly while in candidature for a research degree at this University.
- Where any part of this thesis has previously been submitted for a degree or any other qualification at this University or any other institution, this has been clearly stated.
- Where I have consulted the published work of others, this is always clearly attributed.
- Where I have quoted from the work of others, the source is always given. With the exception of such quotations, this thesis is entirely my own work.
- I have acknowledged all main sources of help.
- Where the thesis is based on work done by myself jointly with others, I have made clear exactly what was done by others and what I have contributed myself.

Signed: _____

Date: _____

Abstract

This thesis concerns the modelling of the interactions between colloidal particles and fluid-fluid interfaces. Colloidal particles – micrometre to nanometre sized solid particles – adsorb strongly at fluid-fluid interfaces because they reduce energetically costly fluid-fluid interface area. Once adsorbed at an interface, colloidal particles interact via various physical forces. One such type of interaction, capillary interactions, emerge because particles deform the fluid-fluid interface leading to excess interface area. The particles minimise this excess interface area by overlapping their respective interface deformations.

In this thesis we develop a new theoretical model describing the detachment energy of prolate and oblate ellipsoidal particles from fluid-fluid interfaces. In so doing, we verify a lattice Boltzmann based numerical method and confirm that it is a powerful tool for modelling emulsions.

We investigate the rotation of magnetic prolate spheroidal particles at fluid-fluid interfaces by applying an external magnetic field directed normal to the interface. The particles experience a torque attempting to align them with the external field, but surface tension resists this rotation. Consequently, the particles tilt with respect to the interface. We show that during tilting, the particles deform the interface in a dipolar manner, providing an experimental realisation of a long sought-after capillary interaction mode. We further confirm a predicted first-order phase transition with respect to the particle's orientation as a function of the dipole-field strength.

Finally, we utilise these induced dipolar capillary interactions to assemble ellipsoidal particles at fluid-fluid interfaces, and investigate the structures they form. We show that the capillary interactions and the resulting structure formation can be tuned by varying the dipole-field strength, providing one of the first realisations of truly tunable capillary interactions. Additionally, we show that by exploiting the first-order phase transition, we can switch the capillary interactions on and off by causing the particles to flip from a tilted state to a vertical state in which interface deformations and hence capillary interactions disappear.

Our results have implications for the directed assembly of colloidal particles at fluid-fluid interfaces and for the creation of novel, reconfigurable materials composed of colloidal particles.

Acknowledgements

There are two people to whom I owe the successful completion of this thesis more than any others: Jens Harting and Timm Krüger. Jens took me under his wing at the beginning of my PhD, introducing me to the LB3D simulation code that I used in this thesis and giving me several interesting physics problems to work on, one of which ended up as essentially my first publication. In the end I spent around 4 months of my time visiting his group in Eindhoven. During my PhD he was a constant source of support, advice, and guidance.

Timm started a post-doc position at the CCS just as I was beginning my second year as a PhD student. By this point I, rather arrogantly, felt that I was getting the hang of research and didn't need much help or advice. Timm showed me how wrong I was. His immense depth and breadth of knowledge was a huge source of inspiration. Timm taught me the every day trade of being a scientist: how to analyse and present data, and how to write a scientific paper. I couldn't have hoped for a better mentor.

I thank them both for their guidance and support. It is no exaggeration to say that I simply wouldn't have managed to do the work I have done in this thesis without them. But what touches me more is the fact that despite having no obligation to help me, they both invested an incredible amount of time and effort in me, despite the inherent uncertain outcomes and their own incredibly busy schedules. These acts of kindness are the things that will stay with me the most after my PhD. Today, I feel confident enough to call myself a scientist, a dream of mine since I was a kid, and I can only say that because of you both. I will be forever grateful; thank you.

Another person to whom I owe a great deal is Fernando Bresme. Fernando received an email from me in the weeks before Christmas 2012 asking if he'd like to meet with me to discuss physics, since I noticed we worked on similar problems. Of course, the most likely response from any busy academic in this situation would be no, but Fernando agreed, and two years later we published two papers resulting from that very first meeting. At points, I was meeting with Fernando more frequently than he was with his own PhD students and I was with my own PhD supervisor, and he gave his time gladly. Like Jens and Timm, I will never forget his kindness.

Along similar lines — speculative emails about potential collaborations — I want to thank Lorenzo Botto. In particular, for reading the Chapter on capillary interactions and helping me understand them better throughout my PhD. Thanks for always listening to my stupid ideas, though I think that's finally paid off now that we've managed to complete a successful project together. I look forward to our ongoing collaborations.

Finally on the academic side, I must thank my supervisor Peter Coveney. Peter has given me an incredible amount of freedom during my PhD, which has essentially amounted to a 3.5 year fellowship. I've been allowed to work on whatever problems I wanted to, and this was only possible because of Peter's trust in me, something I have come to realise with time is extremely rare. As I come to the point in my career where I'm applying for fellowships and post-doc positions, I realise what a truly great gift this has been, one that frankly I'm unlikely to receive again in my professional working life, whether in academia or elsewhere. Thank you. I would also like to thank Fujitsu and EPSRC for funding my PhD studentship.

I'd like to thank friends and colleagues of the CCS for their help and companionship over the years. Doing a PhD can be a phenomenally lonely experience, but they've always been there to give advice and make work more enjoyable. The thing I'll remember most about my PhD is the people I've met and worked with; kind, funny, clever, and open-minded. It's rare in life that you get to surround yourself with people like that on a daily basis. Special thanks to Ulf Schiller for reading parts of my thesis and for our many enjoyable chats about physics.

To Mum and Dad, your unconditional love has meant the world to me. As you grow up, you get to see the kind of parenting that other people receive and the effect this has on them as people. The fact that you've never pressured me into following any particular path in life and have let me make my own mind up about everything from a very young age is just an amazing gift that most people never receive, and has made me who I am (for better or worse) today. I would never have followed the path that I eventually did if you hadn't always been there to help and support me when I needed it most, and as sons tend to do, I'm sorry that I haven't been more forthcoming about how much you both mean to me.

Finally, to Anne-Marie, I can't believe you've managed to put up with me for 7 years now. I also don't know any other person whose girlfriend would allow them to move to another country in the pursuit of a crazy dream. Without your support, understanding, patience, and love, I would likely never even have finished my other degrees, never mind this one. I can't wait to start the next chapter of our lives together; thank you.

Contents

List of Figures

Dedicated to Mum, Dad, Steve, and Anne-Marie...

Chapter 1

Particle-Stabilised Emulsions

Oil and water do not mix. If you pour a small amount of olive oil into a glass of water and shake it, spherical oil droplets form and disperse in the water. These droplets then coalesce to form larger droplets, which eventually causes the oil and water to separate completely. The fully separated fluids are thermodynamically stable: having a flat interface separating the two fluids minimises the area of the fluid-fluid interface, which carries an energy cost.

There are, however, many situations in which we want oil and water, or other immiscible fluids, to mix, creating a so-called emulsion. Similarly, there are some situations in which stable emulsions form that we wish to separate again. A non-exhaustive list of materials composed of two immiscible fluids include:

- Foods: mayonnaise, creams, deserts, and beverages.
- Cosmetics: moisturising creams, sun creams, and other lotions.
- Agricultural chemicals: crop-sprays, and pesticides.
- Pharmaceuticals: liquid medicines, medicinal topical gels, lotions, and creams.
- Oil and mining: dispersants for cleaning up oil spills, enhanced oil recovery, mineral separation and flotation.
- Other: paints, cleaning oils/products, and asphalt.

There are two common ways of emulsifying immiscible fluids: by adding soap (surfactants) or solid particles to the mixture.

Surfactants are amphiphilic: they have a hydrophilic and hydrophobic part. In the case of an oil-water emulsion, the surfactant molecules adsorb at the interface of the droplets and arrange themselves such that the hydrophilic head is immersed in water and the hydrophobic tail is immersed in oil. Surfactants are characterised by their hydrophilic-lipophilic balance (HLB) - surfactants with a high HLB are more soluble in water and those with a lower HLB are more soluble in oil.

The contribution from the fluid-fluid interface to the free energy of a two-fluid system is:

$$F = \int_{\partial A} \gamma \, dA \tag{1.1}$$

where ∂A is the surface area and γ is the surface tension (or surface energy) of the fluid-fluid interface. In principle, emulsions are always thermodynamically unstable since the interface area always increases upon emulsification. However, surfactants lower the fluid-fluid interface surface tension i.e. they decrease the energy cost of creating more interface area. High concentrations of certain surfactants reduce the surface tension so much that thermodynamically stable microemulsions form spontaneously.

The microstructure of a microemulsion can take many forms; oil droplets immersed in water (micelles), spherical water droplets immersed in oil (reversed micelles), or water and oil coexisting continuously in a bicontinuous phase [29]. The droplets are usually spherical, but cylindrical, ellipsoidal, and lamellar configurations have also been observed [30]. In all cases, the surfactant molecules adsorb at the fluid-fluid interfaces. If droplets form the size of the micelles range from 5-100nm, depending on the specific properties of the system.

The other common way of emulsifying immiscible fluids is by adding small solid particles – generally micrometre–nanometre size – to the mixture. The small solid particles come into contact with the fluid-fluid interface due to, for example, Brownian motion or mixing and stirring of the emulsion. The particles then adsorb at the fluid-fluid interface,

usually irreversibly because the particles lower the free energy in Equation (1.1) by reducing the fluid-fluid interface area, ∂A. Similarly to surfactant-based microemulsions, particle-stabilised emulsions can form oil-in-water or water-in-oil emulsions (Pickering emulsions), and a bicontinuous phase (known as bijels).

1.1 Pickering Emulsions

Ramsden and Pickering were the first to discover that solid particles could stabilise an oil-water mixture [31, 32]. In a Pickering emulsion, solid particles stabilise distinct droplets of oil or water dispersed in the bulk phase by adsorbing at the fluid-fluid interfaces, as shown in Figure 1.1.

In contrast with microemulsions, macroemulsions such as Pickering emulsions and bijels are kinetically stable but usually thermodynamically unstable [33]. Mechanical work provided by mixing, shaking, or stirring is usually needed to emulsify the mixtures; they do not form spontaneously.

However, Sacanna et al. [34] created thermodynamically stable Pickering emulsions consisting of monodisperse droplets with a size between those of a microemulsion and an unstable macroemulsion. Kraft et al. [35] further investigated these Pickering microemulsions and concluded that amphiphilic ions, a low bare interface tension($\approx$ 10 mN/m) and small colloidal particles (200 nm) that preferentially wet the oil phase are necessary for thermodynamic stability.

In the following we briefly describe the mechanisms behind the formation and stability of emulsions.

1.1.1 Thermodynamics of Pickering Emulsion Formation

Kralchevsky et al. [6] extended the thermodynamic model of Aveyard et al. [36] to develop a theoretical expression for the work required to form an emulsion:

$$W_1 = \frac{3\gamma_{12}V}{r}w_1 \tag{1.2}$$

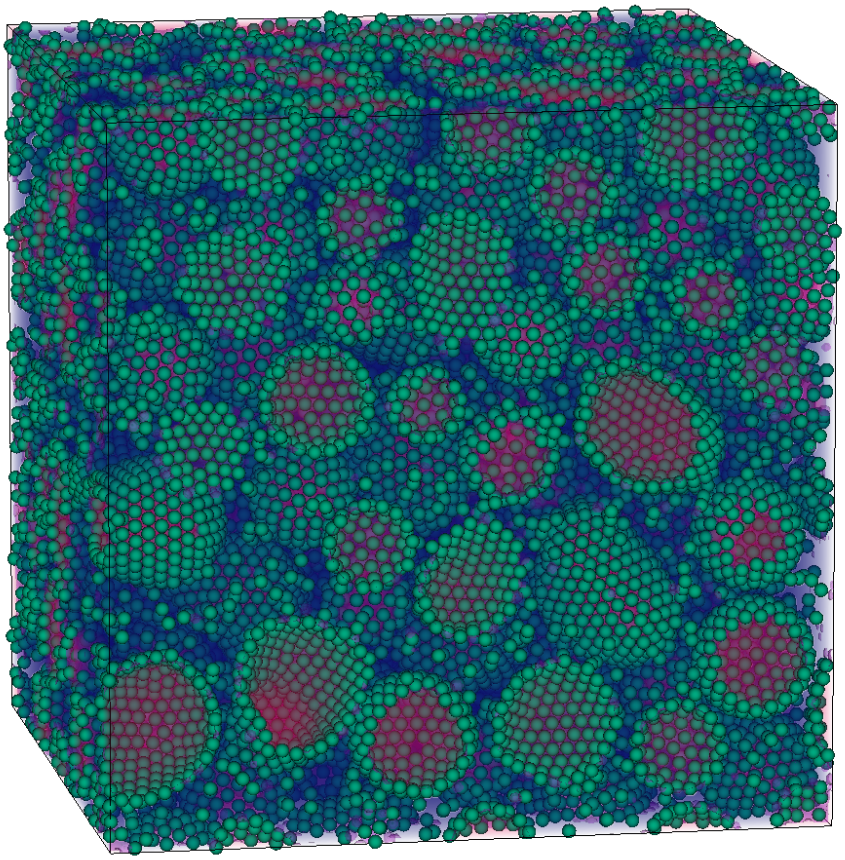

(A)

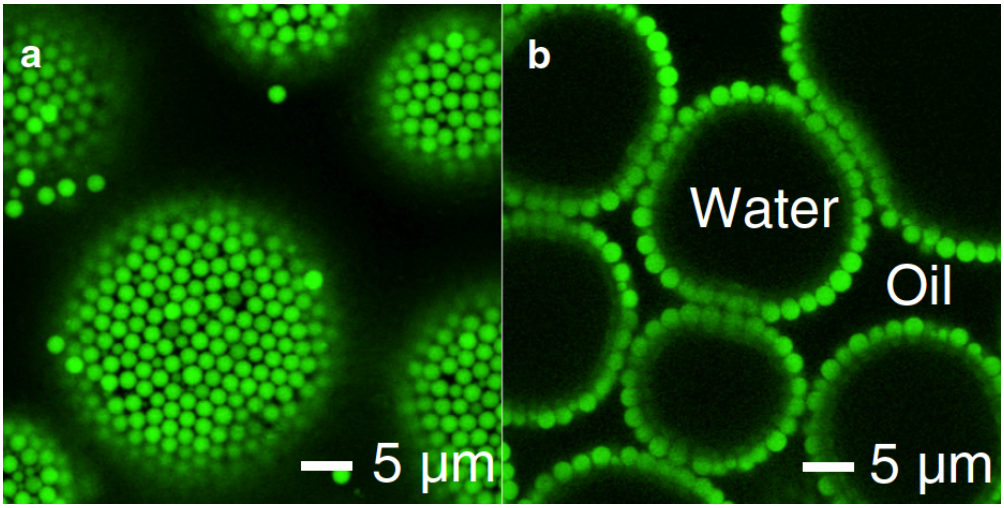

(B)

FIGURE 1.1: (A) A Pickering emulsion simulated with our proprietary lattice Boltzmann code, LB3D. Colloidal particles stabilise distinct droplets of secondary fluid, which are immersed in the primary fluid [4]. Image courtesy of Dr. Stefan Frijters. (B) X-ray microscopy image of a Pickering emulsion. Colloidal particles (green) adsorb at the droplet interfaces. Flocculation can also be seen in (B), a process in which droplets attract each other and aggregate [5]. Reprinted from Ref. [5] with permission from Elsevier.

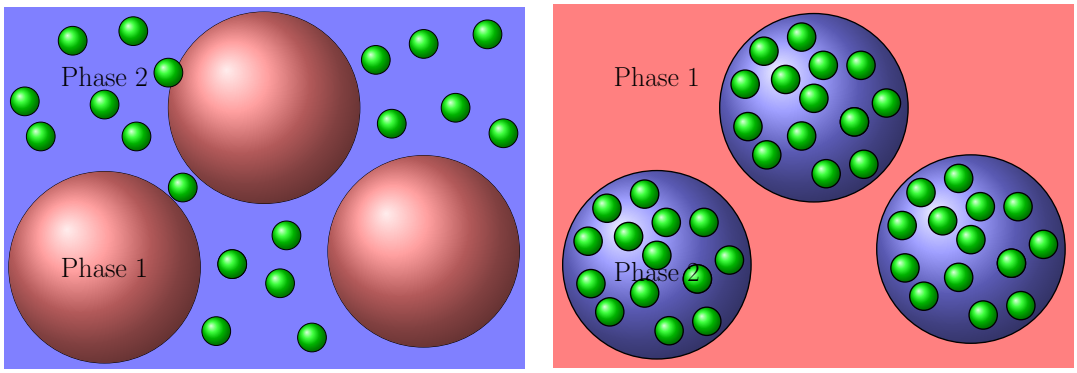

(A) 1-in-2 emulsion. Bancroft emulsion. (B) 2-in-1 emulsion. Anti-Bancroft emulsion.

FIGURE 1.2: Illustration of the two emulsion types considered in the model developed by Kralchevsky et al. [6].

where V is the total volume of fluids 1 and 2, γ_{12} is the fluid 1-fluid 2 surface energy and r is the particle radius. The dimensionless work, w_1, is given by:

$$w_1 = \phi_1 \left[\epsilon(1 - \phi_a b) + \epsilon^2 \phi_a \left(f(\theta)(1 - \phi_a b) - 2b\cos\theta\right)\right] \tag{1.3}$$

where $\phi_1 = \phi_1/(\phi_1 + \phi_2)$ is the volume fraction of fluid 1, ϕ_a is the fraction of interface area removed by the presence of the particles at the interface, ϵ is the ratio of the particle radius to droplet radius, θ is the particle contact angle measured with respect to fluid 2, $b = (1 - \cos\theta)^2$ and $f(\theta) = b(2 + \cos\theta)$. Equation (1.3) assumes that a 1-in-2 emulsion

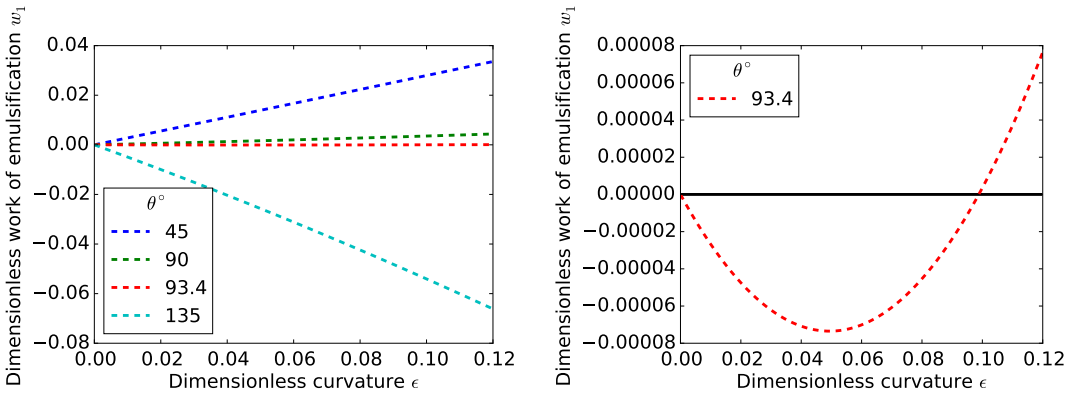

(A) (B)

FIGURE 1.3: (A) Dimensionless work for several different contact angles with fluid 1 volume fraction $\phi_1 = 0.3$ and particle packing fraction $\phi_a = 0.9$, corresponding to close-packing of particles at the interface, for a 1-in-2 emulsion. (B) Zoomed scale for contact angle $\theta = 93.4°$ showing a local minimum i.e. the spontaneous formation of a thermodynamically stable emulsion.

(Figure 1.2a) forms in which the fluid 1 droplets are monodisperse. The model assumes that the particles are initially dispersed in fluid 2, which is an important clarification because Binks and Lumsdon [37] showed that the phase in which the particles are initially dispersed tends to be the continuous phase.

A very similar expression can be developed for the formation of a 2-in-1 emulsion (Figure 1.2b). The Bancroft rule states that the continuous phase is the one in which the emulsifier is more soluble, therefore, if the particles are hydrophilic, an oil-in-water emulsion tends to form (1-in-2 emulsion). A 2-in-1 emulsion is therefore an anti-Bancroft emulsion, in which the preferentially wetted fluid is the discontinuous phase.

In Figure 1.3 we plot some representative curves for different contact angles for an emulsion with $\phi_1 = 0.3$ and $\phi_a = 0.9$, which corresponds to closely packed particles, as a function of dimensionless curvature.

For contact angles $\theta \leq 90°$ the emulsification work w_1 is positive, suggesting that work must be done in order to emulsify the mixture and create droplets of phase 1. The amount of work required to break phase 1 into droplets increases if we desire smaller droplets. For contact angles $\theta \geq 95°$, the emulsification work is negative suggesting that emulsions should form spontaneously provided there are no free energy barriers to overcome, due to the reduction in free energy because of particle adsorption at the interface for these contact angle values.

The zoomed scale for contact angle $\theta = 93.4°$ in Figure 1.3b suggests that a thermodynamically stable emulsion should form spontaneously with dimensionless curvature $\epsilon \approx 0.048$. For this contact angle, the first term in Equation (1.3), $\epsilon(1 - \phi_a b)$, competes with the higher-order curvature term, producing a parabolic rather than linear profile. Since particles have a distribution of contact angles, it is difficult to achieve a thermodynamically stable emulsion given the small range of contact angles that produce these emulsions, which perhaps explains why thermodynamically stable particle-stabilised emulsions are so rarely found.

Using the similar expression for w_2, we can obtain the dimensionless work of formation difference between 1-in-2 emulsification and 2-in-1 emulsification, $\Delta w = w_1 - w_2$, such that for $\Delta w < 0$ a 1-in-2 emulsion is favoured and for $\Delta w > 0$ a 2-in-1 emulsion is favoured.

If phase 1 is the minority phase and the particles are hydrophilic (i.e. prefer phase 2), then 1-in-2 emulsions are thermodynamically favoured. If the particles are hydrophobic, 2-in-1 emulsions are favoured. However, if phase 1 is the majority fluid, then hydrophilic particles produce 2-in-1 emulsions and hydrophobic particles lead to 1-in-2 emulsions. The model therefore predicts that if the contact angle is constant, changing the volume ratio of the two fluids should lead to a change of emulsion type from 1-in-2 to 2-in-1 or vice versa. This so-called catastrophic phase inversion [38–40] should occur for volume ratios of $\phi_1 = 0.5$, which is similar to the value obtained by Binks and Lumsdon [40] experimentally. This model therefore captures many of the important features displayed by emulsions experimentally.

1.2 Pickering Emulsion Instabilities

Because particle-stabilised are usually only kinetically stable, their properties change over time. An emulsion whose properties change more slowly over time is said to be more stable. There are four main causes of emulsion instability: coalescence, flocculation, creaming/sedimentation, and Ostwald ripening, as shown in Figure 1.4.

1.2.1 Coalescence

Droplets coalesce in order to decrease the surface-to-volume ratio of the discontinuous fluid. Particles adsorbed at a fluid-fluid interface provide a physical barrier preventing droplets from coalescing, so-called steric hindrance. If each droplet has a layer of particles adsorbed at the interface, this type of steric hindrance is called "bilayer stabilisation". On the other hand, if particles have a non-90° contact angle, a single layer of particles can bridge two droplets (Figure 1.6). Steric hindrance in particle-stabilised droplets occurs because large detachment energies mean large forces are required to displace the particles vertically at the interface and dense packing on the interface inhibits lateral motion of the particles at the interface.

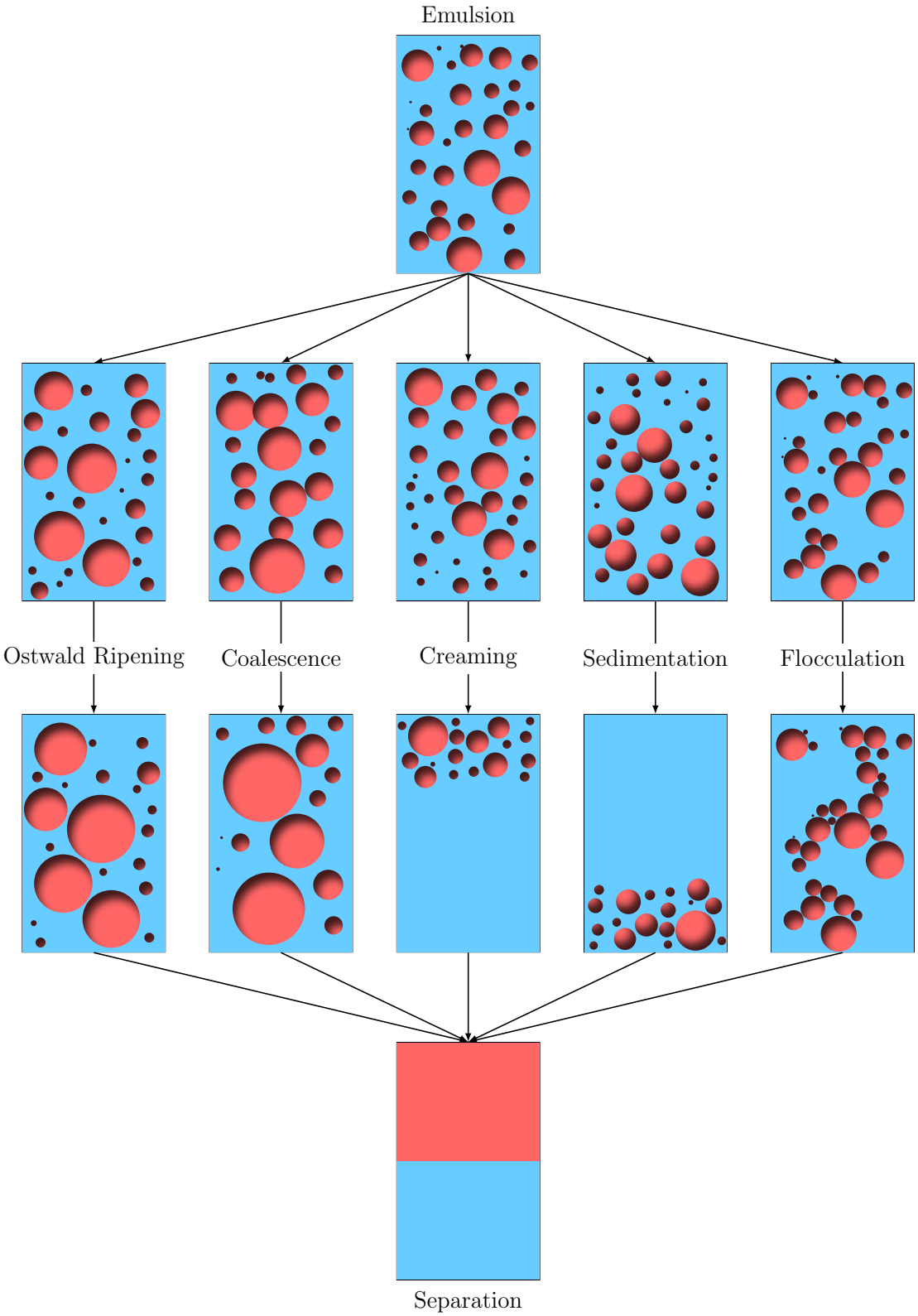

FIGURE 1.4: Illustration of different emulsion instabilities that can cause emulsion phase separation.

1.2.1.1 The Thermodynamics of Coalescence

Lopetinsky et al. [41] developed a simple thermodynamic argument that compares the free energy of two equal sized particle-laden water droplets immersed in oil before and after coalescence. They assumed that the droplet radius is much larger than the particle radius so that they can neglect curvature effects and that the particles completely cover the droplet interface. If the decrease in fluid-fluid interface area, ΔA, reduces the free energy more than the energy required to detach n particles from the interface, E_{d}, then thermodynamics favours coalescence:

$$\Delta F_{\mathrm{co}} = \gamma_{12}\Delta A + nE_{\mathrm{d}}. \tag{1.4}$$

Volume conservation dictates that $2V_1 = V_2$, where V_1 and V_2 are the initial and final droplet volumes, leading to the relation $R_2 = 2^{\frac{1}{3}}R_1$, where R_1 and R_2 are the initial and final droplet radii. Therefore, coalescence changes the droplet area by an amount $\Delta A = 4\pi R_1^2(2^{\frac{2}{3}} - 2)$. When two droplets coalesce, the total droplet surface area decreases. Since the particles are assumed to closely pack on the surface, n particles must detach from the fluid-fluid interface. The removal of n particles increases the fluid-fluid interface area by $n \approx -\Delta A/\pi r^2$ and so the free energy of coalescence becomes:

$$\Delta F_{\mathrm{co}} = \Delta A\left(\gamma_{12} - \frac{E_{\mathrm{d}}}{\pi r^2}\right) \tag{1.5}$$

Using the expressions for the change in interface area ΔA defined above and the detachment energy of a particle from a planar fluid-fluid interface into oil, $E_{\mathrm{do}} = \pi r^2\gamma_{12}(1 + \cos\theta)^2$, yields:

$$\Delta F_{\mathrm{co}} = 4\pi R_1^2\gamma_{12}(2 - 2^{\frac{2}{3}})\left(\cos\theta(\cos\theta + 2)\right) \tag{1.6}$$

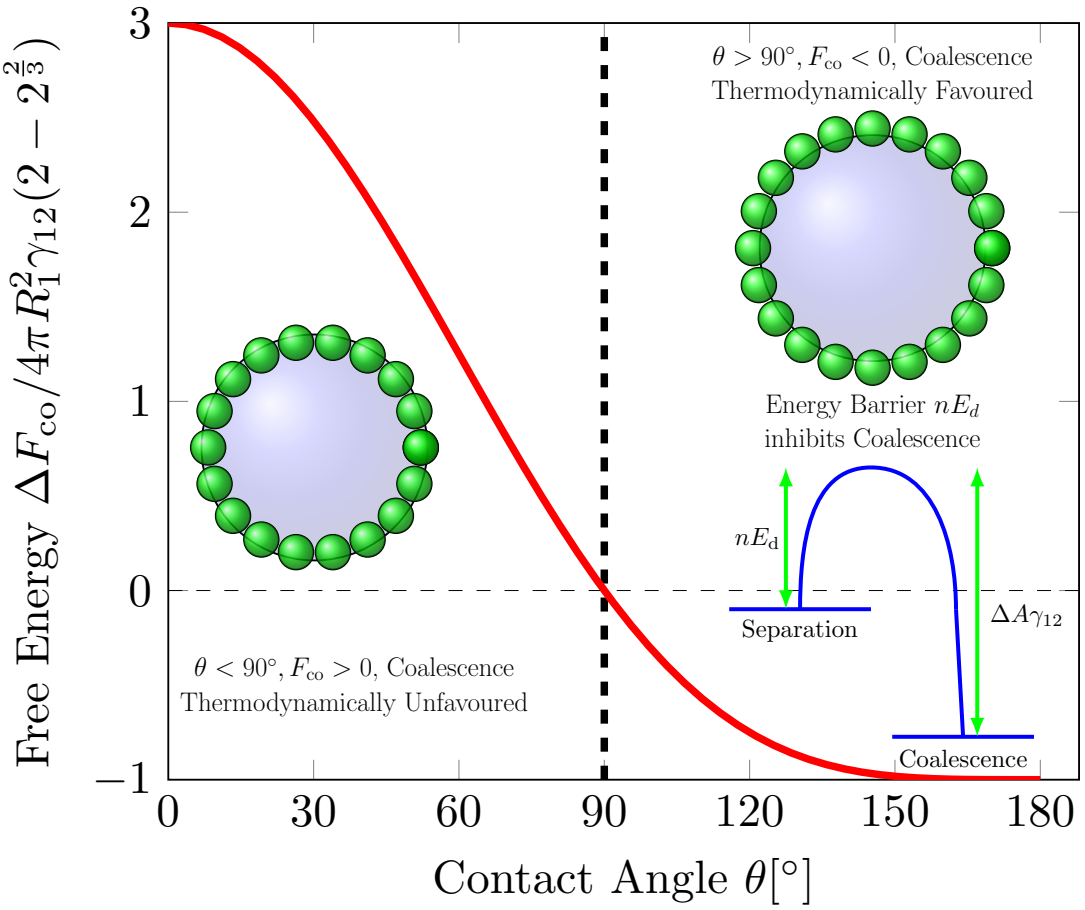

FIGURE 1.5: Schematic illustrating the conditions under which two water droplets coalesce based on the thermodynamic model in Equation (1.6). Even if thermodynamics favours coalescence for contact angles $\theta > 90$, n particles must be detached from the fluid-fluid interface at an energy cost of E_d each. Therefore, the free energy barrier is $\approx nE_d$ particles.

Equation (1.6) shows that thermodynamics favours coalescence for particles with contact angles $\theta > 90^\circ$ (hydrophobic particles) and that for particles with contact angles $\theta < 90^\circ$ (hydrophilic particles) coalescence is thermodynamically unfavoured and the emulsion droplets are thermodynamically stable (Figure 1.5). However, even when thermodynamics favours droplet coalescence in the case of hydrophobic particles, an energy barrier $E_B \approx nE_d$ must be overcome. It is this energy barrier that sterically hinders droplet coalescence and stabilises Pickering emulsions from droplet coalescence [36, 42].

In order to provide a layer of particles that stabilise droplet coalescence by steric hindrance, the particles should not easily move laterally on the interface. Otherwise, lateral particle movement may expose interface areas that are then able to come into contact. Tambe and Sharma [43] suggested that if the detachment energy of particles were

the limiting factor in droplet coalescence, droplet stability would increase linearly with the particle concentration, which they did not observe experimentally. Instead, they showed that moving the particle laterally on the interface requires an order of magnitude less energy than detaching a particle from an interface. Therefore, preventing particles moving laterally on the interface increases emulsion stability, and only large particle concentrations and strong inter-particle attraction provide a large resistance to lateral displacement.

1.2.1.2 Capillary Pressure Between Particle Laden Droplets

An alternative approach to understanding Pickering emulsion droplet stability considers the pressure between two colliding droplets. When two droplets approach each other during coalescence, they trap a thin film of continuous fluid in the space between the droplets. The capillary pressure is the pressure difference between this trapped thin film and the fluid inside the droplets. As the film thins, the film pressure increases. The film ruptures at a critical height, h_c, where van der Waals attraction causes the two films to come into contact and the film spontaneously thins. The critical height h_c is typically $1 - 30$nm [44]. Kaptay [45] combined and analysed many previous results [46–48] and developed a general expression for the maximum capillary pressure at which the thin film ruptures:

$$P_{\mathrm{c,max}} = \pm \frac{2\gamma_{12} p \cos(\theta \pm z)}{r} \tag{1.7}$$

where r is the particle radius and p and z are parameters that depend on the packing and arrangement of the particles. $z = 0$ corresponds to a monolayer of particles stabilising the film (Figure 1.6a) and $z = 0.633$ corresponds to a closely packed double layer (Figure 1.6b). The negative solution corresponds to water-in-oil emulsions and the positive solution to oil-in-water emulsions.

Equation (1.7) suggests that emulsion stability increases with increasing maximum capillary pressure. Denkov et al. [48] used a similar model to Equation (1.7) to show that smaller particles increase the critical pressure and therefore stabilise emulsions better. Their model also suggests that intermediate contact angles that are not too close to

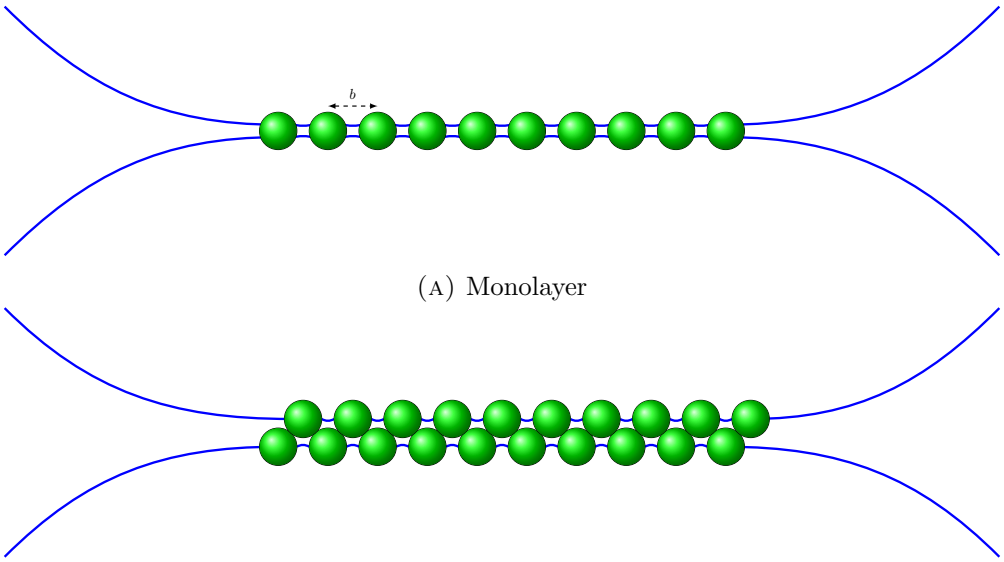

(A) Monolayer

(B) Bilayer

FIGURE 1.6: Two arrangements of particles adsorbed at a fluid-fluid interface corresponding to (A) single-layer $z = 0$ and (B) a double-layer $z = 0.633$ in Equation (1.7).

0° or 90° allow the greatest compromise between the detachment energy of the particles and the distance between the films in the case of monolayers. The particles must preferentially wet the continuous phase in order to stabilise the droplets.

The theoretical models based on Equation (1.7) predict a higher film stability than experiments observe. The theoretical models assume regularly spaced and homogeneous particle arrays. In reality, there are defects and the particles experience lateral forces that introduce inhomogeneity to the particle arrangements at the interface: for example, particles attract each other via capillary interactions that arise due to the interface curvature and repel each other due to electrostatic interactions [49]. Areas at the droplet interface deprived of particles represent "weak spots" that rupture at lower capillary pressures than predicted by theoretical models such as those in Equation (1.7).

Recent computer simulations by Fan and Striolo [50] confirmed that the particle density at the interface is extremely important in determining whether two droplets coalesce. If the area of droplet interface per particle is less than a critical value, droplets coalesce easily and particle properties play little role. If the area per particle is greater than a critical value, particle properties are very important in determining the droplet stability. Droplets are most stable when the particles have a contact angle that causes them to protrude into the continuous phase, which makes droplet coalescence less likely.

1.2.1.3 Thin Film Drainage

As the film between two emulsion droplets thins, continuous fluid flows away from the region where the droplets coalesce into the bulk continuous phase. Therefore, the particle-laden droplet interfaces experience a shear flow. Tambe and Sharma investigated the rheology of particle-laden droplet interfaces theoretically for cubic [51] and hexagonal packing [43, 52]. Their models suggest that particle-laden interfaces behave visco-elastically and that the elasticity depends strongly on the particle concentration. They showed that the film thickness decreases much more slowly as the surface coverage of particles increases. Therefore, droplets with high particle packing fractions coalesce more slowly and this leads to more stable emulsions.

1.2.2 Ostwald Ripening

Ostwald ripening [53] occurs when fluid in the discontinuous phase (distinct droplets) leaves small droplets, diffuses through the continuous phase, and joins larger droplets: small droplets get smaller; large droplets get larger; and the mean droplet radius increases with time. The fluid in the discontinuous phase does this because larger droplets have a smaller pressure difference compared with the continuous phase and are therefore more stable. For the dispersed phase to diffuse through the continuous phase, the dispersed phase must be soluble with the continuous phase. As the dispersed phase droplets get smaller, its solubility with the continuous phase increases. The average droplet radius, R_N, changes with time as

$$\frac{dR_N^3}{dt} = \frac{8}{9}\frac{\gamma_{12} V_M D S_\infty}{k_B T} \tag{1.8}$$

where D is the diffusion coefficient of the dispersed fluid, S_∞ is the bulk solubility of the dispersed phase in the continuous phase, V_M is the molecular volume of the dispersed phase, and γ_{12} is the fluid-fluid surface energy [49, 53–55].

Creating droplets with a narrower size distribution inhibits Ostwald ripening, as does decreasing the surface tension or the bulk solubility of the dispersed phase. However, Ostwald ripening does not usually affect Pickering emulsions because as the droplets

shrink, the particles compress until the particle monolayer at the interface jams completely. If the droplets shrink further, the fluid between the particles (the menisci) bends inwards and opposes the Laplace pressure that drives Ostwald ripening [49, 53–55] (as shown by the fluid between the particles in Figure 1.6b).

1.2.3 Sedimentation and Creaming

Sedimentation and creaming are two sides of the same coin: if the particle-stabilised droplets are more dense than the fluid they are dispersed in, they sink due to gravity (sediment), if they are less dense, they rise due to buoyancy (cream). The creaming or sedimentation velocity of a single droplet assuming Stokes' flow and a dilute emulsion is given by:

$$v = \frac{2R^2 \Delta\rho g}{9\mu_c} \tag{1.9}$$

where g is gravitational acceleration, R is the droplet radius, $\Delta\rho$ is the density difference between the fluids, and μ_c is the viscosity of the continuous phase. Reducing the droplet size or density difference between the fluids can slow the sedimentation/creaming velocity of a droplet.

1.2.4 Flocculation

Flocculation occurs due to attractive forces, usually van der Waals forces, between emulsion droplets. Flocculation leads to Pickering emulsion instability because it increases creaming or sedimentation rates due to an increase in the effective droplet sizes, and also because it increases the probability of droplet coalescence due to the droplets being in contact [56, 57]. Depending on the required emulsion properties, flocculation can either be desirable or undesirable.

It is possible to stabilise Pickering emulsion droplets from coalescence by adding repulsive interactions between the particles. This can be achieved by, for example, using charged particles that repel each other due to Coulomb repulsion, or by adding flexible

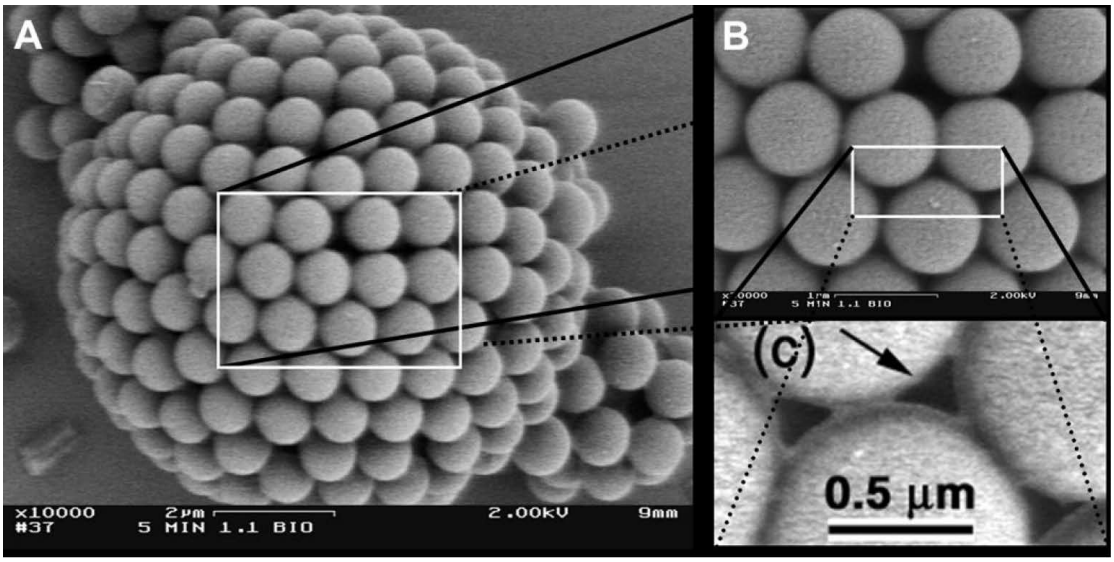

FIGURE 1.7: (A) Selectively permeable capsules composed of colloidal particles [7]. The pore size, and therefore permeability, can be controlled by changing the particle size and by lengthening the sintering process. The sintering fuses the particles together, as seen in (C). One of the unresolved issues with bulk colloidosome production is droplet flocculation, which can clearly be seen in (A). From Ref. [7]. Reprinted with permission from AAAS.

polymers that increase the steric hindrance or introduce an elastic energy that must be overcome [58].

1.3 Applications of Particle-Stabilised Emulsions

1.3.1 Colloidosomes: Microcapsules with Selective Permeability

Dinsmore et al. [7] were one of the first to extend the applications of particle-fluid-fluid interactions beyond simply stabilising emulsions. They created colloidosomes, which are microcapsules made of solid particles whose permeability, size, and strength can be tailored.

To make a colloidosome, they first created a Pickering emulsion and then locked the particles in place, which can be achieved in several ways. One way is to gently sinter the particles by heating them slightly above their glass transition temperature, T_g. The particles then fuse together, as shown in Figure 1.7C. The sintering time controls the size of the bridges between the particles, which enables the precise control of the pore size. Increasing the sintering time also increases the mechanical strength of the colloidosomes.

Choosing particles with different glass transition temperatures allows a broad range of sintering temperatures to improve compatibility with the two immiscible fluids. Other locking methods include adding polyelectrolyes, which bind to particles with opposite charge producing flexible, deformable but tough capsules, and van der Waals attraction, which holds particles together. Tuning the mechanical strength allows the yield stress to be adjusted and enables the colloidosome to rupture at defined shear stresses.

The colloidosome permeability depends directly on the size of the pores between the particles. Large particles pack densely on the droplet surfaces and show a nearly crystalline configuration, but perfect hexagonal symmetry is elusive due to topological constraints: a curved surface requires a minimum of 12 five-fold defects, similar to the pentagons on a football [59]. As the particle size decreases, the surface coverage decreases. Nevertheless, if we assume perfect hexagonal symmetry, the size of the holes is $0.3R$ where R is the particle radius, and so the pore size can be directly controlled by the particle size, allowing Dinsmore et al. [7] to easily achieve pore sizes ranging from micrometres to nanometres.

The capsule size can be controlled by regular emulsification techniques [60], and allows flexibility in the choice of encapsulated materials. Dinsmore et al. [7] prepared capsules with sizes ranging from millimetre to sub-micrometre.

One potential application of colloidosomes is drug delivery; blood drug concentration peaks shortly after ingesting a drug orally and then decreases quickly. Therefore, relatively large doses of the drug need to be taken at regular intervals in order to maintain a consistent amount of the drug in the blood stream. With colloidosomes, the permeability controls the diffusion of the encapsulated drug into the blood, which therefore requires less drug to maintain a consistent blood concentration, causing fewer side effects. However, problems related to emulsion instability must be solved in order to facilitate bulk production of colloidosomes. For instance, microcapsules tend to flocculate, as shown in Figure 1.7A, and sintering therefore fuses the floccs together.

1.3.2 Colloidal Molecules

Manoharan et al. [8] created colloidal molecules from Pickering emulsions by slowly evaporating the oil phase. During the evaporation, capillary forces lead to a spherically

symmetric compressive force until the particles come into contact. At this point, steric interactions break this symmetry and the particles rearrange according to the balance of capillary forces and packing constraints. During this stage, the colloidal particles act as hard spheres. Once the dispersed phase evaporates completely, van der Waals forces keep the particles in contact. Remarkably, for a given number of colloidal particles adsorbed at a droplet interface, the evaporation always leads to the same final cluster structure. Surface charges on the particles on the outside of the cluster stop the individual clusters from aggregating with other clusters.

The symmetry of the clusters (Figure 1.8) is very different from symmetries seen in other materials and did not minimize the cluster volume. In fact, Manoharan et al. [8] found that the particle arrangements corresponded to the minima of the second moment of the mass distribution, $M_2 = \sum_{i=1}^{n} |\mathbf{r}_i - \mathbf{r}_0|^2$, where $\mathbf{r}_i$ is the position of the i^{th} particle and $\mathbf{r}_0$ the position of the cluster centre-of-mass, calculated by Sloane et al. [61]. Lauga and Brenner [62] later showed that the particle arrangements arise purely due to geometrical constraints during the evaporation phase.

Wang et al. [9] recently extended this technique to create colloidal molecules with valence. They first created a colloidal molecule by evaporating the oil phase from a droplet of n amidinated polystyrene particles using the same process as [8]. They then swelled the clusters with styrene and polymerised the styrene to expose the patches of the amidinated particles. They functionalised biotin on the amidinated patches, and then biotinated DNA oligomers bind to the functionalised patches, as shown in Figure 1.9.

These patchy particles therefore have directional interactions based on where the patches are located mimicking the valency of regular atoms. Indeed, valencies analogous to the s, p, sp, sp^2, sp^3, sp^3d, sp^3d^2, and sp^3d^3 hybridised orbitals are possible depending on the number of particles in the cluster.

The aim of producing such colloidal molecules with valence is to create 3D structures and materials of practical interest. The diamond lattice possesses a 3D photonic bandgap [63], but current "top-down" fabrication methods are expensive and inefficient. Bottom up assembly of 3D crystals using colloidal particles is highly desirable due to its scalability and cost-effectiveness. However, a diamond lattice of colloidal molecules remains elusive because the colloids require 4-fold bond coordination. Zhang et al. [64] showed that the patchy particles developed by Wang et al. [9] can self-assemble into

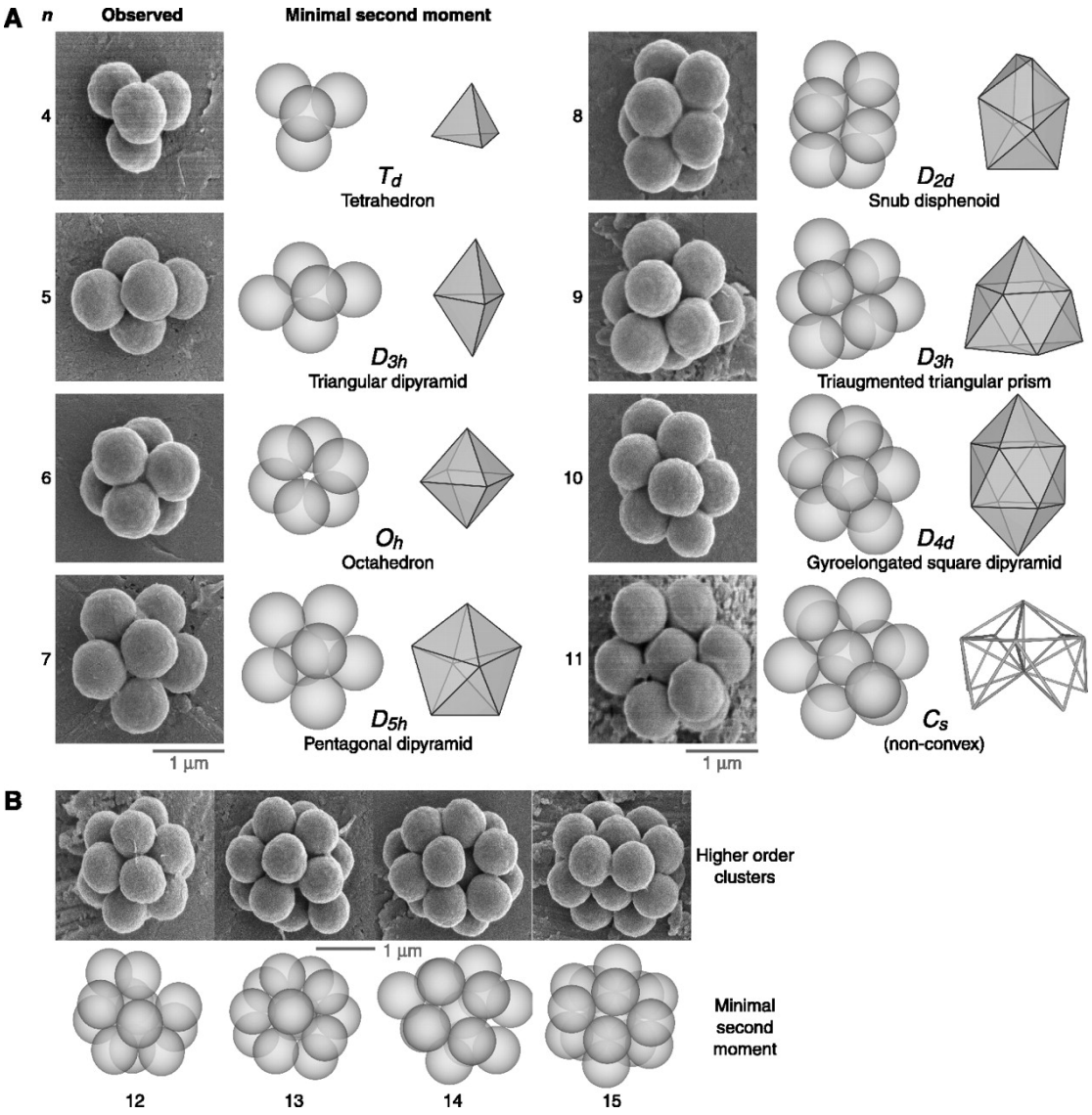

FIGURE 1.8: Clusters with $n = 4 - 11$ particles in each cluster. The symmetry of the clusters corresponds to those expected from minimising the second moment of the mass distribution. From Ref. [8]. Reprinted with permission from AAAS.

a diamond lattice. Hence, the design and manufacture of colloidal molecules with valence using emulsions is potentially a huge technological advance in creating low-cost 3D materials.

1.4 Other Particle-Stabilised Emulsions

1.4.1 Bijels

Stratford et al. [65] predicted a new type of particle-stabilised emulsion, the bicontinuious

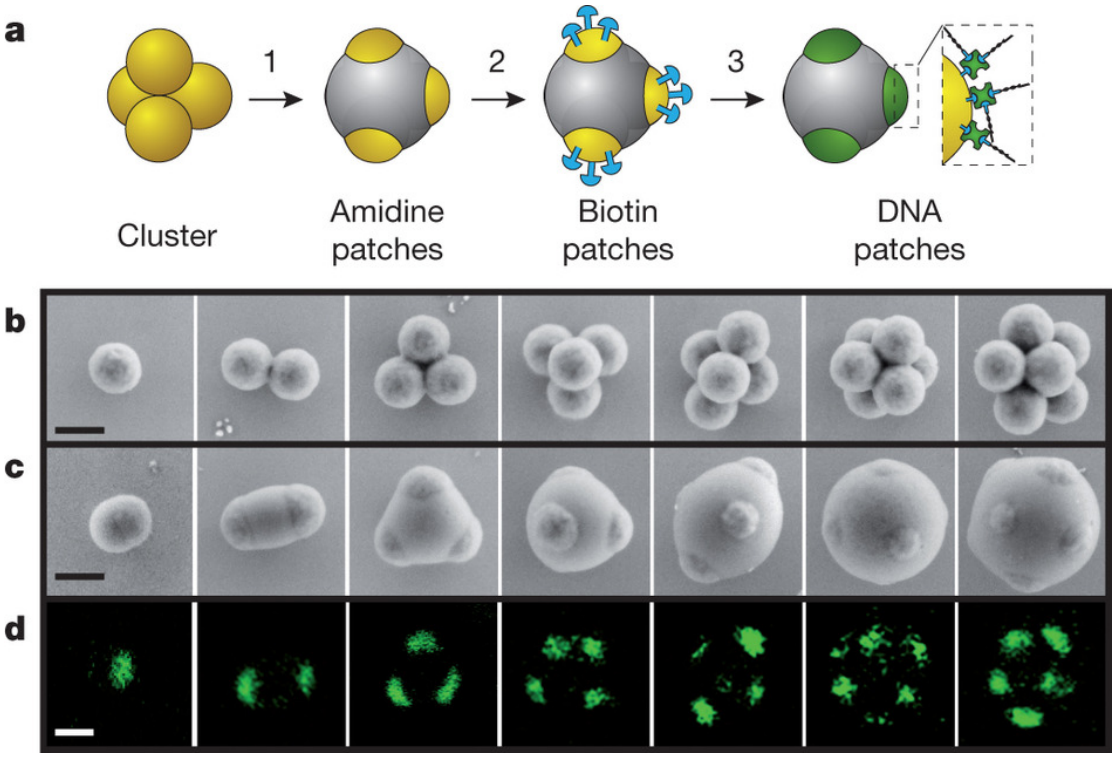

FIGURE 1.9: Clusters with $n = 4 - 11$ particles in each cluster. The symmetry of the clusters corresponds to those expected from minimising the second moment of the mass distribution. Reprinted by permission from Macmillan Publishers Ltd: Nature [9], copyright (2012).

jammed emulsion gel (bijel), using lattice Boltzmann simulations. Herzig et al. [10] and Clegg et al. [66] later confirmed this prediction experimentally. To create a bijel experimentally, a miscible mixture is quickly quenched by rapidly cooling the mixture, creating two continuous fluid phases. However, without colloidal particles, the phases would eventually separate due to their lack of thermodynamic stability. With added particles, the particles adsorb at the fluid-fluid interface and arrest the phase separation so that both the fluid phases are continuous and there are no distinct droplets such as in Pickering emulsions. Remarkably, Sanz et al. [67] showed that the bijel structure prevails even when the fluids are remixed, creating a so-called "Monogel".

A significant technological advantage of bijels is that their shear modulus can be tuned over a wide range by changing the particle size and concentration [68]. Additionally, since the individual fluids flow separately from one another with the jammed interface acting as a porous boundary, bijels might be used as a "reactor" with applications in, for example, catalysis.

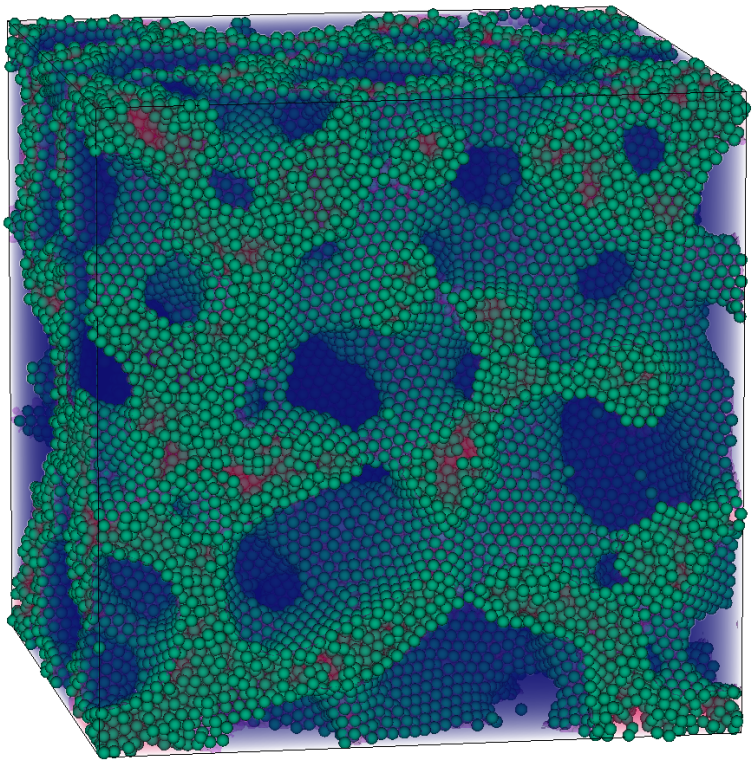

(A)

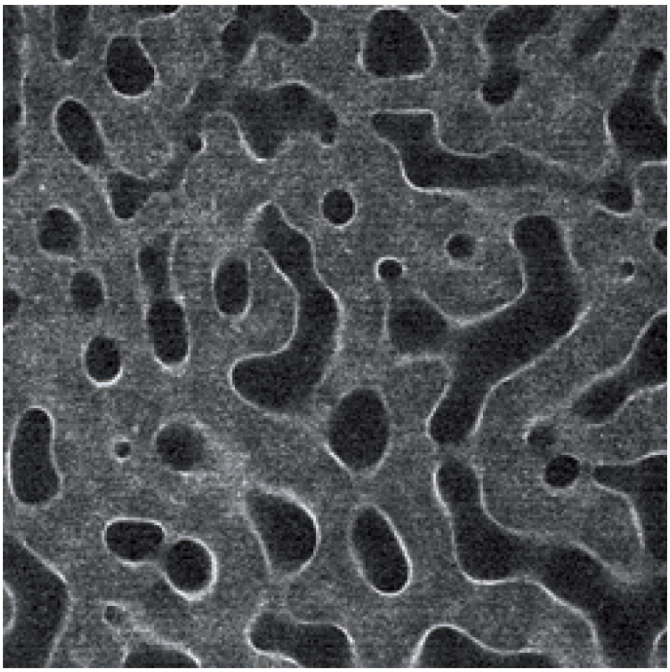

(B)

FIGURE 1.10: (A) A Bijel simulated with LB3D. Particles adsorb and jam at the interface, but the fluid phases are continuous. (B) Experimental image of a bijel [10]. White regions represent particles, which can clearly be seen at the interface between the two fluids. Reprinted by permission from Macmillan Publishers Ltd: Nature Materials [10], copyright (2007).

Jansen and Harting [4] investigated the conditions under which bijels or Pickering emulsions form. They found that the key parameters are the particle contact angle and the volume ratio of the two fluids. When the volume ratio of the two fluids is roughly equal, bijels tend to form. Particle volume fraction has little effect on whether a bijel or Pickering emulsion forms.

1.4.2 Capillary Suspensions

Koos and Willenbacher [69] found that adding $< 1\%$ volume fraction of immiscible secondary fluid to a primary fluid with colloidal particles dispersed in it could change the viscosity of the mixture by more than an order of magnitude and the yield stress of the mixture by two orders of magnitude. Surprisingly, whether the secondary fluid preferentially wetted the particles or not, they saw approximately the same changes to the suspension rheology. However, different mesoscopic structures form depending on the wettability of the particles when the secondary fluid is added.

It was already known that adding preferentially wetting secondary fluid causes a transition from a fluid-like to a gel-like state [70, 71]: small fluid bridges of secondary fluid form between the particles called pendular bridges (Figure 1.11A). This leads to an attractive capillary force between the particles, given by:

$$F_c = 2\pi r \gamma_{12} \cos\theta \tag{1.10}$$

where γ_{12} is the fluid-fluid surface tension, θ is the particle contact-angle, and r is the radius of the particles. This attractive force causes particles to aggregate and form network like structures. Equation (1.10) assumes the particles are touching and that the particles are much larger than the pendular bridge between the particles.

If the secondary fluid does not preferentially wet the particles, particles encapsulate small droplets of the secondary fluid in order to stop it from forming a large fluid-fluid surface area with the immiscible primary fluid. Koos and Willenbacher [69] called this the capillary state (Figure 1.11B). In the capillary state, small droplets of secondary fluid are evenly dispersed in the primary fluid. The particles aggregate around these

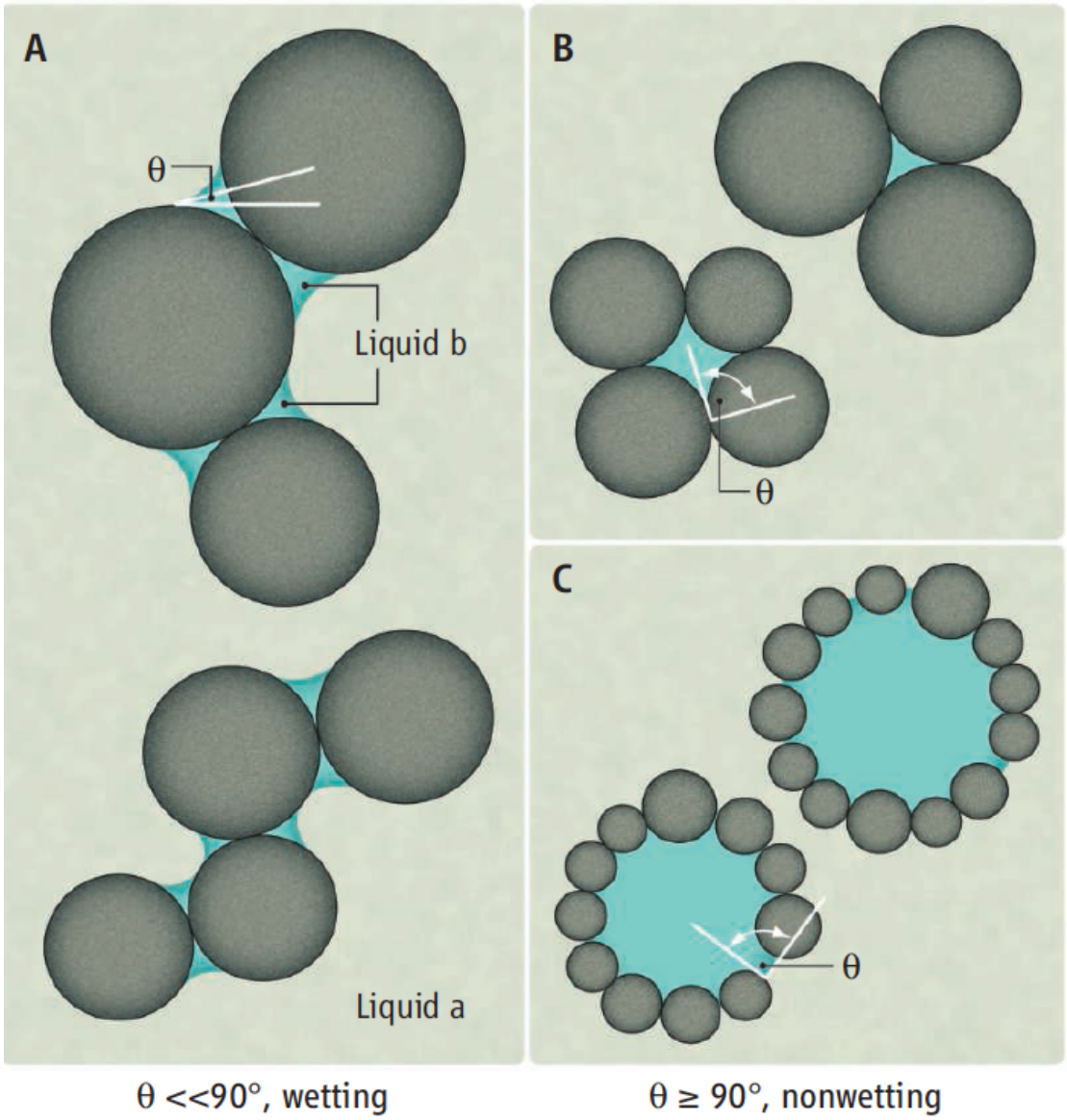

FIGURE 1.11: (A) Pendular bridges form between the particles if the secondary fluid preferentially wets the particles. (B) The capillary state forms when the secondary fluid does not preferentially wet the particles. (C) In Pickering emulsions, the droplet radius R_d is much greater than the particle radius, R, in contrast with the capillary droplets, where $R \approx R_d$. From [11]. Reprinted with permission from AAAS.

small droplets, and these individual clusters then combine with other clusters to form a network-like structure.

The capillary state shares similarities with Pickering emulsions (Figure 1.11C). However, in the capillary state the droplet radius, R_d, is of the order of the particle radius, $R \approx R_d$, where as in Pickering emulsions the droplet radius is many times larger than the particle radius, $R/R_d \ll 1$.

Koos et al. [72] also found that by decreasing the particle size, network formation between particles in the pendular state was stronger, resulting in an increased yield stress. This is consistent with a mathematical formulation of the yield-stress of a macroscopic suspension where the particles are interacting via pendular bridges:

$$\sigma = \frac{f(\phi)}{r^2} F_c = f(\phi) \frac{2\pi\gamma_{12}\cos\theta}{r} \tag{1.11}$$

where $f(\phi)$ is a generic function of the volume fraction of particles, ϕ. For capillary suspensions, where $\phi \ll 1$, a reasonable approximation is $f(\phi) = \phi^2$. Adding surfactant or increasing the sample temperature, both of which act to decrease the surface-tension, resulted in weaker pendular bridges and order of magnitude drops in the viscosity and yield stress of the suspensions.

Finally, Koos and Willenbacher [73] investigated the cluster arrangements of particles aggregating around small droplets in the capillary state. They hypothesised that the clusters aggregate forming a spanning network, causing the gel-like behaviour. Their Surface Evolver [74] computational model found that tetrahedral clusters tend to be the most stable for contact angles $\theta < 151.2°$ and smaller droplet volumes, but that higher droplet volumes favoured an octahedral or mixed-octahedral cluster network. This model successfully predicted the rheology of some of their capillary suspensions. They found that particles aggregate around small droplets because the energy in this configuration is lower than if the small secondary fluid droplets are dispersed in the primary fluid with free particles. However, the global energy minimum occurs for complete phase separation, and the droplet clusters formed in the capillary state are therefore kinetically but not thermodynamically stable.

The discovery of the capillary state will allow the control of suspension flow properties simply by tuning the amount of secondary fluid added. Currently, added surfactants or polymers control suspension rheology, which can often be expensive and environmentally unfriendly.

1.5 Thesis Layout

In this Chapter, I briefly introduced the physics of emulsions and summarised some of the experimental and theoretical work that has been done in order to understand emulsions. I aimed to demonstrate why particle-stabilised emulsions are interesting and worth studying in order to provide motivation for the work I have undertaken in this thesis. In particular, the latter sections of this introduction highlight some of the novel uses and properties of particle-stabilised emulsions that have been discovered only in the last few decades and that still require further understanding. Additionally, I described some novel particle-stabilised emulsions — bijels and capillary suspension — for which very little theoretical work has been undertaken in order to understand their formation and properties, in contrast with the vast body of literature on Pickering emulsion stability.

In order to understand the properties of emulsions better so that we can create new soft materials, we need a better understanding of the basic physical principles underlying particle-fluid-fluid interactions. This thesis centres around modelling the interaction of particles with fluid-fluid interfaces in the hope of understanding these fundamental interactions better so that they may be exploited for scientific or technological purposes in future.

In Chapter 2, I introduce the background theory and previous research on capillary interactions in detail, since most of the results in this thesis are related to this area. Chapter 3 introduces the simulation model used in this thesis to simulate particle-fluid-fluid interactions. In Chapter 4 I discuss new results based on the detachment energy of particles from fluid-fluid interfaces, which has important consequences for the stabilisation of emulsions using anisotropic particles. In Chapter 5 and 6 I present new results regarding the behaviour of magnetic ellipsoidal particles at fluid-fluid interfaces as they tilt in response to an external magnetic field. Chapters 4, 5, and 6 are based on

three peer-reviewed journal articles that I published during my PhD. Finally, Chapter 7 concludes this thesis.

Chapter 2

Capillary Interactions

2.1 Introduction

Colloidal particles adsorb strongly at fluid-fluid interfaces because they replace fluid-fluid interface area with fluid-particle interface area that has a lower surface energy. Once adsorbed at an interface, particles can interact with each other via different interactions, such as capillary interactions.

Capillary interactions arise when particles deform a fluid-fluid interface. The deformations create excess interface area compared with a minimum-area flat interface. Particles can minimise this excess interface area by overlapping their interface deformations with deformations induced by other particles. Capillary interactions may be combined with other interactions, for example electromagnetic interactions, in order to control the assembly of particles at fluid-fluid interfaces. If the assembly of particles can be controlled, it may be possible to create materials with specific and desirable properties.

Much recent research has focussed on the possibility of using capillary interactions for *directed* assembly of particles at interfaces. By choosing specific particle properties, the interface deforms in a predictable way, and certain types of deformations are anisotropic, causing particles to assemble in particular orientations.

In order to understand how the interface deforms around a particle, we consider the shape of the interface at a particular position according to the Young-Laplace equation:

$$P_1 - P_2 = \gamma_{12}\left(\frac{1}{R_{min}} + \frac{1}{R_{max}}\right) \tag{2.1}$$

where R_{min} and R_{max} are the principal radii of curvature of the interface, P_1 and P_2 are the pressure of fluid 1 and fluid 2, respectively, and γ_{12} is the fluid-fluid interface surface tension.

In the flat interface limit, the principal radii of curvature tend to infinity and the pressure difference across the surface at that point vanishes $P_1 - P_2 = 0$. In the far field, we assume that the particle-induced interface deformations disappear (zero mean curvature) and the pressure difference vanishes.

We define an interface height at the contact line $h_c(r_c, \theta_c)$ where r_c is the radial distance from the particle centre and θ_c is the polar angle. The interface height elsewhere on the interface is $h(r, \theta)$. In the case where the height of the surface is defined in terms of two coordinates $h(r, \theta)$, we can use differential geometry to express the mean curvature of the interface:

$$\left(\frac{1}{R_{min}} + \frac{1}{R_{max}}\right) = \nabla \cdot \left(\frac{\nabla h}{\sqrt{1 + (\nabla h)^2}}\right) \tag{2.2}$$

so that Young-Laplace equation (Equation 2.1) can be written as:

$$P_1 - P_2 = \gamma_{12} \nabla \cdot \left(\frac{\nabla h}{\sqrt{1 + (\nabla h)^2}}\right) \tag{2.3}$$

If we take gravity into account using $P = \rho g h$, where ρ is the fluid density and g the acceleration due to gravity, we obtain:

$$(\rho_1 - \rho_2) g h = \gamma_{12} \nabla \cdot \left(\frac{\nabla h}{\sqrt{1 + (\nabla h)^2}}\right) \tag{2.4}$$

We can rescale this equation according to a characteristic particle size, R_p, by normalising the interface height $\tilde{h} \mapsto h/R_p$ and the gradient $\tilde{\nabla} \mapsto \nabla/R_p$ giving:

$$\tilde{\nabla} \cdot \left(\frac{\tilde{\nabla}\tilde{h}}{\sqrt{1 + (\tilde{\nabla}\tilde{h})^2}} \right) = \text{Bo } \tilde{h} \tag{2.5}$$

where

$$\text{Bo} = \frac{(\rho_1 - \rho_2) g R_p^2}{\gamma_{12}} \tag{2.6}$$

is the Bond number, which quantifies the balance between gravitational forces and surface tension forces. We can define a capillary length $L_c = \sqrt{\frac{\gamma_{12}}{(\rho_1 - \rho_2)g}}$, which determines the length scale over which interface deformations due to gravity propagate, so that the Bond number can be rewritten as $\text{Bo} = \frac{R_p^2}{L_c^2}$.

The capillary length tells us two important things: Firstly, if a particle is significantly smaller than the capillary length $R_p \ll L_c$, the Bond number is negligible $\text{Bo} \approx 0$ meaning that surface tension forces are much larger than gravitational forces and therefore we can neglect the effect of gravity on the particle. Secondly, the capillary length essentially specifies an interaction cut-off: if two particles are adsorbed at an interface and the particle-particle separation, r_{AB}, is greater than the capillary length, $r_{AB} > L_c$, the particles will not interact via capillary interactions. An air-water interface has a capillary length $L_c = 2.3\text{mm}$.

In the analysis of capillary interactions, we frequently consider the "small interface slope" limit, $\tilde{h} \ll 45°$. In this case, $\tilde{\nabla}\tilde{h} \cdot \tilde{\nabla}\tilde{h} \ll 1 \Rightarrow \sqrt{1 + (\nabla h)^2} \approx 1$ and we can approximate Equation (2.5) as:

$$\tilde{\nabla} \cdot \tilde{\nabla}\tilde{h} = \tilde{\nabla}^2 \tilde{h} = \text{Bo } \tilde{h}. \tag{2.7}$$

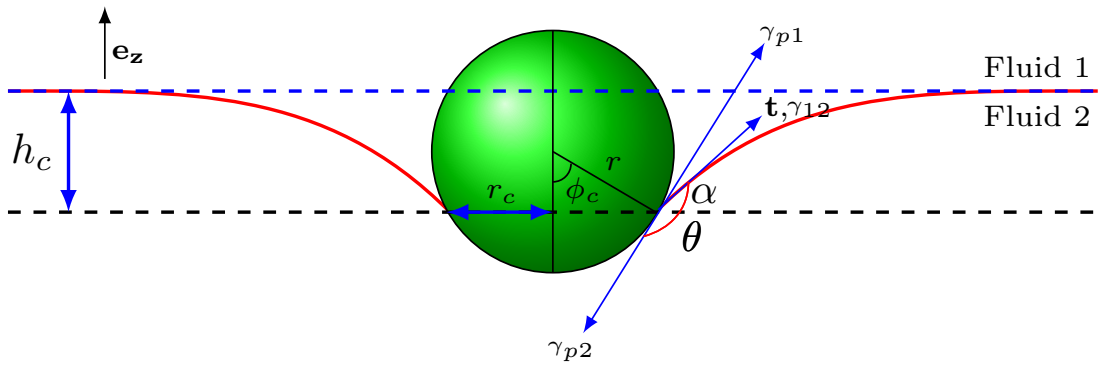

FIGURE 2.1: A heavy particle with finite Bond number adsorbed at the interface between fluid 1 and fluid 2. r_c is the height of the contact line — the position where the fluid-fluid interface meets the particle surface — h_c is the height of the interface (or contact line height) at that point, and ϕ_c is the contact-line angle. θ is the particle contact angle, measured with respect to fluid 2, α is the angle that the deformed fluid-fluid interface makes with the undeformed interface. γ_{1p}, γ_{2p}, and γ_{12} are the particle-fluid 1, particle-fluid 2, and fluid 1-fluid 2 surface tensions respectively. The vectors $\mathbf{t}$ and $\mathbf{e_z}$ are the tangent vector at the contact line and the undeformed interface normal, respectively, and r is the particle radius.

2.1.1 A Single Spherical Particle at a Fluid-Fluid Interface with a Finite Bond Number

A heavy spherical particle adsorbed at a fluid-fluid interface deforms the fluid-fluid interface due to its weight — imagine a bowling ball on a trampoline — as shown in Figure 2.1.

In equilibrium, the particle weight, $F_w = mg = F_\gamma + F_B$, balances with the buoyancy force, F_B, and surface tension force F_γ. The buoyancy forces are given by

$$F_B = \rho_1 V_{p1} g + \rho_2 V_{p2} g - (\rho_1 - \rho_2)\, g h_c A_c \tag{2.8}$$

where $V_{p1} = \frac{4}{3}\pi r^3 - V_{p2}$ and $V_{p2} = \frac{1}{3}\pi r^3(2 - 3\cos\phi_c + \cos^3\phi_c)$ are the particle volumes immersed in fluid 1 and fluid 2, respectively, and $A_c = \pi(r\sin\phi_c)^2$ is the area enclosed by the contact line. The first two terms of Equation (2.8) are simple buoyancy terms related to the displacement of the respective fluids by the particle. The particle depresses the interface, and the third term accounts for the increase in hydrostatic pressure due to this deformation.

The surface tension force is given by

$$F_\gamma = \gamma_{12} \oint \mathbf{t} \cdot \mathbf{e_z}\, ds \tag{2.9}$$

where $\mathbf{e_z}$ is the undeformed interface normal parallel with the z-axis and $\mathbf{t}$ is the tangent vector to the interface at the point where it contacts the particle. For the surface tension force to be non-zero and balance the weight of the particle, the angle between the tangent vector $\mathbf{t}$ and the undeformed surface normal $\mathbf{e_z}$ must be non-zero. In other words, the surface must deform to accommodate the weight of the particle, as illustrated in Figure 2.1.

We can parametrise the contact line circle as $\mathbf{c}(s) = (r_c \cos s, r_c \sin s)$ where r_c is the contact line radius, and the integral in Equation (2.9) evaluates to $F_\gamma = 2\pi\gamma_{12} r_c \sin\alpha$, where α is the angle between the contact line tangent vector $\mathbf{t}$ and the undeformed interface (Figure 2.1). If the interface slope is small, then $\mathbf{t} \approx \frac{\partial h}{\partial r}|_{r=r_c}$ and Equation (2.9) becomes

$$F_\gamma = \gamma_{12} \oint \nabla h \cdot \mathbf{e_z}\, ds. \tag{2.10}$$

Substituting the above mentioned quantities (and $m = \frac{4}{3}\pi r^3 \rho_p$) into the force balance equation yields:

$$\sin\alpha = -\frac{Bo}{6}\left[4\frac{\rho_p - \rho_1}{\rho_2 - \rho_1} - (1-\cos\phi_c)^2(2-\cos\phi_c) + 3\frac{h_c}{r}\sin^2\phi_c\right] \tag{2.11}$$

Since $0 \leq \sin\alpha \leq 1$ for a heavy particle ($\rho_p > \rho_2 > \rho_1$), Equation (2.11) omits no solution if the Bond number Bo is too large i.e. if gravitational forces are much stronger than surface tension forces and the particle detaches from the interface. Similarly, if the Bond number tends to zero (e.g. for a very small or light particle) the deformation of the interface due to the particle can be neglected.

Danov et al. [75] suggested that an asymmetric electric field around a charged particle adsorbed at a fluid-fluid interface due to large differences in electric permittivity of the two fluids could also deform the interface in a manner similar to gravity. This so-called electrodipping force can exist even for particles with negligible Bond numbers.

Finding the height profile of the interface, h_c, then involves solving Equation (2.7). In the limit of small Bond numbers $L_c \gg R_p$ and defining a quantity $H(r) = h(r) - h(\infty) = h(r) - h_\infty$, which represents the interface height minus the far-field contribution, Equation (2.7) becomes

$$\nabla^2 H = \frac{H}{L_c^2} \tag{2.12}$$

Taking into account the azimuthal symmetry of the problem, Laplace's equation in cylindrical coordinates is:

$$\frac{\partial^2 H}{\partial r^2} + \frac{1}{r}\frac{\partial H}{\partial r} = \frac{H}{L_c^2}. \tag{2.13}$$

This is a Bessel type equation that yields solutions in terms of modified Bessel functions of the second kind of order m, K_m:

$$H(r) = A_0 K_0\left(\frac{r}{L_c}\right) + \sum_{m=1}^{\infty} A_m K_m\left(\frac{r}{L_c}\right)\cos\left(m\left(\psi - \psi_{0,m}\right)\right) \tag{2.14}$$

where A_m and $\psi_{0,m}$ are constants of integration. The $m = 0, 1, 2$, and 3 terms are respectively called the monopole, dipole, quadrupole, and hexapole terms in analogy with electrostatics. The monopole term describes the vertical displacement of the contact line due to external forces such as gravity or the electrodipping force. The dipolar term relates to the rotation of the contact line due to external torques. The quadrupolar and higher order terms give information about the shape of the contact line itself.

In the case of a heavy spherical particle at an interface, we neglect terms $m \geq 1$ since the $m = 0$ monopolar mode is the leading order term.

Using the fact that $\frac{d}{dr}K_0\left(\frac{r}{L_c}\right) = -\frac{1}{L_c}K_1\left(\frac{r}{L_c}\right)$, that the interface height at the contact line is defined to be zero $h(r_c) = h_c = 0$, and that the contact line at infinity h_∞ is unknown such that $H(r) = h(r) - h_\infty = 0$, it follows that $h_\infty = -H(r_c)$. Combined with the contact-line boundary condition $F_\gamma = 2\pi r_c \gamma_{12} \partial_r H(r)|_{r=r_c}$ (Equation (2.10)), the general solution of Equation (2.13) is:

$$h(r) = \frac{F_\gamma L_c \left[K_0\left(\frac{r_c}{L_c}\right) - K_0\left(\frac{r}{L_c}\right)\right]}{2\pi r_c \gamma_{12} K_1\left(\frac{r}{L_c}\right)} \tag{2.15}$$

If the distance is much less than the capillary length $r \ll L_c$, then $K_m(\frac{r}{L_c}) \propto \left(\frac{L_c}{r}\right)^m$ for $m \geq 1$, and $K_0(\frac{r}{L_c}) \to \log\left(\frac{2L_c}{r}\right) - \gamma_E$, where γ_E is the Euler-Mascheroni constant. In this limit, the solution of Laplace's equation in Equation (2.14) reduces to a multipole expansion analogous to 2D electrostatics [76]. Using the above, we obtain:

$$h(r) = \frac{F_\gamma L_c \left[\log\left(\frac{2L_c}{r_c}\right) - \gamma_E - \log\left(\frac{2L_c}{r}\right) + \gamma_E\right]}{2\pi r_c \gamma_{12} \frac{L_c}{r_c}} \tag{2.16}$$

$$= \frac{F_\gamma}{2\pi\gamma_{12}} \log\left(\frac{r}{r_c}\right) \tag{2.17}$$

2.1.2 Capillary Interactions between Finite Bond Number Spherical Particles

Nicolson [77] calculated the interaction energy between buoyant bubbles at fluid-fluid interfaces and Chan et al. [78] extended this work to calculate the interaction energy, E_{AB}, between two finite Bond number spherical particles A and B:

$$E_{AB} = -2\pi\gamma_{12} R_A R_B Bo_A Bo_B Q_A Q_B K_0(\frac{r_{AB}}{L_c}) \tag{2.18}$$

where R_i are the particle radii, Bo_i are the particle Bond numbers, and $Q_i = \frac{2}{3}\frac{\rho_p - \rho_1}{\rho_2 - \rho_1}|_i - \frac{1}{3} - \frac{1}{2}\cos\phi_c + \frac{1}{6}\cos\phi_c^3$ is a parameter that determines how the particle Bond number affects the slope of the interface. In the context of this thesis, it is interesting to note that

several papers have confirmed this relationship using lattice Boltzmann simulations [79–81].

The interactions modelled by Nicolson [77] and Chan et al. [78] describe bubbles elevating the interface and particles depressing the interface in a monopolar, symmetric manner. When the deformations of individual particles or bubbles overlap, a $\frac{1}{r}$ lateral force develops between them, causing them to aggregate. These capillary forces are responsible for forming bubbles rafts and aggregating heavy particles at fluid-fluid interfaces — the so-called Cheerio's effect [82] — but there is no preferred orientational order between the bubbles or particles as they attract each other.

2.1.3 Irregular Contact Lines

From the above analysis, we can conclude that for particularly small or light particles in which surface tension forces dominate gravitational forces, capillary interactions between such particles should not exist, since the interface remains undisturbed. However, Lucassen [83] showed that if the contact line where the particle and fluid-fluid interface meet undulates, capillary interactions can occur. He argued that in reality, contact lines will almost always undulate due to, for example, surface roughness or anisotropic surface chemistry, and hence capillary interactions between particles will exist even in the absence of gravitational effects.

Stamou et al. [12] attempted to explain puzzling experiments that showed negatively charged polystyrene particles attracting each other and clustering with inter-particle distances in the micrometer range, defying known pair potentials at the time [84–87]. They argued that van der Waals forces are too small $E_{\text{vdw}} \approx (0.1 - 0.6)k_BT$ for particle separations $r_{AB} \geq 1\mu m$ and capillary forces due to particle weight (Section 2.1.2) were insufficient to account for the long-ranged attraction between particles [78]. They considered the effect of an undulated contact line around spherical particles, as suggested by Lucassen [83], which may arise due to surface roughness or complex surface chemistry. We review the theoretical ideas underpinning this work in detail, since many subsequent studies extend this analysis and I do so in Appendix B.

In order to study the pair interaction energy between two particles, we must find the excess surface area created by a single particle due to its undulating contact line. Stamou

et al. [12] invoked the small slopes argument (Equation (2.7)) and neglected gravity since all lengths are smaller than the capillary length $L < L_c = 2.7\text{mm}$. In this case, finding the interface deformation due to the presence of a particle with an undulated contact line reduces to solving Laplace's equation $\nabla^2 h = 0$, which the authors do in cylindrical coordinates. The solution is given by Equation (2.14), where we take the limiting form of the modified Bessel functions, yielding multipole solutions of the form:

$$H(r) = \sum_{m=2}^{\infty} H_m \left(\frac{r_c}{r}\right)^m \cos\left(m\left(\psi - \psi_{0,m}\right)\right) \tag{2.19}$$

They neglect the gravity ($m = 0$) and the external torque ($m = 1$) terms due to the absence of any external forces or torques. The leading order term is then the quadrupole term:

$$h = H\cos(2(\psi - \psi_0))\left(\frac{r_c}{r}\right)^2 \tag{2.20}$$

where H is the maximal contact line height, ψ_0 is the particle "bond angle", and r_c is the contact radius where the interface meets the particle surface, which is approximately equal to the particle radius for contact angles near 90°.

The excess surface area δS is the difference between the real surface area S^* and the projected surface area S. They use a local coordinate system rotated so that the slope maximum occurs in the y-direction such that $dx^* = dx$. In this coordinate system, $dy^* = \sqrt{dy^2 + dh^2} = dy\sqrt{1 + (\nabla h)^2} \approx dy\left(1 + \frac{1}{2}(\nabla h)^2\right)$. Therefore, $d(\delta S) = dS^* - dS = dx^*\, dy^* - dx\, dy = dx\, dy\, \frac{1}{2}(\nabla h)^2$ and it follows that:

$$\delta S = \frac{1}{2}\int_{r=r_c}^{\infty}\int_{\psi=0}^{2\pi} (\nabla h)^2 r\, d\psi\, dr. \tag{2.21}$$

We find that $\nabla h \cdot \nabla h = 4H^2 r_c^4 r^{-6}$ (a similar calculation is carried out in Appendix B) and the self-energy of the particle is therefore:

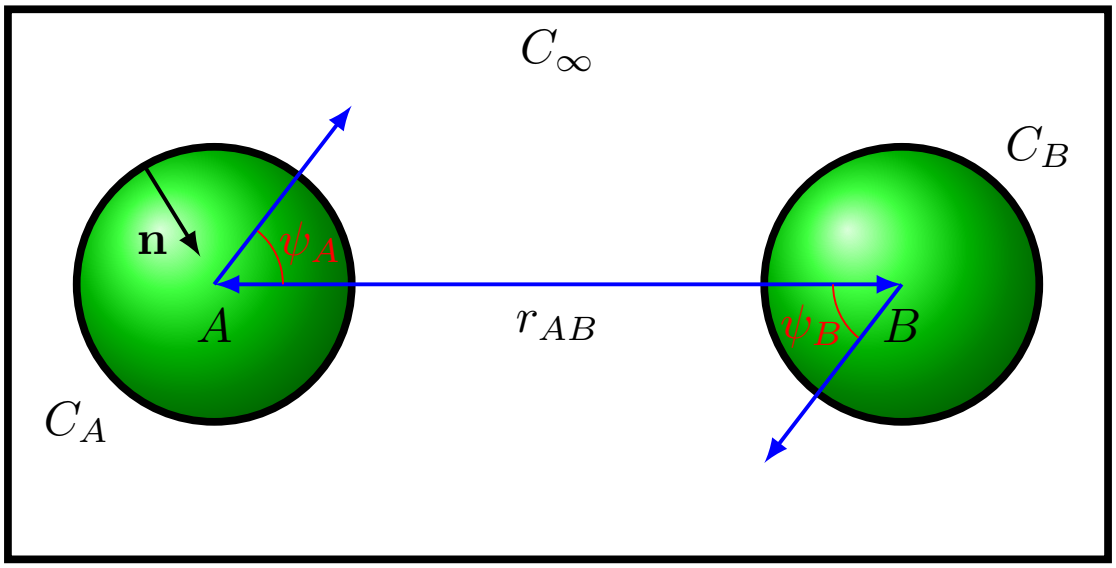

FIGURE 2.2: Schematic of the theoretical system considered by Stamou et al. [12]. Two particles A and B with contours C_A and C_B, respectively, are separated by a distance r_{AB}. The particles have a unit normal $\mathbf{n} = -(\cos\psi, \sin\psi)$ directed towards their centres. The polar angles ψ_A and ψ_B are defined with respect to the vector $\mathbf{r_{AB}}$ joining their centres, such that $\psi_A = -\psi_B$ corresponds to a mirror symmetric configuration. The interface boundary contour at infinity is C_∞.

$$\delta E = \gamma_{12}\delta S = \pi\gamma_{12}H^2. \tag{2.22}$$

Stamou et al. [12] showed that if their micron-sized particles have a contact line hysteresis of just $\Delta\theta_c = 10^\circ$ the contact line height difference is $H \approx \frac{1}{2}R\Delta\theta_c = 50\text{nm}$, resulting in a self-energy of $\delta E \approx 10^5 k_B T$.

The interaction energy between two particles A and B separated by a distance r_{AB} is $\delta E_{AB} = \gamma\left(\delta S_{AB} - \delta S_A - \delta S_B\right)$, where S_{AB} is the interface area around the two particles and $S_{A,B}$ is the interface area around the isolated particles.

In order to calculate S_{AB} they assumed that the interface deformation at particle A due to particle B is small, and vice versa, such that they could invoke the Nicolson superposition principle [77] and suggest that the total interface deformation, h_{AB}, is just the sum of the individual particle deformations: $h_{AB} = h_A + h_B$. Inserting this assumption into Equation (2.21) and Equation (2.22) then gives

$$\begin{aligned}\delta E_{AB} =& \frac{\gamma}{2}\int (\nabla h_A + \nabla h_B)^2\, dS - \frac{\gamma}{2}\int (\nabla h_A)^2\, dS - \frac{\gamma}{2}\int (\nabla h_B)^2\, dS \\ =& \gamma \int \nabla h_A \cdot \nabla h_B\, dS \\ =& \int_C h_B(\mathbf{n}\cdot\nabla h_A)\, dC - \int_S h_B(\nabla^2 h_A)\, dS \\ =& 2\int_{C_B} h_B(\mathbf{n}\cdot\nabla h_A)\, dC \end{aligned} \tag{2.23}$$

where we have used Green's theorem and the fact that $\nabla^2 h_A = 0$. The factor of two arrives from the symmetry of the problem and the superposition approximation: the interface deformation at particle A due to particle B is equal to the interface deformation at particle B due to particle A. Since the integrand scales as $\sim r^{-5}$, the integral over the surface boundary at infinity C_∞ can be neglected. $\mathbf{n} = -(\cos\psi, \sin\psi)$ is a unit vector pointing towards the particle centres (Figure 2.2).

Finally, the authors assume that the particle-particle separation r_{AB} is much larger than the contact line radius r_c so that the field ∇h_A at the boundary C_B can be Taylor expanded $\nabla h_A(\mathbf{r}) \approx \nabla h(\mathbf{0}) + \mathbf{r}\cdot(\nabla\otimes\nabla)h_A(\mathbf{0})$, where $\mathbf{r} = (r_B\cos\theta_B, r_B\sin\theta_B)$ is a vector pointing from the centre of particle B.

The integral in Equation (2.23) can then be solved (using the methods of Appendix B) to give:

$$\begin{aligned}\delta E_{AB} &= -12\pi\gamma H^2 \cos(2\psi_A + 2\psi_B)\left(\frac{r_c}{r_{AB}}\right)^4 \\ &= -12\cos(2\psi_A + 2\psi_B)\left(\frac{r_c}{r_{AB}}\right)^4 \delta E \end{aligned} \tag{2.24}$$

Particles in a mirror symmetric configuration $\psi_A = -\psi_B$ minimise the interaction energy. For typical micron sized particles with contact line deviations of just 50nm capillary interactions are stronger than thermal fluctuations for particle-particle separations upto 15μm. For particle-particle separations of 2 micrometres, the interaction energy is $\delta E_{AB} \approx 10^4 k_B T$.

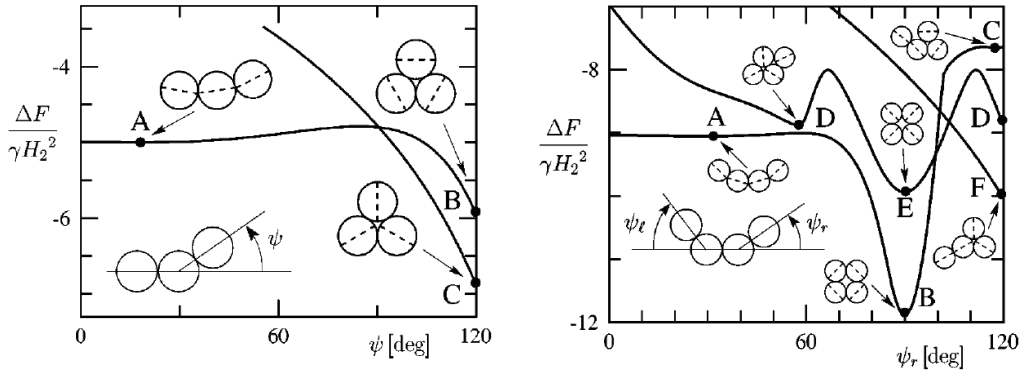

(A) (B)

FIGURE 2.3: (A) Fournier and Galatola [13] obtained the free energy landscape of 3 particles by keeping two particles in contact and rotating a third by an angle ψ around them. The radial triangular configuration at position C is the ground state. (B) The position of three particles is fixed through the angle ψ_r and then minimised with respect to ψ_l. The orthoradial configuration at position B is the ground state, with the radial configuration at position E being the next lowest in energy. Monolayers of these particles should produce squares lattices with either orthoradial (B) or radial (E) configurations. Reprinted figures with permission from [13] Copyright (2002) by the American Physical Society.

When combined with an r_{AB}^{-3} dipole-dipole repulsion between the particles, the quadrupolar capillary interaction explains several of the qualitative features seen in experiment [84–87].

Danov et al. [88] extended the analysis of Stamou et al. [12] to include pair interactions arising from undulating contact lines for multipoles of arbitrary order (i.e. dipoles, quadrupoles, hexapoles etc.) and mixed multipole interactions (e.g. dipole-quadrupole) by repeating the above analysis in bipolar coordinates. Additionally, their exact analytical expressions are valid for any particle-particle separations $r_A + r_B < r_{AB} < \infty$. Danov and Kralchevsky [89] used these results to calculate the shear elasticity of monolayers of particles acting via capillary multipoles, and predicted that such monolayers should behave as 2D elastic solids, rather than fluids.

Fournier and Galatola [13] were the first to come up with an exact many-body interaction calculation of polar capillary multipoles. For two particles, their results reiterated previous results concerning the pair interaction, namely that a mirror symmetric configuration minimises the interaction energy for a given particle-particle separation. However, including a constant non-zero octupolar term lifts this degeneracy and favours tip—tip alignment of particles, in agreement with the findings of Brown et al. [14].

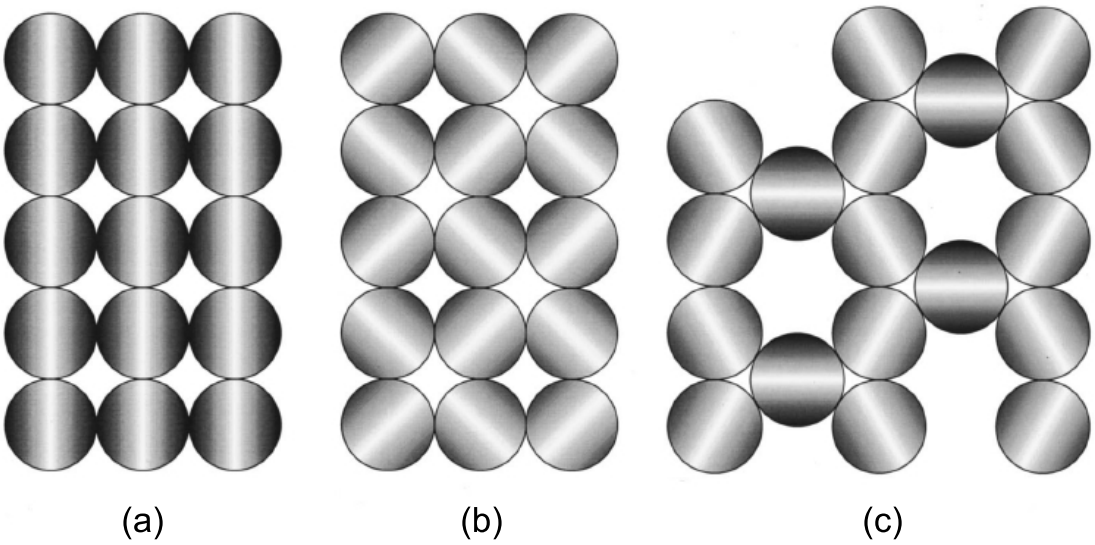

FIGURE 2.4: Possible lattice structures for tightly packed quadrupole particles assuming that each particle pair maintains mirror symmetry $\psi_A = -\psi_B$ [14]. (b) is the orthoradial structure later confirmed by Fournier and Galatola [13] and (c) introduces defects in order to fulfil the mirror symmetry condition. Reprinted with permission from [14]. Copyright (2000) by the American Physical Society.

For three particles, they fixed the position of two particles and rotated the other particle by an angle ψ around the original two particles (Figure 2.3a) and minimised each configuration with respect to rotations of the individual particles. The ground state is the radial, triangular cluster at position C in the free energy landscape. In some respects the most intriguing result is the existence of the bent chain at position A — a purely many-body effect — since pairwise interaction potentials predict a straight chain with maximum distortion axes (dashed lines) parallel to each other. For four particles (Figure 2.3b), the orthoradial (B) rather than radial (E) configuration is the ground state, suggesting that these structures should be the building blocks of square lattices at interfaces. Again, bent chains (A) represent a local minimum that results purely from many-body capillary interactions. The analysis of Fournier and Galatola [13] shows that superposition approximation is inaccurate in the near-field, where many-body effects and higher-order multipoles play an important role.

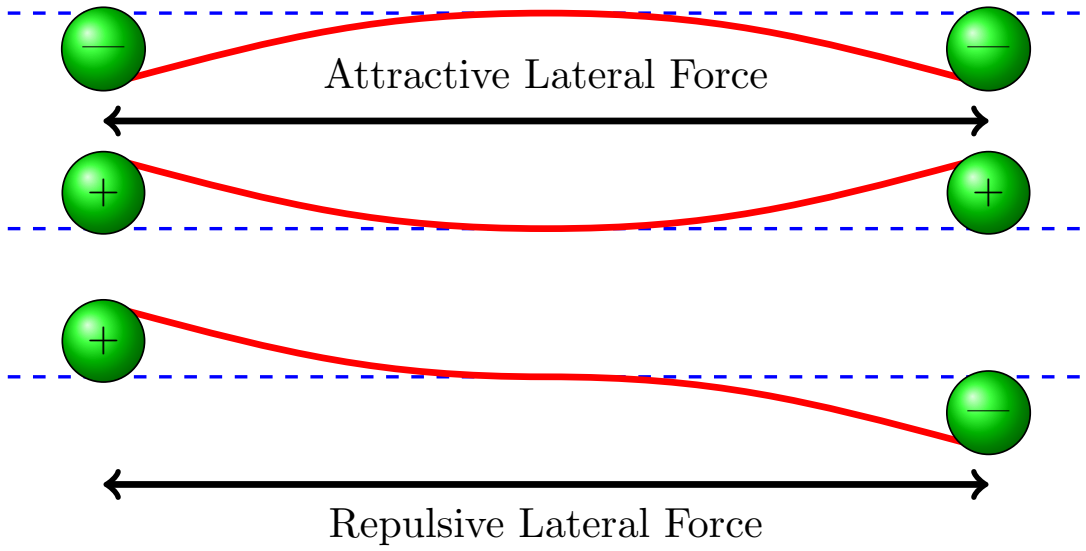

FIGURE 2.5: Like capillary charges attract and unlike capillary charges repel.

2.1.4 Using Capillary Interactions to Direct Assembly

Bowden et al. [90] were the first to highlight the utility of using capillary interactions for directed assembly of particles at fluid-fluid interfaces. They used millimetric complex shaped particles, which therefore have a finite Bond number. The particles assembled into well defined configurations and shapes depending on the chosen particle shapes and properties. Their results demonstrated that capillary interactions can be used to manufacture *a priori* desired structures by varying the particle properties — such as shape, mass, wettability, and surface chemistry — alone.

Brown et al. [14] fabricated much smaller particles than Bowden et al. [90] using photolithography, meaning the bond numbers of the particles was negligible so that the quadrupolar mode should be the first dominant deformation contribution. They experimentally studied disk-shaped particles that curved out of plane with a hydrophilic and hydrophobic side, and confirmed that the interface deformation produced by a single particle was approximately quadrupolar. They also highlighted the possible lattice structures that might form in monolayers of quadrupolar particles that are subjected to the constraint $\psi_A = -\psi_B$ (Figure 2.4). Note the necessary introduction of voids in Figure 2.4c in order for each particle pair to maintain mirror symmetry. However, they also observed particles forming chains that could only be explained by the presence of higher order multipoles, which was later corroborated by Fournier and Galatola [13].

Finally, Nierop et al. [91] showed that, even in the absence of gravity and contact line undulations caused by surface roughness, if a particle is slightly non-spherical its contact line deforms and leads to strong capillary interactions between particles. They investigated monolayers of weakly eccentric particles using traditional molecular dynamics algorithms with a pair-potential assuming small interface slopes and superposition of particle deformations. They found that particles form dendritic/fractal structures if they stick upon contact, and form a hexagonal array with herringbone orientational order if the particles do not stick together upon contact.

These studies highlight the utility of using anisotropic capillary interactions in order to control the preferred orientation of particle assembly. The key point is that like interface deformations attract, and unlike deformations repel (Figure 2.5). Particles may then assemble into desired structures by carefully choosing how the particle deforms the interface; this can be done by altering particle properties such as mass, surface chemistry, and shape. In the next section, we discuss capillary interactions between anisotropic particles in detail.

2.2 Anisotropic Particles

Loudet et al. [15] were the first to investigate the behaviour of ellipsoidal (prolate spheroidal) particles adsorbed at a fluid-fluid interface. They found a long-ranged (several times the particle long axis radius, $R_{\parallel}$) attractive force between ellipsoidal particles that was very large compared to the thermal energy, k_BT. They ruled out van der Waals forces for similar reasons to Stamou et al. [12]: they decay quickly and are much smaller than k_BT for particle separations greater than a micrometer [92].

They also ruled out electrostatic forces since they are usually repulsive, and the ellipsoidal particles only repelled each other in contact. They speculated that the cause of the attractive forces, which are orders of magnitude greater than k_BT, could be due to nanometre-sized contact line undulations as reported by Stamou et al. [12], since the attractive forces showed power-law behaviour consistent with capillary quadrupoles.

They also found that the long-ranged attraction depended crucially on the particle shape; in order to make ellipsoidal particles, they stretched spherical particles, therefore,

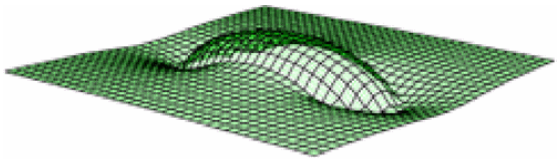

FIGURE 2.6: Interface deformation profile around an ellipsoidal particle. The particle depresses the interface more at the tips than it elevates the interface at the sides [15]. Reprinted figure with permission from [15] Copyright (2005) by the American Physical Society.

the spherical particles and ellipsoidal particles have similar surface chemistry. Yet the spherical particles did not exhibit long-ranged attraction.

The ellipsoidal particles tended to arrange into open-structures and chains rather than lattices. Further, surface chemistry — which is partly responsible for the particles' wettability — appears to play an important role: polystyrene (PS) ellipsoidal particles preferred to align tip—tip, but silica (Si) ellipsoidal particles preferred to align side—side. In order to understand this behaviour better, they observed the interaction of pairs of isolated ellipsoidal particles in both tip—tip and side—side orientations. After contact, the Si particles rearranged into the side—side configuration.

They found that for both PS and Si ellipsoidal particles, the interaction force, F, varied with respect to centre-centre separations r_{AB} as $F_{\text{side}} \propto r_{AB}^{-4.1}$ and $F_{\text{tip}} \propto r_{AB}^{-5.0}$ for ellipsoidal particles approaching in the side—side and tip—tip orientation, respectively.

They solved Laplace's equation with the appropriate boundary conditions assuming no gravity, constant particle contact angle, and small slopes, and found that ellipsoidal particles deform the interface more strongly in the long-axis direction than the short-axis direction, as shown in Figure 2.6. Nevertheless, the interface still shows a quadrupolar symmetry and since spherical quadrupoles should interact with a force $F \propto r_{AB}^{-5}$ they tentatively concluded that the particles behave as capillary quadrupoles.

Loudet et al. [93] followed up this study by experimentally imaging the contact line using interferometry and confirmed a quadrupolar interface deformation. They additionally confirmed that the interface depressions at the tips of the particle were greater than the interface elevations at the sides.

Lehle et al. [94] analysed the interaction of two ellipsoidal particles analytically by assuming small interface deformations and solving Laplace's equation $\nabla^2 h = 0$ in terms

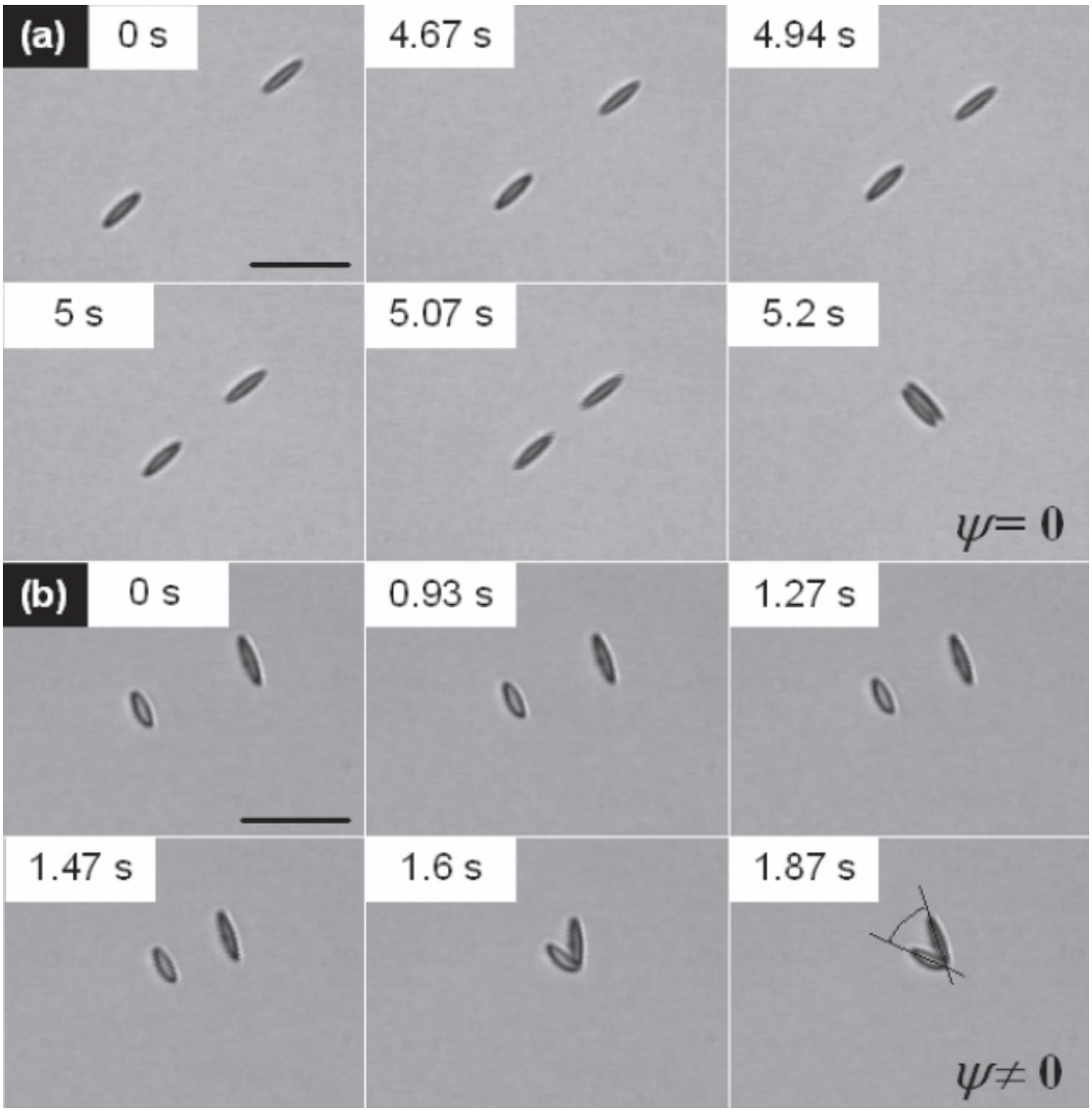

FIGURE 2.7: (a) The ellipsoids have equal aspect-ratio, α, and long-axis radii, $R_\perp$. After approaching in the tip—tip orientation, the particles re-orient into the side—side configuration. (b) Particles of different sizes: once in contact, the particles arrange into capillary arrows with a finite angle, ψ, between their axes. Capillary arrows are a many-body effect that cannot be explained using simple far-field pair potentials [16]. Reprinted from Ref. [16] with permission.

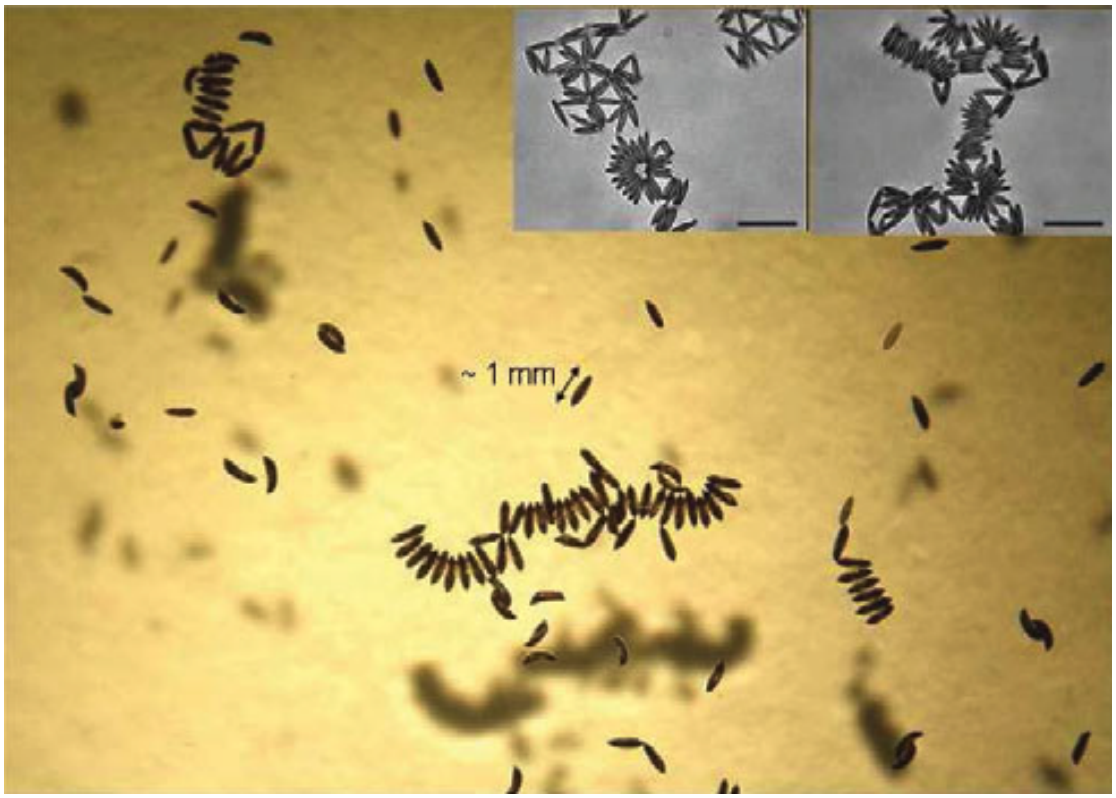

FIGURE 2.8: The structures formed by mosquito eggs on water surfaces. Gravitational effects can be neglected, and the observed structures are due to quadrupolar capillary interactions between the particles. Curved chains and triangular structures can clearly be seen. Reprinted from Ref [17] with permission from Springer.

of elliptic multipoles. They found that close to the particle, polar multipoles (an elliptic multipole of order m is a superposition of polar multipoles of order $n \geq m$) higher than the quadrupole contribute significantly to the interface deformation. They showed that for interparticle distances $d < 4R_{\parallel}$, where $R_{\parallel}$ is the long-axis radius of the ellipsoidal particle, the capillary force deviates significantly from the expected far-field capillary force, $F_{\text{cap}} \propto r_{AB}^{-5}$. Effective power law exponents for inter-particle distances $d < 4R_{\parallel}$ would be > -5 and < -5 for the side—side and tip—tip configurations [95], respectively, consistent with the experimental observations made by Loudet et al. [15].

Lehle et al. [94] also investigated the maximum height difference Δh_c along the contact line. They found that Δh_{max} depends on both the aspect-ratio of the ellipsoidal particles, α, and the contact angle, θ. The maximal height difference Δh_{max} increases as the particle aspect-ratio increases, but the contact-angle at which the peak Δh_{max} occurs decreases as the aspect-ratio increases. Δh_{max} is zero for neutrally wetting ($\theta = 90°$) and completely wetting particles ($\theta = 0°$ or $180°$). These findings have recently been

corroborated using Surface Evolver simulations [96].

Loudet and Pouligny [16] later investigated the assembly of ellipsoidal particles with mismatched aspect-ratios and/or long-axis radii, $R_{\perp}$. They found that when ellipsoidal particles had equal aspect-ratios and long-axis radii, the particles always adopted the side—side configuration once in contact regardless of whether or not they approached in the side—side or tip—tip state, suggesting that the side—side state is a free energy minimum.

However, if the aspect-ratios are not equal, the particles formed "capillary arrows" in which there was a finite angle, ψ, between the ellipsoidal particles' long-axes, irrespective of whether they approached each other in the side—side or tip—tip state, as shown in Figure 2.7. These capillary arrows then drifted and moved on the interface as a rigid-body, even when interacting with other capillary arrows (until contact).

Interestingly, their study provided some of the first direct evidence that the contact lines of ellipsoidal particles are not pinned: the contact lines move in response to interactions with interface deformations caused by other particles. Their theoretical analysis showed that unequal sized ellipsoidal particles begin to repel each other at small centre-centre separations if they approach in the side–side state, confirming their observations in Figure 2.7. Additionally, their theoretical calculations confirmed that there is an energy minimum at a finite angle ψ for unequal ellipsoidal particles in contact. Intriguingly, the capillary arrow structure produces an effective dipolar interface deformation.

They concluded that the existence of capillary arrows cannot be explained using the far-field pair potential and must be a many-body effect, similar to the conclusions of Fournier and Galatola [13] with regards to the bent particle chains (Figure 2.3).

Loudet and Pouligny [17] further extended this theoretical analysis in a bid to explain the structures formed by mosquito eggs on the surface of ponds (Figure 2.8). For three equal sized ellipsoids, a capillary triangle, as frequently seen in Figure 2.8, is slightly higher in energy than three ellipsoids arranged in the side-side configuration. The existence and stability of these capillary triangles suggests that an energy barrier prevents the particles from re-arranging into the lower energy side—side state.

Lewandowski et al. [18] derived a pair potential between elliptical quadrupoles. They found that for interparticle separations $r_{AB} > \sqrt{2}R_{\parallel}$, the tip—tip state is lower in energy,

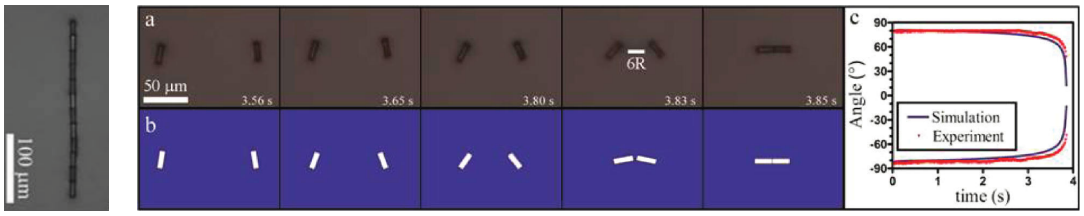

(A) (B)

FIGURE 2.9: (A) Cylindrical particles form rigid tip—tip chains. (B) Two cylindrical particles during approach. Initially, the particles attract in a mirror symmetric configuration $\psi_A = -\psi_B$. As the particles get closer, a torque rotates them into their lowest energy tip—tip state. Once in contact, the particles remain in the tip—tip state. Reprinted (adapted) with permission from [18]. Copyright (2010) American Chemical Society.

and for $r_{AB} < \sqrt{2}R_{\parallel}$, the side—side state is lower in energy, in agreement with Lehle et al. [94] ($r_{AB} = \sqrt{2}R_{\parallel}$ corresponds to tip—tip contact between the particles).

The particles experience a torque, T, to rotate them into their lowest energy configuration that decays with the inter-particle separation, r_{AB}, as $T \propto r_{AB}^{-6}$: for separations $r_{AB} > 2R_{\parallel}$, the torque rotates them into the tip—tip configuration, for separations $r_{AB} < 2R_{\parallel}$, the torque rotates them into the side—side configuration. The elliptical quadrupole decays into a polar quadrupole at large particle-particle separations, meaning that particles attract in a mirror-symmetric configuration, $\psi_1 = -\psi_2$, in agreement with Stamou et al. [12]. However, there is zero torque if the particles are originally in the side—side or tip—tip state, which reconciles with previous observations of the assembly of two ellipsoidal particles in which the particles maintain the side—side configuration during approach [15–17].

For cylindrical particles, they observed that the particles remain in the tip—tip state once in contact (Figure 2.9b), in contrast with ellipsoidal particles, which usually rotate into the side—side state, and that cylindrical particles form straight, rigid chains in which each particle is aligned tip—tip with its neighbouring particles (Figure 2.9a).

These findings led Botto et al. [19] to investigate the capillary interactions of non-neutrally wetting ellipsoidal and cylindrical particles in contact. In agreement with previous observations [15–17, 94], they found that the side—side state is the lowest energy state for ellipsoidal particles in contact, and that there is no energy barrier stopping ellipsoidal particles from rearranging into the side—side state. This explains why ellipsoidal particles rotate into the side—side state after they make contact with

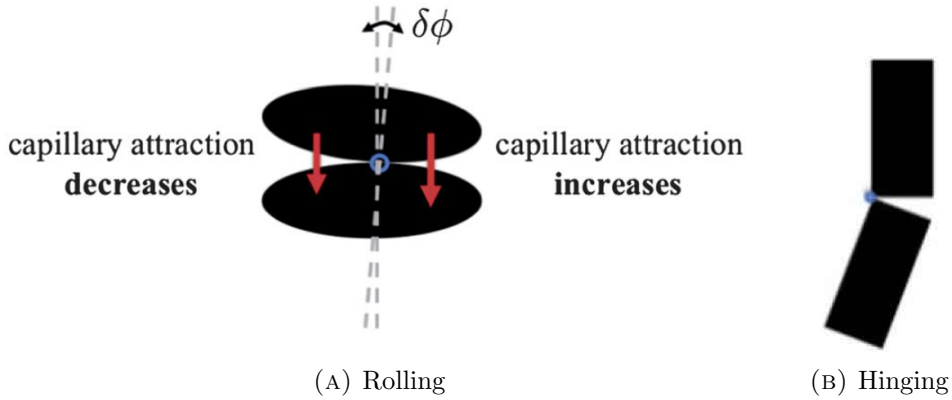

(A) Rolling (B) Hinging

FIGURE 2.10: (A) Small bond angle deviations give rise to a linear torque regime. (B) Corner sharpness is the source of the free energy barrier separate the tip—tip and side—side states between cylindrical particles. Reproduced (Adapted) from [19] with permission of The Royal Society of Chemistry.

each other, even if they approach tip—tip [15, 17]. Botto et al. [19] found an elastic torque regime for bond angles $\phi < 45°$ and suggested that this is the reason ellipsoidal particle chains can curve: a small change in bond angle produces an increase in the capillary energy on one tip of the particle but an identical decrease on the other tip so that the particles can easily "roll" around each other (Figure 2.10a).

In contrast, for cylindrical particles, the lowest energy configuration is the tip—tip state, and there is a free energy barrier separating the tip—tip and side—side states that depends on the corner "sharpness" of the particles: smoother particle corners give rise to smaller energy barriers, until eventually, the free energy barrier disappears (i.e. in the limit that the cylindrical particles turn into ellipsoidal particles). The free energy barrier arises due to "hinging" around the sharp particle corners (Figure 2.10b). Therefore, sharp-edged cylinders remain in the tip—tip state after contact. However, if they do find themselves in the side—side state due to e.g. compression, they remain in that configuration due to the energy barrier inhibiting their rearrangement into the lower energy tip—tip state.

Monolayers of ellipsoidal particles are highly elastic when compared with spherical particles of similar surface chemistry [97, 98]. Madivala et al. [99] used this fact to manufacture very stable Pickering emulsions using ellipsoidal particles. The use of ellipsoidal particles for stabilised emulsions is an area of significant potential technological applications that has only just begun to be explored.

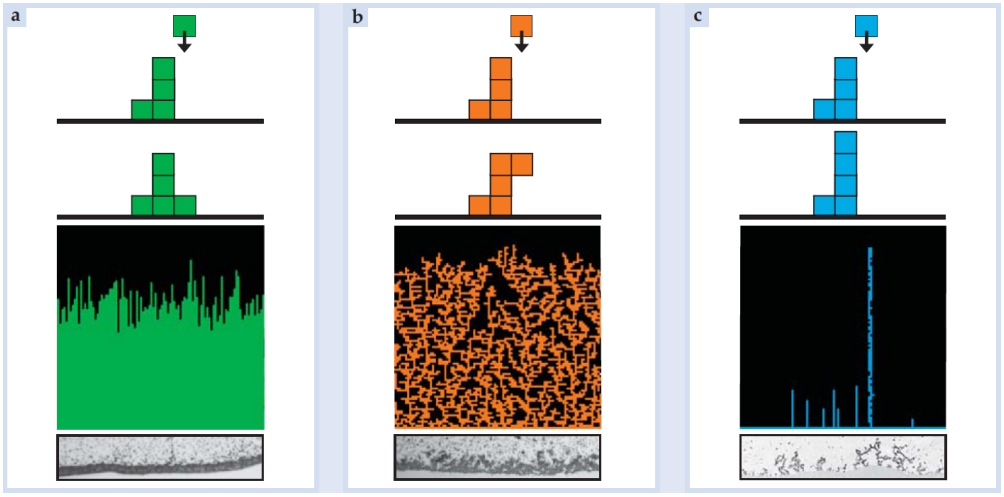

FIGURE 2.11: For spheres (a), each column of particles grows independently $\sim t^{\frac{1}{2}}$ according to a Poisson process. For ellipsoids (b), capillary interactions cause the particles to attract and stick together, and columns grow as $\sim t^{\frac{1}{3}}$ as per the KPZ equation. Finally, for highly anisotropic ellipsoids or cylinders (c), columns that contain particles grow larger, because the attraction is so strong that particles migrate to areas with other particles, and regions with fewer particles grow more slowly, so that the interface width grows as $\sim t^{0.68}$ [20]. Reproduced with permission from [20]. Copyright 2013, American Institute of Physics.

2.3 Applications of Capillary Interactions

2.3.1 Coffee Ring Effect

In the coffee ring effect, a droplet of fluid with suspended spherical particles dries on a substrate. The surface of the drop is a spherical air-water interface (ignoring the base of the droplet). As the droplet evaporates; the liquid volume is smaller at the edges of the droplet than in the centre, and the droplet edges pin and therefore do not recede, which means the edges of the droplet evaporate faster. Therefore, fluid flows to the droplet edges, and as it does so, transports spherical particles with it. This results in a thick build up of spherical particles at the droplet edge [100].

Replacing spherical particles with ellipsoidal particles suppresses the coffee ring effect [101]. During the evaporation process, some particles adsorb at the air-water interface. Once adsorbed, quadrupolar capillary interactions between ellipsoidal particles cause the particles to attract and stick to each other. This clumping prevents the particles from drifting all the way to the edge of the droplet, and also from tightly packing at the edge of the droplet if they make it there, inhibiting the coffee ring effect.

Interestingly, the coffee ring effect is a great way to test various universality classes of interface growth [102]. Figure 2.11 shows that the coffee ring width, W, grows with time according to $W \sim t^{\frac{1}{2}}$ for spherical particles and $W \sim t^{\frac{1}{3}}$ for ellipsoidal particles, an example of the Kardar-Parisi-Zhang (KPZ) Equation [103]. As the particle anisotropy increases further, the KPZQ (KPZ with quenched disorder) equation characterises the growth, $W \sim t^{0.68}$. In this case, regions with lots of particle attract even more particles, but regions with few particles grow slowly. These scaling laws have been observed in the interface growth of bacterial colonies [104] and the progress of fire on burning paper [105]. Therefore, these colloidal systems are excellent model systems for studying seemingly unrelated areas of physics.

2.3.2 Meniscus Climbing Insects

Water-walking insects utilise the surface tension of air-water interfaces in order to support their weight and walk on water. They use several different techniques to propel themselves on the water surface. However, when these insects wish to leave the surface of water for dry land they have to climb the menisci that exist where the water meets

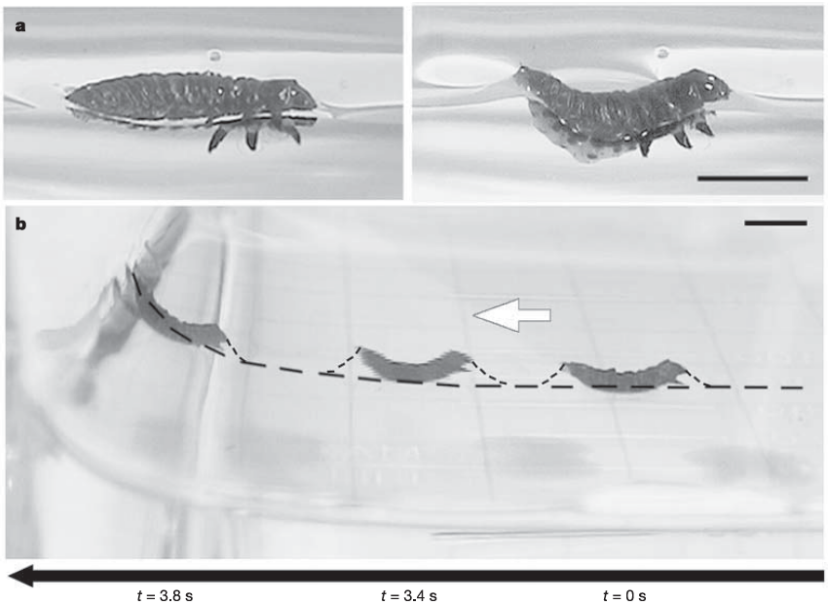

FIGURE 2.12: (a) The insect bends its body in order to deform the fluid-fluid interface, creating a positive capillary charge. The capillary charges of the meniscus and beetle match, and so an attractive lateral capillary force emerges. (b) The capillary force causes the insect to climb the meniscus. Reprinted by permission from Macmillan Publishers Ltd: Nature [21], copyright (2005).

the land. This is quite a challenge, since the menisci are effectively frictionless to these insects [21].

Some insects have developed methods to simply jump over the menisci and out of the water, but others use capillary interactions. By contorting their bodies or limbs in specific ways, these insects deform the water surface to create lateral capillary forces that attract them to the menisci at the water's edge [21]. Figure 2.12 shows a Waterlilly Leaf Beetle deforming its body to bend the water surface upwards creating a positive capillary charge that matches the menisci (Figure 2.5). Due to the matching capillary charges, an attractive lateral capillary force emerges between the insect and the meniscus and the insect travels up the meniscus with ease [21].

Chapter 3

The Lattice Boltzmann Method

3.1 Introduction

Traditional methods of simulating fluid flows have followed two paths: microscopic and macroscopic modelling. In microscopic modelling, we compute the forces on each individual fluid particle in the system and solve Newton's equations of motion for each particle to calculate the particles' trajectories. In order to resolve the motion of the particles properly, the simulation time-step must be smaller than the particle collision time scale. These so-called molecular dynamics simulations can become extremely computationally expensive depending on the number of particles we wish to model, the physical forces we wish to include, and the total time we wish to simulate. Additional difficulties arise if there are very few particles in the system (e.g. atomic clusters) because at low particle numbers bulk-properties such as temperature, pressure, viscosity, heat capacity, and thermal conductivity are undefined.

At the other extreme, in macroscopic (continuum) modelling we develop mass, momentum, and energy conservation equations for a control volume of fluid that is assumed to contain many particles. We then discretise these equations of motion in space and time in order to solve them computationally. Macroscopic approaches are more efficient than microscopic approaches computationally, in the sense that we are able to simulate larger systems for longer times, due to having fewer degrees of freedom. But we lose information about the behaviour of individual fluid particles due to the continuum approximation, which may be useful for certain applications.

The lattice Boltzmann equation is a mesoscopic method, bridging the length and time-scales between the microscopic and macroscopic modelling regimes. Lattice Boltzmann methods achieve this by modelling single particle distribution functions, encapsulating some of the principles of both microscopic and macroscopic modelling. One of the additional advantages of the lattice Boltzmann method is its parallelism: lattice Boltzmann is a completely local algorithm, which therefore allows efficient implementation on supercomputers. In this section, we overview the relevant ideas from microscopic and macroscopic modelling before introducing the lattice Boltzmann method as used in this thesis and its connection with microscopic and macroscopic modelling.

3.2 Microscopic Modelling / Molecular Dynamics

Microscopic techniques revolve around solving Newton's equations of motions for individual particles in a system and evolving the trajectories of those particle in time. The force on the i^{th} particle, F_i, in an ensemble of N particles is:

$$\sum F_i = m_i a_i \tag{3.1}$$

where m_i and a_i are the particle mass and acceleration respectively. The force sum on the left hand side involves calculating the force on particle i from all the other particles in the system and any external forces. The physics is contained in this force term: what physical forces should we include in the interactions between the particles? The computational cost of molecular dynamics simulations is dominated by this force term. Some interactions, in particular long-range electromagnetic interactions, can be computational expensive to calculate, and their expense scales with the number of particles in the system. This restriction places a natural restraint on the length and time scales that are accessible with molecular dynamics simulations.

Using the central difference approximation of a derivative for both the acceleration $a_i(t+\Delta t)\Delta t = v_i(t+\frac{1}{2}\Delta t) - v_i(t-\frac{1}{2}\Delta t)$ and velocity $v_i(t+\Delta t)\Delta t = x_i(t+\frac{1}{2}\Delta t) - x_i(t-\frac{1}{2}\Delta t)$, we can find the position $x_i(t+\Delta t)$ of the i^{th} particle at a time $t+\Delta t$ using the following integration scheme, known as the Leapfrog integrator:

$$
\begin{aligned}
v\left(t+\frac{1}{2}\Delta t\right) &= v\left(t-\frac{1}{2}\Delta t\right)+a(t)\Delta t \\
x\left(t+\Delta t\right) &= x(t)+v\left(t+\frac{1}{2}\Delta t\right)\Delta t.
\end{aligned}
\tag{3.2}
$$

There are several potential choices of integration schemes, but the Leapfrog algorithm is the one used in this thesis, as described in more detail later in this Chapter [106]. We can then calculate macroscopic quantities of interest such as the temperature and pressure provided there are enough particles in the system for these properties to be well defined. Molecular dynamics allows us to gain information about the motion of individual particles and the system microstructure. This kind of detail is unavailable with macroscopic modelling techniques.

3.3 Macroscopic Modelling and the Navier-Stokes Equations

Macroscopic modelling focusses on deriving conservation equations for a control volume of fluid assumed to contain many individual particles. We can then discretise these macroscopic equations in space and time and solve the resulting macroscopic equations, which are not necessarily local. Traditional computational fluid dynamics techniques therefore necessarily invest a great deal of effort in modelling the meshes used to discretise space and the relevant boundary conditions. Consequently, some flow geometries are too computationally expensive to compute or conceptually difficult to model at present.

3.3.1 The Continuity Equation

We can derive the continuity of mass equation by considering a simple differential control volume and calculating the conservation of mass flowing through that volume to obtain:

$$
\frac{\partial \rho}{\partial t}+\nabla\cdot(\rho\mathbf{v})=0. \tag{3.3}
$$

where ρ is the fluid density and $\mathbf{v}$ is the fluid velocity. This form of the continuity equations assumes that there are no sources or sinks of mass.

3.3.2 The Cauchy Momentum Equation

The Cauchy momentum equation models the conservation of momentum, and so we can make a simple substitution into Equation (3.3) $\rho \mapsto \rho\mathbf{v}$ to obtain $\frac{\partial \rho\mathbf{v}}{\partial t} + \nabla \cdot (\rho\mathbf{v} \otimes \mathbf{v}) = 0$. Using the fact that divergence of a tensor product is $\nabla \cdot (\mathbf{u} \otimes \mathbf{v}) = (\nabla \cdot \mathbf{u})\mathbf{v} + \mathbf{u} \cdot \nabla\mathbf{v}$, we obtain $\rho\frac{\partial \mathbf{v}}{\partial t} + \mathbf{v}\frac{\partial \rho}{\partial t} + \mathbf{v} \otimes \mathbf{v} \cdot \nabla\rho + \rho\mathbf{v}\nabla \cdot \mathbf{v} + \rho\mathbf{v} \cdot \nabla\mathbf{v} = 0$, and after some rearrangement and substitution of the mass continuity equation (Equation (3.3)) we arrive at Cauchy's momentum equation:

$$\rho\left(\frac{\partial \mathbf{v}}{\partial t} + \mathbf{v} \cdot \nabla\mathbf{v}\right) = 0 \tag{3.4}$$

Since Cauchy's momentum equation can be considered as $F = ma$ for a control volume (i.e. for body forces — forces per unit volume), this form of the equation assumes that there are no sources or sinks of momentum. In reality, we need to consider the sources and sinks that cause fluids to change their momentum and flow.

We can identify three types of force: body forces, $\mathbf{f}$, such as gravity, which act on the centre-of-mass of the control volume; pressure forces, ∇p, where p is the pressure, which act normal to the surfaces of the control volume, analogous to the "normal" force in regular Newtonian mechanics; and viscous or shear forces, $\nabla \cdot \boldsymbol{\tau}$, where $\boldsymbol{\tau}$ is a general stress tensor, which act parallel to the surfaces of the control volume, analogous to friction in Newtonian mechanics.

Adding these sources and sinks to the Cauchy momentum equation (Equation (3.4)) gives:

$$\rho\left(\frac{\partial \mathbf{v}}{\partial t} + \mathbf{v} \cdot \nabla\mathbf{v}\right) = -\nabla p + \nabla \cdot \boldsymbol{\tau} + \mathbf{f} \tag{3.5}$$

3.3.3 Compressible Navier-Stokes Equation

There is no general equation for the deviatoric stress tensor $\boldsymbol{\tau}$ or pressure p in Equation (3.5), so we have to come up with a so-called constitutive law that describes how the stresses lead to forces. Constitutive laws depend on the fluids in question and can be considered an educated guess: they therefore frequently break down for certain fluids and certain specific flow conditions.

In order to obtain the compressible Navier-Stokes equations, Stokes made several assumptions about fluid flows:

- The fluid is isotropic.
- Following insights from Newton, the shear stress depends linearly on the strain rate, $\tau = \mu\frac{\partial v}{\partial y}$, where μ is the dynamic viscosity, v is the velocity of the fluid parallel to the direction the shear is applied, and y is the direction perpendicular to the shear stress.
- The divergence of the deviatoric stress tensor is zero for a motionless fluid i.e. there are no net forces in equilibrium.

These assumptions lead to a constitutive law for the deviatoric stress tensor $\boldsymbol{\tau}$ of the form:

$$\boldsymbol{\tau} = p\mathbf{I} + \mu(\nabla\mathbf{v} + (\nabla\mathbf{v})^{\mathrm{T}}) - \frac{2}{3}\mu(\nabla\cdot\mathbf{v})\mathbf{I} \tag{3.6}$$

where we have defined a pressure $p = (\lambda+\frac{2}{3}\mu)\nabla\cdot\mathbf{v}$ with bulk viscosity λ. Substituting this into the Cauchy momentum equation yields the compressible Navier-Stokes momentum equation:

$$\rho\left(\frac{\partial\mathbf{u}}{\partial t} + \mathbf{v}\cdot\nabla\mathbf{v}\right) = -\nabla p + \mu\nabla^2\mathbf{v} + \tfrac{1}{3}\,\mu\nabla(\nabla\cdot\mathbf{v}) + \mathbf{f}, \tag{3.7}$$

Note that we also usually require an equation of state and a conservation of energy equation in addition to the mass and momentum conservation equations developed above. This connects hydrodynamics with thermodynamics.

3.3.4 Incompressible Navier-Stokes Equations

If we now assume that the fluid is incompressible i.e. that its density is constant and that the viscosity μ is constant, then the bulk viscosity vanishes $\lambda = 0$ and the mass continuity equation (Equation (3.3)) simplifies to $\nabla \cdot \mathbf{v} = 0$.

Making these approximations to the compressible Navier-Stokes equation (Equation (3.7)) yields the incompressible Navier-Stokes equation:

$$\rho \left(\frac{\partial \mathbf{v}}{\partial t} + \mathbf{v} \cdot \nabla \mathbf{v} \right) = -\nabla p + \mu \nabla^2 v + \mathbf{f} \tag{3.8}$$

If we scale by a reference density ρ_0 (since the density is constant) we obtain:

$$\frac{\partial \mathbf{v}}{\partial t} + \mathbf{v} \cdot \nabla \mathbf{v} = -\nabla w + \nu \nabla^2 \mathbf{v} + \mathbf{a} \tag{3.9}$$

where $w = \frac{p}{\rho_0}$ is the specific thermodynamic work per unit mass, $\nu = \frac{\mu}{\rho_0}$ is the kinematic viscosity, and $\mathbf{a}$ is an acceleration.

It is useful to discuss the qualitative meaning of each term of the incompressible Navier-Stokes equation:

$$\overbrace{\frac{\partial \mathbf{v}}{\partial t}}^{\text{Inertia}} + \underbrace{\mathbf{v} \cdot \nabla \mathbf{v}}_{\text{Convection}} \overbrace{- \underbrace{\nu \nabla^2 \mathbf{v}}_{\text{Diffusion}} = \underbrace{-\nabla w}_{\substack{\text{Internal} \\ \text{Sources}}}}^{\text{Stress Divergence}} + \underbrace{\mathbf{a}.}_{\substack{\text{External} \\ \text{Sources}}} \tag{3.10}$$

- The inertia terms tells us how much a fluid's previous velocity affects its current velocity. For example, if a swimmer stops propelling itself, it will continue to travel

through the fluid due to inertia, unless we are in the low Reynolds' number regime (discussed shortly).

- The convection term is a non—linear term that tells us how the fluid accelerates at different points in the flow, independent of time. An example is a squeezed hose-pipe — the fluid velocity increases near the point of constriction even when the flow is in equilibrium.
- Since the Laplacian of velocity tells us the difference between the velocity of the fluid at a point and the velocities of the fluid surrounding that point, we can interpret the kinematic viscosity ν as a parameter that controls the diffusion of momentum.

3.3.5 Stokes' Equations

In the context of this thesis and the modelling of emulsions in general, it is useful to discuss the conditions that lead to Stokes flow. If we scale the dimensional form of the incompressible Navier-Stokes momentum equation (Equation (3.8)) we obtain:

$$\frac{\partial \mathbf{v}}{\partial t} + \mathbf{v} \cdot \nabla \mathbf{v} = -\nabla p + \frac{1}{Re} \nabla^2 v + \mathbf{f}. \tag{3.11}$$

where

$$Re = \frac{\rho L V}{\mu} = \frac{L V}{\nu} \tag{3.12}$$

is the Reynolds' number. L is the characteristic length, and V is the average velocity (with respect to the fluid). The Reynolds' number quantifies the balance between inertial forces and viscous forces and is small if the relative velocity or the size of the object in question is small.

For small Reynolds' numbers, the viscous terms in the dimensionless Navier-Stokes Equation (Equation (3.11)) dominate and we can neglect the inertia terms, giving:

$$\nabla^2 \mathbf{v} - \nabla p + \mathbf{f} = 0 \tag{3.13}$$

$$\nabla \cdot \mathbf{v} = 0. \tag{3.14}$$

Soft matter is often interesting at the micrometre scale, which dictates that the Reynolds' number is small [107]. Several interesting scenarios occur in Stokes flow, namely the concept of time reversibility and its implications for low Reynolds' swimmers [108].

3.4 The Lattice Boltzmann Equation

The lattice Boltzmann equations stems from the Boltzmann equation [109–111], and so it is useful to describe the basic principles behind the Boltzmann equation first. The main idea of the Boltzmann equation is to consider the behaviour of collections of particles by introducing a probability distribution and considering the evolution of the probability distributions: what percentage of the particles at a certain location at a given time have velocities in a particular range? The probability of finding a particle in region $\mathbf{x} + d\mathbf{x}$ with momentum $\mathbf{p} + d\mathbf{p}$ is $f(\mathbf{x}, \mathbf{p}, t)\, d\mathbf{x}\, d\mathbf{p}$.

If we assume that the particles do not collide, and that the particles are uninfluenced by any external forces, the particles will continue along their trajectories and we can compute the distribution at $t + dt$ easily: $f(\mathbf{x} + \mathbf{c}\, dt, \mathbf{p} + d\mathbf{p}, t + dt)\, d\mathbf{x}\, d\mathbf{p} = f(\mathbf{x}, \mathbf{p}, t)\, d\mathbf{x}\, d\mathbf{p}$, where $\mathbf{c} = \mathbf{x}/\Delta t$ is the distribution function velocity.

However, if the particles collide, some particles will be collided into the phase-space volume and some will be collided out of it. Assuming that the velocities of particle collisions are uncorrelated [112], we can write this difference between the two distributions as $f(\mathbf{x} + \mathbf{p}\, dt, \mathbf{p} + \mathbf{F}\, dt, t + dt) - f(\mathbf{x}, \mathbf{p}, t) = \Omega\, dt$ where Ω is the rate of particle collisions, known as the Boltzmann collision factor.

If we Taylor expand to first order, we obtain Boltzmann's equation:

$$\mathbf{p} \cdot \nabla_x f(\mathbf{x}, \mathbf{p}, t) + \mathbf{F} \cdot \nabla_p f(\mathbf{x}, \mathbf{p}, t) + \partial_t f(\mathbf{x}, \mathbf{p}, t) = \Omega \tag{3.15}$$

To reach the lattice Boltzmann equation from the Boltzmann equation, we simply set $m = 1$ so that $\mathbf{p} = \mathbf{c}$ and discretise Equation (3.15) in space and time. Notice that in order to fully discretise Equation (3.15) we must also discretise the velocity space i.e. the distribution functions $f(\mathbf{x}, \mathbf{c}, t)$ are only allowed to have certain velocities.

This discretisation of the velocity space is one of the main differences between lattice Boltzmann methods and other numerical methods. The decision of how to discretise the velocity space is an important feature of lattice Boltzmann methods and significantly affects the resulting physics, which we discuss in more detail shortly.

If we now define $f(\mathbf{x}, \mathbf{c}_i, t)$ as $f_i(\mathbf{x}, t)$ and linearise the collision operator $\Omega\, dt \mapsto \Omega_i(\mathbf{x}, t)$ [113, 114], where $\Omega_i(\mathbf{x}, t)$ denotes the number of particles colliding into or out of the direction of $\mathbf{c}_i$ at position $\mathbf{x}$ and time t, we arrive at the lattice Boltzmann equation:

$$f_i(\mathbf{x} + \mathbf{c}_i \Delta t, t + \Delta t) - f_i(\mathbf{x}, t) = \Omega_i(\mathbf{x}, t). \tag{3.16}$$

In lattice Boltzmann modelling, we commonly define the time-step to be $\Delta t = 1$ and we normalise the velocities such that $\|\mathbf{c}_i\| = 1$, yielding:

$$f_i(\mathbf{x} + \mathbf{c}_i, t + 1) - f_i(\mathbf{x}, t) = \Omega_i(\mathbf{x}, t). \tag{3.17}$$

To reiterate, $f_i(\mathbf{x}, t)$ represents the single particle distribution function with velocity $\mathbf{c}_i$ at lattice coordinate $\mathbf{x}$ and time t.

3.4.1 The BGK Operator

In order for the lattice Boltzmann equation (Equation (3.17)) to be useful, we must define a collision operator that captures the relevant physics. A common choice for the collision operator is the BGK operator [115–117]:

$$\Omega_i = -\frac{1}{\tau}\left(f_i - f_i^{(\mathrm{eq})}\right) \tag{3.18}$$

where τ is a free parameter known as the relaxation time that controls how quickly the distribution f_i relaxes to the equilibrium distribution, $f_i^{(\mathrm{eq})}$. Sub-relaxation occurs for $\tau > 1$: the particle distribution only partially relaxes to equilibrium; over-relaxation occurs for $\tau < 1$: the particle distribution moves beyond equilibrium; and complete relaxation occurs for $\tau = 1$: only the equilibrium distributions propagate. The relaxation time τ cannot be arbitrarily small since linear numerical instabilities occur at $\tau = 0.5$ in the BGK model [117].

The collision operator must conserve mass

$$\begin{aligned} \sum_i \Omega_i &= -\frac{1}{\tau}\left(\sum_i f_i - \sum_i f_i^{(\mathrm{eq})}\right) = 0 \\ \implies \rho &= \sum_i f_i = \sum_i f_i^{(\mathrm{eq})} \end{aligned} \tag{3.19}$$

and momentum

$$\begin{aligned} \sum_i \mathbf{c}_i \Omega_i &= -\frac{1}{\tau}\left(\sum_i \mathbf{c}_i f_i - \sum_i \mathbf{c}_i f_i^{(\mathrm{eq})}\right) = 0 \\ \implies \rho\mathbf{u} &= \sum_i \mathbf{c}_i f_i = \sum_i \mathbf{c}_i f_i^{(\mathrm{eq})}. \end{aligned} \tag{3.20}$$

These relations are used to calculate the density ρ and momentum $\rho\mathbf{u}$ using the lattice Boltzmann method.

3.4.2 Lattice Boltzmann BGK Model

Using the BGK operator with the lattice Boltzmann equation, we obtain the full lattice BGK equation [117]:

$$f_i(\mathbf{x}+\mathbf{c}_i, t+1) - f_i(\mathbf{x}, t) = -\frac{1}{\tau}\left(f_i - f_i^{(0)}\right) \tag{3.21}$$

The computational implementation of this model involves a few conceptually simple steps:

1. A collision step coming from the right-hand side of Equation (3.21), involving:
   - The calculation of density, velocity, and other macroscopic quantities.
   - The calculation of the equilibrium distribution function f^{eq} (described in Section 3.5).
2. A streaming step stemming from the left-hand side of Equation (3.21).

3.5 From lattice Boltzmann to Navier-Stokes

Recovering the Navier-Stokes equations (Equation (3.7)) from the lattice Boltzmann equations (Equation (3.16)) requires some mathematical manipulation. Firstly, we Taylor expand the lattice Boltzmann BGK equation to second order:

$$\left(\partial_t + \nabla\cdot\mathbf{c}_i\right) f_i + \frac{1}{2}\left(\partial_t^2 + 2\partial_t\nabla\cdot\mathbf{c}_i + \nabla^2\mathbf{c}_i\right) f_i = -\frac{1}{\tau}\left(f_i - f_i^{(\text{eq})}\right) \tag{3.22}$$

Next, we carry out a so-called multiscale Chapman-Enskog expansion [118–121] in which we separate the time-scales into t_1 for advection and t_2 for diffusion by making the following approximations [122, 123]:

$$\partial_t = \epsilon\partial_t + \epsilon^2\partial_{t2} \tag{3.23}$$

$$\nabla = \epsilon\nabla \tag{3.24}$$

$$f_i = f_i^{(\text{eq})} + \epsilon f_i^{(1)} + \epsilon f_i^{(2)} \tag{3.25}$$

$$\Omega_i = \Omega_i^{(0)} + \epsilon\Omega_i^{(1)} + \epsilon^2\Omega_i^{(2)} \tag{3.26}$$

Substituting these expansions into Equation (3.22) and collecting terms of the same order, to order e^0 we obtain:

$$\frac{\partial f_i^{\text{eq}}}{\partial t_1} + \mathbf{c}_i + \nabla_1 f^{\text{eq}} = -\frac{f_i^{(1)}}{\tau} \tag{3.27}$$

Using Equation (3.19) and Equation (3.20) we can see that this equation is exactly the mass continuity equation (Equation (3.3)). Similarly, to order ϵ^1:

$$\frac{\partial \rho \mathbf{v}}{\partial t} + \nabla \cdot \Pi = 0 \tag{3.28}$$

where the momentum flux tensor is

$$\Pi_{\alpha\beta} = \sum_i (\mathbf{c}_i)_\alpha (\mathbf{c}_i)_\beta \left(f_i^{\text{eq}} + \left(1 - \frac{1}{2\tau}\right) f_i^{(1)} \right)$$

which looks similar to the momentum conservation equation in Equation (3.4). In order to make further progress, we need to specify the lattice vectors $\mathbf{c}_i$ and the equilibrium distribution function f^{eq}.

In this thesis, we use the D3Q19 lattice (Figure 3.1), which is the most common lattice choice in 3 dimensions. The choice of lattice is vitally important in lattice Boltzmann modelling because only certain lattices with sufficient isotropy recover the Navier-Stokes equations [124–126]. The D3Q19 lattice vectors are given by:

$$\mathbf{c}_i = \begin{cases} (0,0,0) & i = 0 \\ (\pm 1,0,0), (0,\pm 1,0), (0,0,\pm 1) & i = 1,2,\ldots,6 \\ (\pm 1,\pm 1,\pm 1) & i = 7,8,\ldots,18 \end{cases} \tag{3.29}$$

The equilibrium distribution function we use comes from a Hermite quadrature of the Maxwell distribution function:

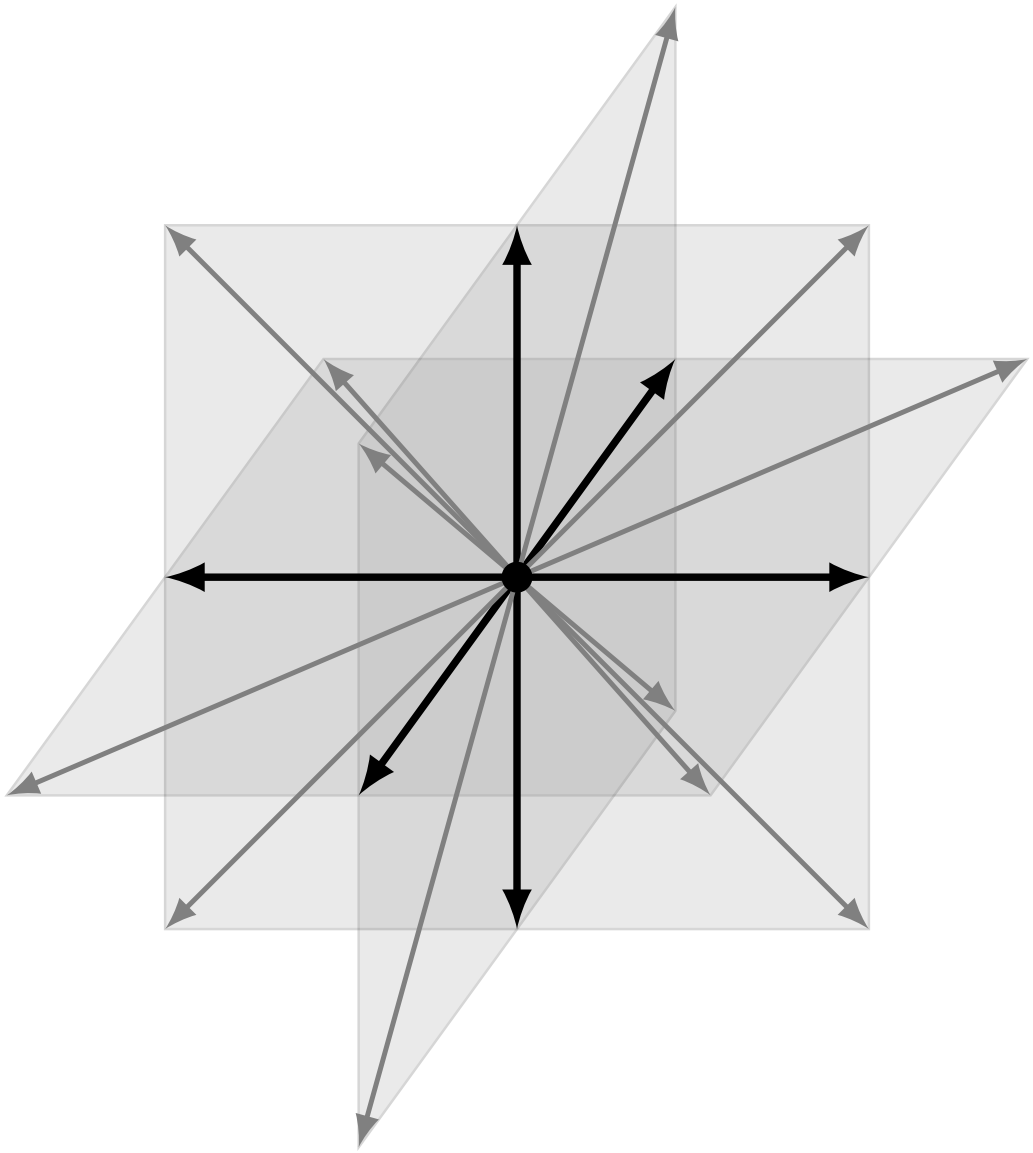

FIGURE 3.1: The D3Q19 lattice, showing the velocity vectors from the central lattice node, at which the zero vector resides. Each velocity vector lies in one of the three planes shown. Tikz code courtesy of Dr. Timm Krüger.

$$f_i^{\mathrm{eq}} = w_i \rho^c \left(1 + \frac{\mathbf{c}_i \cdot \mathbf{v}}{c_s^2} + \frac{(\mathbf{c}_i \cdot \mathbf{v})^2}{2c_s^4}\right) \tag{3.30}$$

where w_i are the lattice vector weightings given by

$$w_i = \begin{cases} 0 & i = 0,\ \text{zero velocity vector} \\ \frac{1}{18} & i = 1, 2, \ldots, 6,\ \text{nearest} - \text{neighbours} \\ \frac{1}{36} & i = 7, 8, \ldots, 18,\ \text{next} - \text{nearest neighbours} \end{cases} \tag{3.31}$$

This expansion is valid only for small Mach numbers, $\text{Ma} = \frac{v}{c_s}$, where the lattice speed of sound c_s is a constant, which follows from the D3Q19 lattice choice:

$$c_s = \frac{1}{\sqrt{3}} \frac{\Delta x}{\Delta t} = \frac{1}{\sqrt{3}} \tag{3.32}$$

using our choice of lattice units $\Delta x = \Delta t = 1$. Inserting the equilibrium distribution function and lattice vectors into our momentum flux tensor yields:

$$\begin{aligned} \Pi^{(0)}_{\alpha\beta} &= \sum_i (\mathbf{c}_i)_\alpha (\mathbf{c}_i)_\beta f_i^{\text{eq}} = p\Delta_{\alpha\beta} + \rho \mathbf{v}_\alpha \mathbf{v}_\beta \\ \Pi^{(1)}_{\alpha\beta} &= \left(1 - \frac{1}{2\tau}\right) \sum_i (\mathbf{c}_i)_\alpha (\mathbf{c}_i)_\beta f_i^{(1)} = \nu \left(\nabla_\alpha(\rho \mathbf{v}_\beta) + \nabla_\beta(\rho \mathbf{v}_\alpha)\right) \end{aligned} \tag{3.33}$$

with pressure $p = \frac{\rho}{c_s^2} = \frac{\rho}{3}$ giving a kinematic viscosity:

$$\nu = c_s^2 \Delta t \left(\frac{\tau}{\Delta t} - \frac{1}{2}\right) = \frac{2\tau - 1}{6}. \tag{3.34}$$

Using these relations, it is clear that the lattice Boltzmann momentum equation (Equation (3.28)) is equivalent to the compressible Navier-Stokes equation (Equation (3.7)) provided the density variations are small.

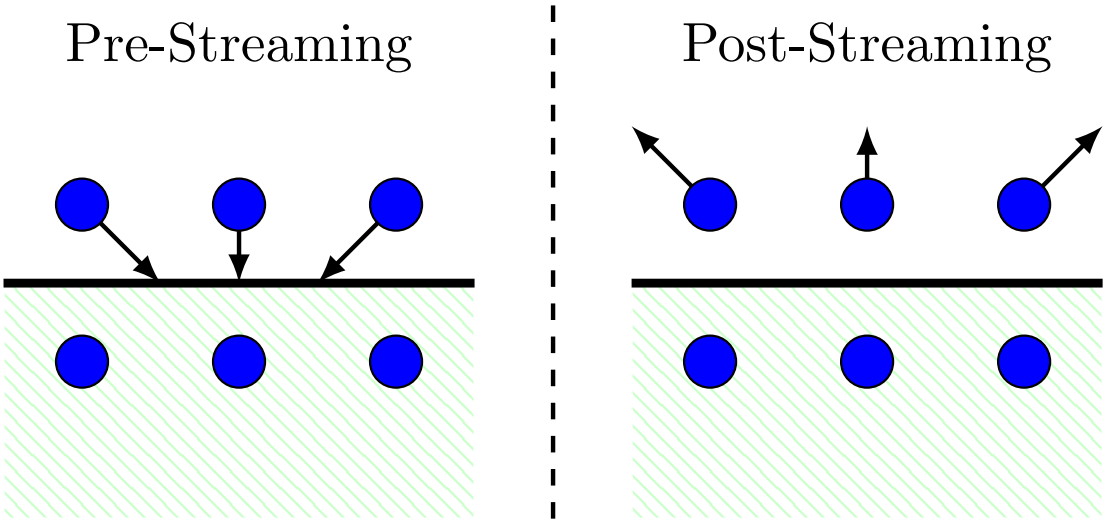

FIGURE 3.2: Bounce-back boundary conditions with a solid wall: particle distribution functions that would stream into the solid node get reflected back along the direction they came from.

3.6 Simple Bounce-Back Boundary Conditions

One of the biggest advantages of lattice Boltzmann methods for modelling fluid flows is the simple implementation of complex solid boundary geometries. Lattice Boltzmann achieves this by using a simple bounce back boundary condition on solid nodes in which the distribution functions reflect back to the lattice sites they came from, as shown in Figure 3.2 [127, 128]. The solid nodes do not participate in the regular lattice Boltzmann stream-collide step (Equation (3.21)).

3.7 Multiple Fluids and the Shan-Chen Model

In order to simulate multiple fluids, we add a phenomenological fluid-fluid interaction between each fluid species, the so-called Shan-Chen force [129, 130]:

$$\mathbf{F}_C^c(\mathbf{x},t) = -\Psi^c(\rho^c(\mathbf{x},t)) \sum_{c,c'} g_{cc'} \sum_{\mathbf{x}} \Psi^{c'}(\rho^c(\mathbf{x}',t))(\mathbf{x}'-\mathbf{x}). \tag{3.35}$$

where $c \neq c'$ denote the fluid components, $g_{cc'}$ is a coupling strength between the fluid components. The sign of $g_{cc'}$ determines whether the fluids exhibit repulsion (positive $g_{cc'}$) or attraction (negative $g_{cc'}$). Ψ^c is a pseudo-potential, a function of the density

$\rho^c(\mathbf{x}, t)$ of the respective fluid component at an individual lattice site, which plays the role of an "effective mass". The essence of the Shan-Chen force is to calculate the effective mass from the fluid density at a particular lattice-site, and multiply this with the effective mass of the other fluid component at neighbouring lattice sites, with the degree of attraction or repulsion chosen by the coupling constant. The Shan-Chen model can be used to simulate multi-phase and/or multi-component fluids depending on the density difference of the two fluids: a large density difference corresponds to the simulation of multi-phase fluids, and a small fluid density difference corresponds to the simulation of multi-component fluids.

When modelling multicomponent fluids, the individual fluid components obey the usual lattice Boltzmann equation:

$$f_i^c(\mathbf{x} + \Delta t \mathbf{c}_i, t + \Delta t) = f_i^c(\mathbf{x}, t) + \Omega_i^c(\mathbf{x}, t) \tag{3.36}$$

where c is the fluid component (for a binary system, $c = r, b$) and $i = 1, \ldots, N$ so that $f_i^c(\mathbf{x}, t)$ represents the particle distribution function for component c in direction $\mathbf{c}_i$ at lattice coordinate $\mathbf{x}$ and time t.

The Shan-Chen model correctly reproduces several vital properties of non-ideal fluids, such as a non-ideal bulk equation of state and a non-zero surface tension [130, 131]. There are many different possible choices of the effective mass Ψ, and it is possible to modify the equation of state based on the choice of Ψ [132]. Certain choices allow larger fluid density differences, but the ubiquitous choice in the research literature and the one that we choose is

$$\Psi(\rho^c(\mathbf{x}, t)) = 1 - e^{-\rho^c(\mathbf{x}, t)}. \tag{3.37}$$

When the potential is of the form in Equation (3.37), the force between the fluid components decreases exponentially as the fluid density increases, which is vital for numerical stability. Unfortunately, this choice of Ψ means that the coexistence curve deviates from thermodynamic theory, though recent work has aimed to introduce a

thermodynamically-consistent temperature into the Shan-Chen model by changing the form of Ψ and considering next-to-nearest neighbour interactions [133]. Other limitations include the fact that the surface tension and the equation of state are both dependent on $g_{cc'}$, which does not allow us to change them independently.

To incorporate the Shan-Chen force into the lattice Boltzmann equation (Equation (3.16)) we add a shift to the velocity $\mathbf{u}^c(\mathbf{x},t) \mapsto \mathbf{u}^c(\mathbf{x},t) + \Delta\mathbf{u}^c(\mathbf{x},t)$ in the local equilibrium distribution function only

$$\Delta\mathbf{u}^c(\mathbf{x},t) = \frac{\tau^c \mathbf{F}_C^c(\mathbf{x},t)}{\rho^c(\mathbf{x},t)} \tag{3.38}$$

The velocity of each fluid component is

$$\mathbf{u}^c(\mathbf{x},t) \equiv \frac{\sum_i \mathbf{c}_i f_i^c(\mathbf{x},t) - \frac{1}{2}\Delta t \mathbf{F}_C^c(\mathbf{x},t)}{\sum_i f_i^c(\mathbf{x},t)}. \tag{3.39}$$

In this thesis, we simulate two fluids, referred to as the red fluid and blue fluid, which can be considered analogous to oil and water. We define an order parameter $\phi(\mathbf{x},t) = \rho^r(\mathbf{x},t) - \rho^b(\mathbf{x},t)$ which we call the "colour" of a lattice site. The colour order parameter is used, amongst other things, to determine the position of the fluid-fluid interface.

3.7.1 Colloidal Particles

To simulate rigid, finite-sized particles suspended in a fluid [4, 134–136] we use the method introduced by Ladd [137, 138] and Aidun et al. [139], where particles are discretised on the lattice [140]. The trajectory of the particles is calculated by solving the particles' classical equations of motion $\mathbf{F} = m \cdot \frac{d\mathbf{u}_\mathrm{p}}{dt}$ and $\mathbf{D}(t) = I \cdot \frac{d\omega}{dt}$ using a leapfrog integrator according to Equation (3.2) as described in Section 3.2.

To include particle-fluid interactions, lattice sites occupied by a particle are treated as solid wall nodes with simple bounce-back boundary conditions, as described in Section 3.6.

The interaction between the particles and the fluid is controlled by a modified lattice Boltzmann equation so that whenever a lattice site $\mathbf{x}$ is inside a particle the following equation replaces the usual lattice Boltzmann equation (Equation (3.36)):

$$f_i^c(\mathbf{x} + \Delta t\mathbf{c}_i, t + \Delta t) = f_{\bar{i}}^c(\mathbf{x} + \mathbf{c}_i, t) + \Omega_{\bar{i}}^c(\mathbf{x} + \mathbf{c}_i, t) + C \tag{3.40}$$

where C depends linearly on the velocity of the particle surface and $\bar{i}$ is defined such that $\mathbf{c}_i = -\mathbf{c}_{\bar{i}}$.

This results in a no-slip boundary condition half-way between the fluid and the solid node. Due to the particle bounce-back conditions and the change of fluid momentum that is reflected at the boundary, an additional force and torque act on the particle

$$\mathbf{F}(t) = (2f_{\bar{i}}^c(\mathbf{x} + \mathbf{c}_i, t) + C)\mathbf{c}_{\bar{i}} \tag{3.41}$$

$$\mathbf{D}(t) = \mathbf{F}(t) \times \mathbf{r}(t) \tag{3.42}$$

respectively, where $\mathbf{r}(t)$ is a vector directed from the particle centre to the lattice site of reflection.

As the particle moves across the lattice, the particle invades new lattice sites and vacates others. During invasion, the fluid at the invaded site is removed and its momentum transfers to the particle:

$$\mathbf{F}(t) = -\sum_c \rho^c(\mathbf{x}, t)\mathbf{u}^c(\mathbf{x}, t). \tag{3.43}$$

Vacated lattice sites require more care. For a single fluid, when the particle vacates a lattice site we fill the lattice site with the initial fluid density, ρ_{init}. For two fluids, we define an average density

$$\bar{\rho}^c(\mathbf{x},t) \equiv \frac{1}{N_{FN}} \sum_{i_{FN}} \rho^c(\mathbf{x} + \mathbf{c}_{i_{FN},t}) \tag{3.44}$$

averaged by N_{FN} neighbouring fluid lattice sites with coordinates $\mathbf{x}_{i_{FN}} = \mathbf{x} + \mathbf{c}_{i_{FN}}$. The vacated fluid site is then filled with a fluid density according to:

$$f_i^c(\mathbf{x},t) = \rho_{new}^c(\mathbf{x},t) \cdot f_i^{eq}(\mathbf{u}_{surface}(\mathbf{x},t), \rho_{new}(\mathbf{x},t)) \tag{3.45}$$

where $\mathbf{u}_{surface}(\mathbf{x},t)$ is the velocity of the lattice nodes in the vicinity of the particle surface and $\rho_{new}^c(\mathbf{x},t)$ is the initial fluid velocity. This leads to another force on the particle, $\mathbf{F}(t) = \sum_c \rho_{new}^c \mathbf{u}_{\text{surf}}(\mathbf{x},t)$ in order to conserve momentum.

When calculating the Shan-Chen forces between different fluids according to Equation (3.35), empty lattice sites inside a particle are still taken into consideration. However, no Shan-Chen forces act from the particle to the fluid, and hence a layer of increased fluid density forms around the particle. To suppress this effect, the outermost layer of lattice sites inside the particle is filled with a virtual fluid density that is an average of the surrounding fluid densities, $\rho^c(\mathbf{x},t) = \bar{\rho}^c(\mathbf{x},t)$. This virtual fluid is static: the lattice Boltzmann equation, advection and collision, is not applied to the virtual fluid.

The Shan-Chen forces acting on the particle from the surrounding fluid $\sum_{\mathbf{x}} \sum_c \mathbf{F}^c(\mathbf{x},t)$ are added to the other forces used to calculate the particle trajectories. Due to these Shan-Chen forces between the particle and the fluid, the fluid density near the particle surface is generally smaller than the bulk density, which can lead to mass loss over time when choosing $\rho^c(\mathbf{x},t) = \bar{\rho}^c(\mathbf{x},t)$. We apply a correction term that suppresses the mass loss over-long time scales with only small deviations on shorter time-scales

$$\rho_{new}^c(\mathbf{x},t) = \bar{\rho}^c(\mathbf{x},t) \left(1 - C_0 \frac{\sum_c \rho_{init}^c \delta\rho^c(t)}{\rho_{init}^c V_{box}}\right) \tag{3.46}$$

where $\delta\rho^c(t)$ is the mass error of component c at time t and $C_0 = 2500$ is a parameter which controls the correction strength.

The addition of the virtual fluid allows us to control the contact angle and therefore the wettability of the particles [4, 135]. We define $\Delta\rho$ are the particle colour, which is an input parameter. A positive value is added to the red fluid component and a negative value is added to the blue fluid component as follows

$$\rho^r_{virt} = \bar{\rho}^r + \Delta\rho \tag{3.47}$$

$$\rho^b_{virt} = \bar{\rho}^b - \Delta\rho \tag{3.48}$$

so that $\Delta\rho = 0$ represents a neutrally wetting particle with contact-angle $\theta = 90°$. The relationship between the virtual fluid and the contact angle is approximately linear for spherical particles.

When two particles move towards each other a lubrication interaction results in a force acting to separate the particles. If there is less than one lattice site between the particles, the flow is unresolved and not properly reproduced. A lubrication correction is added:

$$\mathbf{F}_{ij} = \frac{3}{2}\pi\nu^c R^2 \hat{\mathbf{r}}_{ij} \left(\hat{\mathbf{r}}_{ij}(\mathbf{u}_1 - \mathbf{u}_2)\right) \left(\frac{1}{|\hat{\mathbf{r}}_{ij}| - 2R} - \frac{1}{\Delta_c}\right) \tag{3.49}$$

where $\hat{\mathbf{r}}_{ij}$ is the displacement vector between the particles and $\mathbf{u}_1$ and $\mathbf{u}_2$ are their respective velocities. The lubrication correction is applied for distances $0.1 < |\mathbf{r}| < \frac{2}{3}$ with the lower bound due to the divergence of Equation (3.49) when the particles touch.

For ellipsoidal particles, we use an approach developed by Berne and Pechukas [141]. We define two parameters $\sigma = 2R$ and $\epsilon = \frac{3\pi\mu}{8}\sigma$ such that:

$$\epsilon(\hat{\mathbf{o}}_i, \hat{\mathbf{o}}_j) = \frac{\bar{\epsilon}}{\sqrt{1 - \Gamma^2(\hat{\mathbf{o}}_i\hat{\mathbf{o}}_j)^2}} \tag{3.50}$$

and

$$\sigma(\hat{\mathbf{o}}_i, \hat{\mathbf{o}}_j, \hat{\mathbf{r}}_{ij}) = \frac{\bar{\sigma}}{\sqrt{1 - \frac{\Gamma}{2}\left(\frac{(\hat{\mathbf{r}}_{ij}\hat{\mathbf{o}}_i + \hat{\mathbf{r}}_{ij}\hat{\mathbf{o}}_j)^2}{1+\Gamma\hat{\mathbf{o}}_i\hat{\mathbf{o}}_j} + \frac{(\hat{\mathbf{r}}_{ij}\hat{\mathbf{o}}_i - \hat{\mathbf{r}}_{ij}\hat{\mathbf{o}}_j)^2}{1-\Gamma\hat{\mathbf{o}}_i\hat{\mathbf{o}}_j}\right)}} \tag{3.51}$$

where $\bar{\sigma} = 2R_\perp$, $\bar{\epsilon} = \frac{3\pi\mu}{8}\bar{\sigma}$, $\Gamma = \frac{R_\parallel^2 - R_\perp^2}{R_\parallel^2 + R_\perp^2}$ and $\hat{\mathbf{o}}_i$ is the unit orientation vector of particle i. $R_\parallel$ and $R_\perp$ are the radii parallel and perpendicular to the particle symmetry axis respectively.

The lubrication force for anisotropic particles can the be written as

$$\mathbf{F}_{ij}(\hat{\mathbf{o}}_i, \hat{\mathbf{o}}_j, \hat{\mathbf{r}}_{ij}) = \epsilon(\hat{\mathbf{o}}_i, \hat{\mathbf{o}}_j)\tilde{\mathbf{F}}_{ij}\left(\frac{r_{ij}}{\sigma(\hat{\mathbf{o}}_i, \hat{\mathbf{o}}_j, \hat{\mathbf{r}}_{ij})}\right) \tag{3.52}$$

where $\tilde{\mathbf{F}}_{ij} = \hat{\mathbf{r}}_{ij}(\hat{\mathbf{r}}_{ij}(\mathbf{u}_1 - \mathbf{u}_2))\left(\frac{1}{|\hat{\mathbf{r}}_{ij}|-1} - \frac{\sigma}{\Delta_c}\right)$ is a generic dimensionless function taking the specific form of the force into account.

To avoid particle overlap, we apply a short-ranged repulsive Hertz potential between the particles. For spherical particles, the inter-particle potential is the Hertz potential $\phi_H = K_H(2r_p - r_{ij})^{\frac{5}{2}}$ for $r_{ij} \leq 2r_p$ and $\phi_H = 0$ for $r_{ij} > 2r_p$ where r_{ij} is the distance between two particles with coordinates $\mathbf{r}_i$ and $\mathbf{r}_j$ and $K_H = 100$ is the strength of the interaction. For ellipsoidal particles, the above potential needs to be modified. Defining $\sigma = 2R$ and $\epsilon = K_H\sigma^{\frac{5}{2}}$ we obtain:

$$\phi_H(\hat{\mathbf{o}}_i, \hat{\mathbf{o}}_j, \hat{\mathbf{r}}_{ij}) = \epsilon(\hat{\mathbf{o}}_i, \hat{\mathbf{o}}_j)\tilde{\phi}_H\left(\frac{r_{ij}}{\sigma(\hat{\mathbf{o}}_i, \hat{\mathbf{o}}_j, \hat{\mathbf{r}}_{ij})}\right) \tag{3.53}$$

where again $\tilde{\phi}_H = (1-x)^{\frac{5}{2}}$ is a generic dimensionless function which takes the specific form of the potential into account.

3.8 Lattice Boltzmann Simulations of Particle-Stabilised Emulsions

We briefly describe some of the studies carried out using lattice Boltzmann simulations of binary fluids with immersed rigid particles. The focus here is to highlight the capability of the method and types of studies carried out, rather than their findings.

Stratford et al. [142] were the first to combine standard lattice Boltzmann algorithms for binary fluids [143–145] with immersed rigid particles [137, 146], which they then used to predict the existence of bijels [65] (described in Chapter 1). Kim et al. [147] used the same algorithm to investigate the formation of bijels when the two fluids have different volume ratios. Later, Kim et al. [148] added magnetic particle-particle interactions to investigate the behaviour of bijels composed of magnetic particles and ferrofluids in general [149].

Jansen and Harting [4] later made use of the Shan-Chen method described in detail in this Chapter for simulating multiple fluids, which is a somewhat simpler implementation than that developed by Stratford et al. [142].

Frijters et al. [134] used this algorithm to compare the behaviour of particle-stabilised droplets with surfactant-stabilised droplets in steady shear flow. They found that particles migrate to areas of high droplet curvature with lower shear velocities. Additionally, they found that adsorbed particles make droplets break up more easily under shear flow. This finding is consistent with particles acting as emulsifiers i.e. aiding the formation of emulsion droplets.

Günther et al. [136] compared the time-scales of emulsion formation for spherical and ellipsoidal particles. They found that, in contrast with spherical particles, spheroidal particles never quite reach a steady domain size (in the case of Bijels) or droplet size (in the case of Pickering emulsions). They attribute this effect to local reordering amongst the ellipsoidal particles due to capillary interactions.

Frijters et al. [150] investigated domain and droplet sizes in particle-stabilised emulsions, and confirmed the work of Arditty et al. [151] by finding that the average radius of particle-stabilised droplets, R_{avg}, decreases as the particle concentration ϕ increases according to an inverse law, $R_{\text{avg}} = \frac{1}{\phi}$.

Liang et al. [79], Shinto et al. [80] and Onishi et al. [81] studied capillary interactions between heavy spherical particles adsorbed at a fluid-fluid interface, recovering the pair interaction energy developed by Chan et al. [78] (Equation (2.18)).

These studies highlight the versatility of lattice Boltzmann method with immersed rigid particles in studying particle-stabilised emulsions. The model of Swift et al. [143] even allows one to substitute one or more fluid components with a liquid crystal, enabling the simulation of colloid-liquid crystal mixtures [152]. A particular advantage of the Shan-Chen model used in this paper is the tunable nature of the particle-fluid interactions, allowing the control of the particle contact angle [4].

3.9 Validation: The Drag Force on a Spherical Particle

In addition to the published works that have validated aspects of the algorithm described in this Chapter, [4, 134, 136, 150] and indeed the papers arising from this thesis, [1–3] which also carry out various validation tests, we performed a simple validation of the algorithm described in this Chapter.

Calculating the drag force on a spherical particle moving through a fluid in the Stokes' regime is amenable to a simple analytical calculation yielding the following drag force:

$$F_D = 6\pi\mu R v \tag{3.54}$$

where μ is the dynamic viscosity, R is the particle radius, and v is the particle velocity.

In order to simulate such a system, we fix the position of a particle in the centre of a $3D$ periodic system and apply a body force to the surrounding fluid. After a short time period, the system reaches a steady-state. Using Lattice Boltzmann methods, we calculate the drag force on the particle by simply summing up the single particle distribution functions that stream in and out of the particle surface according to bounce-back boundary conditions (Section 3.6). With periodic boundary conditions, a correction to the drag force known as the Hasimoto correction must be applied: [153, 154]

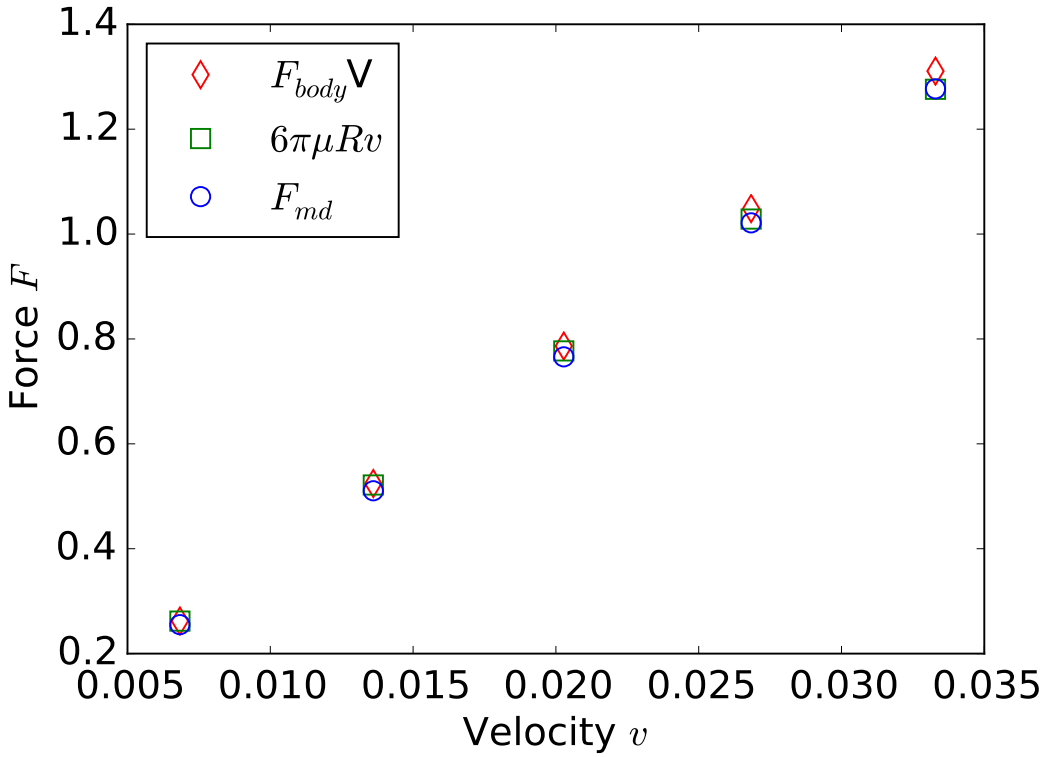

FIGURE 3.3: The measured drag force (blue symbols) on a fixed spherical particle in a periodic channel surrounded by fluid subjected to a body force F_{body} (red diamonds) and compared with the analytical solution for Stokes' flow (green squares). We observe good agreement between all three quantities, validating the correctness of our algorithm for typical system parameters used in this thesis.

$$F_H = \frac{6\pi\mu Rv}{1 - 2.83a + 4.19a^3 - 27.4a^7 + \mathcal{O}(a^9)} \tag{3.55}$$

where $a = R/L$ is the particle radius to system size ratio.

Figure 3.3 shows the comparison between the measured drag force on a spherical particle from our lattice Boltzmann simulations (blue circles) and the analytical drag force corresponding to Eq. (3.55) (green squares) for a particle with radius $R = 10$ lattice units, which is a characteristic particle size used throughout this thesis, and system size $L = 64$. The red triangles represent the body force applied to the fluid. Figure 3.3 shows good agreement between the analytically predicted drag force and the measured simulation drag force. The force applied to the fluid (red diamonds) is also equal to

the drag force, although small deviations emerge for large fluid velocities due to the departure from the low Reynolds' number regime. The success of this validation confirms that we can have confidence in correctness of the results of this thesis.

Chapter 4

How Much Energy Does it Take to Detach a Particle From a Fluid-Fluid Interface?

4.1 Introduction

A natural question arises from our discussion of Pickering emulsions and other particle stabilised emulsions: why do particles adsorb at fluid-fluid interfaces? The simple answer is that particles come into contact with a fluid-fluid interface mostly by chance, for example, due to Brownian motion from thermal fluctuations, or stirring and shearing of particle-fluid-fluid mixtures, but once they collide with an interface, they attach irreversibly; there is no force driving the particles towards the interface in the first place. The question then becomes: why do particles stick at interfaces? We can find the answer by considering a simple model of the free energy of a particle at an interface and in one of the bulk fluids. We calculate the free energy of a particle adsorbed at a fluid-fluid interface or immersed in the bulk fluid by considering the relevant surface energies and surface areas for a particular configuration and summing up the contributions (Figure 4.1).

The free energy of a particle adsorbed at an interface (Figure 4.1a) is [41]:

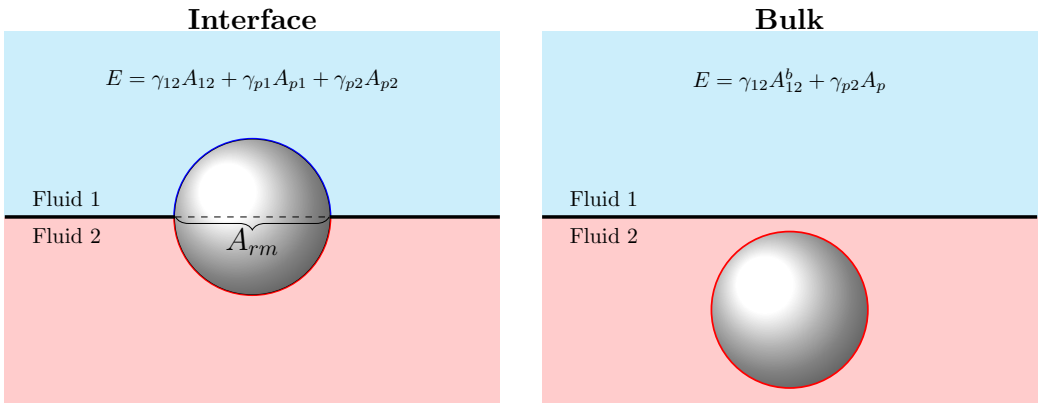

(A) A particle adsorbed at a fluid-fluid interface. The solid blue line denotes the area of the particle immersed in fluid 1, A_{p1}, the solid red line denotes the area of the particle immersed in fluid 2, A_{2p}, and the solid black line is the area of the fluid-fluid interface when the particle is adsorbed at the interface, A_{12}.

(B) A particle immersed in bulk fluid 2. The solid red line denotes the surface area of the particle immersed in fluid 2, which in this case is the total particle surface area, A_p. The solid black line is the surface-area of the fluid-fluid interface, A^b_{12}. Note that $A^b_{12} > A_{12}$.

FIGURE 4.1: A simple free energy model which takes into account the surface energies of the particle and fluid 1, γ_{p1}, the particle and fluid 2, γ_{p2}, and fluid 1 and fluid 2, γ_{12}. To obtain the energy in a particular configuration we sum the contributions of the surface energies with the relevant surface areas. In (A), A_{rm} is the area removed from the fluid-fluid interface by the presence of the particle, which is a crucial parameter in the detachment energy (Equation (4.3)).

$$E_{\text{int}} = \gamma_{12}A_{12} + \gamma_{p1}A_{p1} + \gamma_{p2}A_{p2} \tag{4.1}$$

and the free energy of a particle immersed in the bulk (Figure 4.1b) is

$$E_{\text{b}} = \gamma_{12}A^b_{12} + \gamma_{p2}A_p \tag{4.2}$$

where A_{ij} is the area of the i, j interface and γ_{ij} is the surface-energy of the i, j interface where $i, j = \{1\text{: fluid 1, 2: fluid 2, p: particle}\}$ and A_p is total particle surface area.

Taking the difference between these two configurations yields the detachment energy [41, 42]:

G. B. Davies et al. Detachment Energies of Spheroidal Particles from Fluid-Fluid Interfaces, *Journal of Chemical Physics*, 141, 154902 (2014) [1]. Reproduced with permission from [1].

$$\Delta E = E_{\mathrm{b}} - E_{\mathrm{int}} = \gamma_{12} A_{rm} + (\gamma_{p2} - \gamma_{p1}) A_{p1} \tag{4.3}$$

where $A_{rm} = A_{12}^{b} - A_{12}$ is the area removed from the fluid-fluid interface by the presence of a particle.

The detachment energy (Equation (4.3)) depends implicitly on the particle shape via the particle surface area. The crucial insight from the detachment energy in Equation 4.3 is that particles that remove more interface area have a higher detachment energy.

4.1.1 Spherical Particles

For a spherical particle, $A_p = 4\pi R^2 = A_{p1} + A_{p2}$, $A_{p1} = 2\pi R^2(1 + \cos\theta)$, and $A_{rm} = \pi(R\sin\theta)^2$, where R is the particle radius and θ is the particle contact angle (Figure 4.2), and the detachment energy becomes $\Delta E = \gamma_{12}\pi R^2(1+\cos\theta)^2$. We can obtain a similar expression for the detachment into bulk fluid 1, $\Delta E = \gamma_{12}\pi R^2(1-\cos\theta)^2$, and the two expressions can be combined into a single expression, the well known detachment energy for a single spherical particle from a fluid-fluid interface [41]:

$$\Delta E = \gamma_{12}\pi R^2(1 - |\cos\theta|)^2 \tag{4.4}$$

For some commonly realised experimental values e.g. neutrally wetting micron-sized spherical particles adsorbed at an interface with surface tension $\gamma_{12} = 50\,\mathrm{mN\,m^{-1}}$, $\Delta E \sim 10^7 k_B T$, and thermal fluctuations are unable to detach the particle from an interface.

4.1.2 The Phase Space of Young's Equation

The detachment energy expression in Equation (4.3) shows that a particle will remain attached at an interface even if the fluid-particle surface energies are higher than the fluid-fluid surface energy, provided the fluid-particle surface energies are equal, $\gamma_{1p} = \gamma_{2p}$, i.e. the particle is neutrally wetting.

The particle wants to minimise its free energy (Equation (4.1)) at an interface.

G. B. Davies et al. Detachment Energies of Spheroidal Particles from Fluid-Fluid Interfaces, *Journal of Chemical Physics*, 141, 154902 (2014) [1]. Reproduced with permission from [1]. Copyright 2014, AIP Publishing LLC.

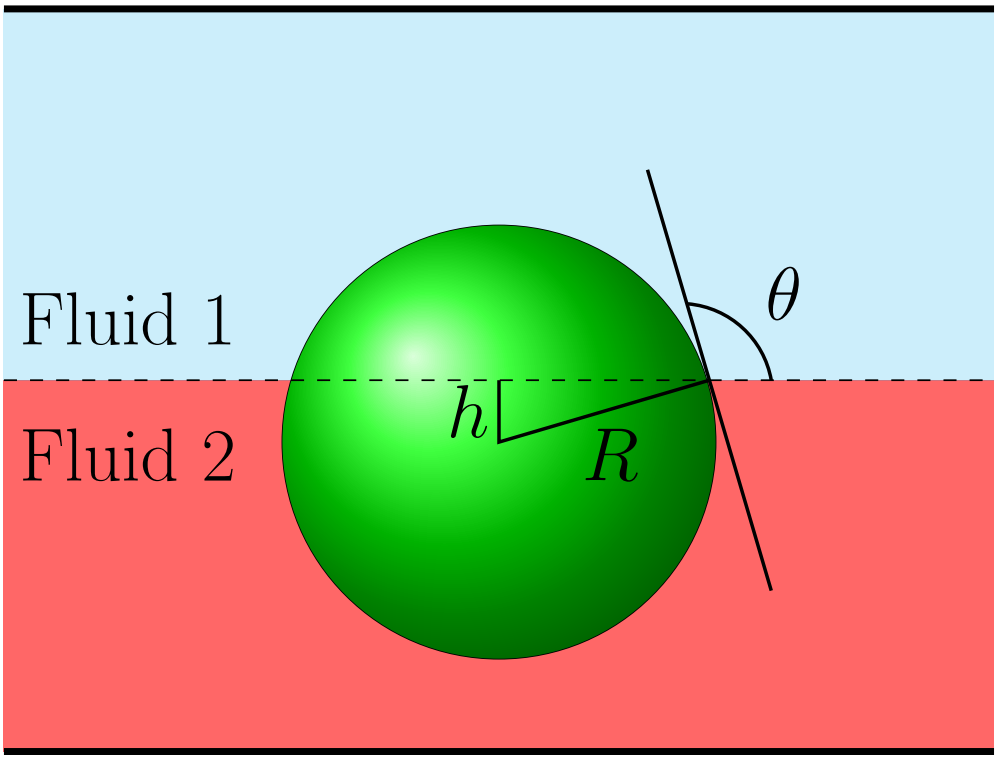

FIGURE 4.2: For a spherical particle, the contact angle θ is defined as the ratio of the height of the particle centre-of-mass, h, above the undeformed interface to the radius, R, of the particle.

$$dE_{\text{int}} = \gamma_{12}\, dA_{12} + \gamma_{p1}\, dA_{p1} + \gamma_{p2}\, dA_{p2} = 0 \tag{4.5}$$

Noting that $dA_{p2} = -\,dA_{p1}$ and defining an equilibrium contact angle θ (Figure 4.2) such that $dA_{12} = dA_{p1}\cos\theta$ we obtain:

$$dE_{\text{int}} = \gamma_{12}\, dA_{p1}\cos\theta + \gamma_{p1}\, dA_{p1} - \gamma_{p2}\, dA_{p1} = 0 \tag{4.6}$$

and solving $\frac{dE_{\text{int}}}{dA_{p2}} = 0$ yields Young's equation, which relates the contact angle of the particle to the balance of surface energies:

$$\frac{\gamma_{p2} - \gamma_{p1}}{\gamma_{12}} = \cos\theta \tag{4.7}$$

G. B. Davies et al. Detachment Energies of Spheroidal Particles from Fluid-Fluid Interfaces, *Journal of Chemical Physics*, 141, 154902 (2014) [1]. Reproduced with permission from [1]. Copyright 2014, AIP Publishing LLC.

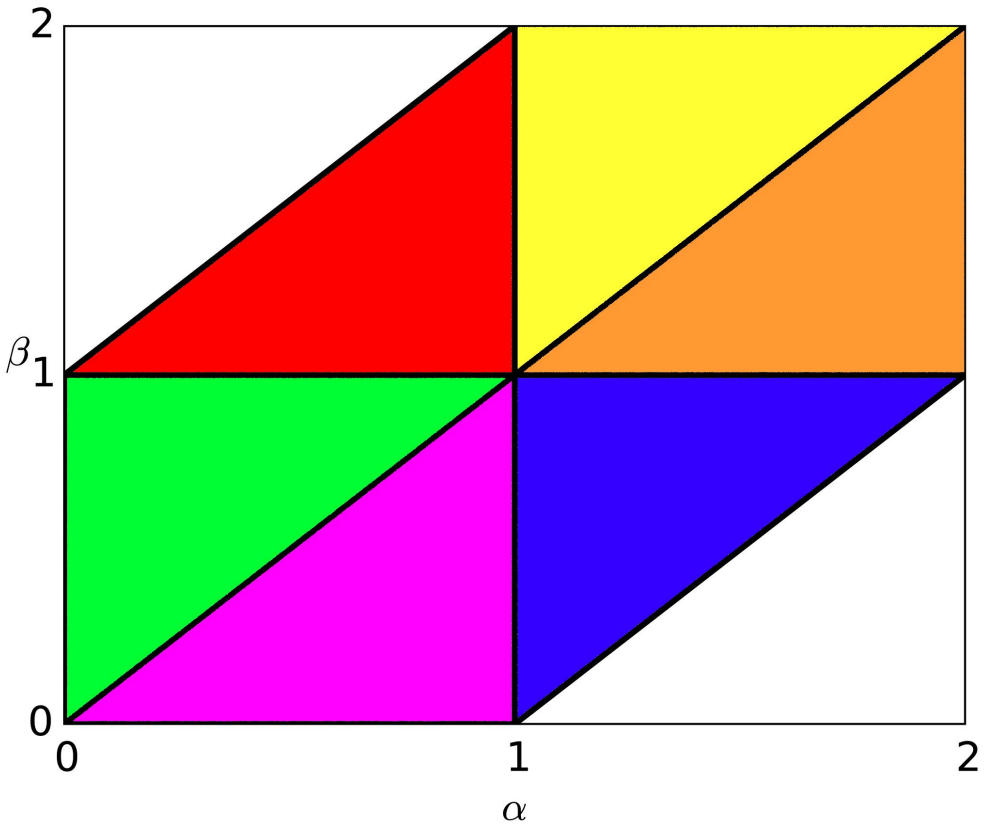

FIGURE 4.3: Diagonal lines $\alpha = \beta + C$ yield the same contact angle but the balance of surface energies is different. If $\alpha > \beta$, the contact angle $\theta < 90°$ (purple, blue, and orange regions). If $\alpha < \beta$, the contact angle $\theta > 90°$ (red, yellow, and green regions).

Therefore, Equation (4.3) can be written as $\Delta E = E_{\mathrm{b}} - E_{\mathrm{int}} = \gamma_{12}\left(A_{rm} + \cos\theta A_{p1}\right)$.

It is instructive to look at what other circumstances a particle will remain attached at the interface i.e. how the balance of surface energies affects the particle contact angle at an interface. To do this, we define two dimensionless parameters $\alpha = \frac{\gamma_{2p}}{\gamma_{12}}$ and $\beta = \frac{\gamma_{1p}}{\gamma_{12}}$ so that we can write Young's equation as

$$\cos\theta = \alpha - \beta. \tag{4.8}$$

The shaded areas of Figure 4.3 show the solution space of Young's equation i.e. values of surface energies γ_{1p}, γ_{2p}, and γ_{12} that give a contact angle $0 \leq \theta \leq 180$. The $\alpha = \beta$ diagonal corresponds to neutrally wetting particles, $\theta = 90°$. Any diagonal line of the

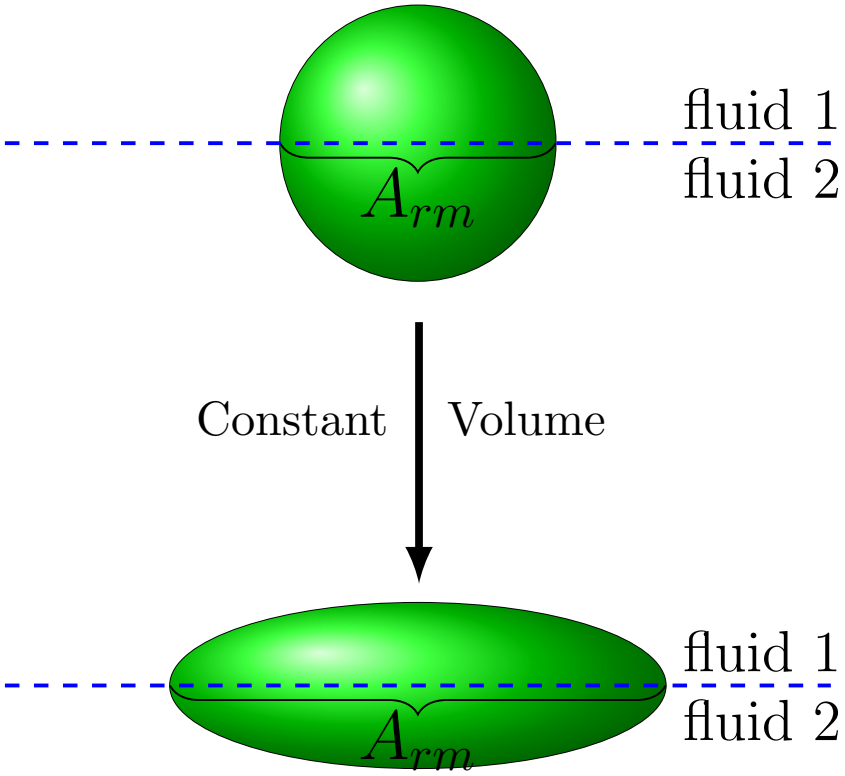

FIGURE 4.4: Anisotropic particles may remove more interface area than spherical particles for a given particle volume, requiring higher detachment energies and therefore potentially stabilising emulsions better.

form $\alpha = \beta + C$ is a line of constant contact angle. When $\alpha > \beta$, (the red, yellow, and green regions) $\theta < 90°$, and when $\alpha < \beta$ (the purple, blue, and orange regions) $\theta > 90°$.

Different ratios of surface energies can give identical contact angles. As an example, let's consider the $\alpha = \beta - 1/2$ diagonal line. If $\beta = 1/4$ then $\alpha = 3/4$, (purple region) meaning that both $\gamma_{12} > \gamma_{2p}$ and $\gamma_{12} > \gamma_{1p}$. Moving further along the diagonal line, if $\beta = 3/4$ then $\alpha = 5/4$ (blue region). In this case, $\gamma_{12} > \gamma_{1p}$ but $\gamma_{12} < \gamma_{2p}$. Finally, if $\beta = 5/4 \implies \alpha = 7/4$ (orange region), both $\gamma_{1p} > \gamma_{12}$ and $\gamma_{2p} > \gamma_{12}$. Yet all of these values of α and β give the same contact angle. The consequences of this subtlety on the formation of emulsions has yet to be explored.

4.1.3 Anisotropic Particles

Given that the area removed by the particle is a crucial parameter determining the detachment energy, it is clear that for a given particle volume, particles of other shapes

G. B. Davies et al. Detachment Energies of Spheroidal Particles from Fluid-Fluid Interfaces, *Journal of Chemical Physics*, 141, 154902 (2014) [1]. Reproduced with permission from [1].

may remove more interface area, as shown in Figure 4.4. A natural first step is to consider the detachment energy of spheroidal particles from interfaces.

Faraudo and Bresme [155] developed analytical expressions for the detachment energy of prolate and oblate spheroidal particles from a flat fluid-fluid interface, in both their perpendicular (symmetry axes perpendicular to the interface) and parallel (symmetry axes parallel to the interface) orientations, respectively:

$$\Delta E^{\perp} = \frac{\alpha}{4G}(1-\bar{h}^2) - \frac{\gamma_{2p}-\gamma_{1p}}{\gamma_{12}}\bar{A}^{\perp}_{2p}(\bar{h}), \tag{4.9}$$

$$\Delta E^{\parallel} = \frac{1}{4G}(1-\bar{h}^2) - \frac{\gamma_{2p}-\gamma_{1p}}{\gamma_{12}}\bar{A}^{\parallel}_{2p}(\bar{h}) \tag{4.10}$$

where $\alpha = R_{\parallel}/R_{\perp}$ is the particle aspect-ratio, $R_{\parallel}$ and $R_{\perp}$ are the radii parallel and orthogonal to the particle's symmetry axis, respectively. The dimensionless height $\bar{h} = h/R_{\perp}$ for prolate spheroidal particles in their equilibrium orientation, $\bar{h} = h/R_{\parallel}$ for oblate spheroidal particles in their equilibrium orientation, and G is a geometrical aspect factor:

$$G = \begin{cases} \frac{1}{2} + \frac{\alpha^2}{4\epsilon}\log\frac{1+\epsilon}{1-\epsilon} & \text{if } \alpha \leq 1 \\ \frac{1}{2} + \frac{1}{2}\frac{\alpha}{\epsilon}\sin^{-1}\epsilon & \text{if } \alpha \geq 1 \end{cases} \tag{4.11}$$

where $\epsilon = \sqrt{1-\alpha^2}$ and $\epsilon = \sqrt{1-\alpha^{-2}}$ is the eccentricity of oblate and prolate spheroidal particles, respectively. $\bar{A}^{\perp}_{2p}(\bar{h})$ and $\bar{A}^{\parallel}_{2p}(\bar{h})$ were incorrectly defined by Faraudo and Bresme [155], likely due to a typo. We corrected the equations:

$$\bar{A}^{\perp}_{2p} = \frac{\alpha}{\pi G(\alpha)}\int_0^1 \mathrm{d}x\sqrt{1-\left(1-\bar{h}^2\right)\left(1-\alpha^{-2}\right)x^2} \times \sqrt{1-\bar{h}^2}\tan^{-1}\left[\frac{1}{\bar{h}}\sqrt{\left(1-\bar{h}^2\right)\left(1-x^2\right)}\right], \tag{4.12}$$

$$\bar{A}^{\parallel}_{2p} = \frac{1}{2} - \frac{\alpha}{4G}\bar{h}\sqrt{1+\frac{\epsilon^2\bar{h}^2}{\alpha^2}} - \frac{\alpha^2}{4G\epsilon}\sinh^{-1}\left(\frac{\epsilon\bar{h}}{\alpha}\right). \tag{4.13}$$

G. B. Davies et al. Detachment Energies of Spheroidal Particles from Fluid-Fluid Interfaces, *Journal of Chemical Physics*, 141, 154902 (2014) [1]. Reproduced with permission from [1]. Copyright 2014, AIP Publishing LLC.

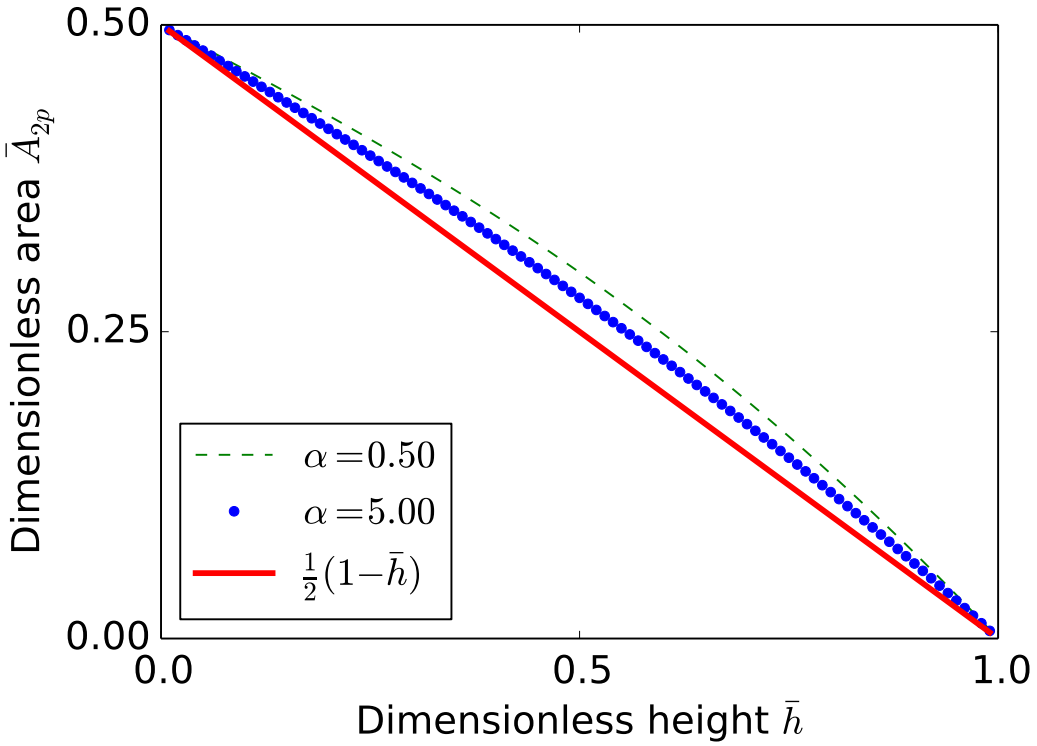

FIGURE 4.5: For $\alpha < 1$, $\bar{A}_{2p}^{\perp}$ (Equation (4.12)) is plotted (dashed line), and for $\alpha > 1$, $\bar{A}_{2p}^{\parallel}$ (Equation (4.13)) is plotted (dotted line). The results are compared with the function $A_{2p} = \frac{1}{2}(1-\bar{h})$ (solid line). The functions $\bar{A}_{2p}^{\perp}$ and $\bar{A}_{2p}^{\parallel}$ are well approximated by the function $\frac{1}{2}(1-\bar{h})$. Reproduced with permission from [1]. Copyright 2014, AIP Publishing LLC.

and they represent the dimensionless area of a particle immersed in bulk fluid 2, so that $A_{2p} = 1/2$ corresponds to a neutrally wetting particle, and $A_{2p} = 0$ corresponds to a particle detached into the bulk fluid. The detachment energy depends on the orientation of the particle on the interface. Here, we focus on oblate and prolate spheroidal particles in their equilibrium orientation: for a oblate spheroidal particles, that is with its symmetry axis parallel to the interface normal; for a prolate spheroidal particle, that is with its symmetry axis perpendicular to the interface normal.

G. B. Davies et al. Detachment Energies of Spheroidal Particles from Fluid-Fluid Interfaces, *Journal of Chemical Physics*, 141, 154902 (2014) [1]. Reproduced with permission from [1].

4.2 Results

Though exact, the model developed by Faraudo and Bresme [155] in Equations (4.9) and (4.10) presents some challenges if they are to be used in practice. Firstly, the particle-fluid surface energies, γ_{2p} and γ_{1p}, are extremely difficult to measure experimentally, and in our Shan-Chen multicomponent lattice Boltzmann model, impossible, since we can control the contact angle only by tuning dimensionless coupling parameters between the fluid and particle (e.g. the particle colour parameter as described in Chapter 3). Rather than measure the individual surface tension terms, researchers mostly gain information about them by measuring the contact angle of the particle using Young's relation (Equation (4.7)). However, as I showed earlier, many different combinations of the individual surface tension terms give rise to the same particle contact angle.

Secondly, the area terms $\bar{A}_{2p}^{\perp}$ and $\bar{A}_{2p}^{\parallel}$ are cumbersome to calculate, and in the case of the $\bar{A}_{2p}^{\perp}$ term, need to be calculated numerically. We sought to develop an approximate, more practical model.

We simplified the area terms $\bar{A}_{2p}^{\perp}$ and $\bar{A}_{2p}^{\perp}$ by arguing that for typical experimental aspect-ratios, $0.5 < \alpha < 5.0$, the area terms do not deviate significantly from the area of a spherical particle, as shown in Figure 4.5. Then, we can approximate the dimensionless area as:

$$A_{2p} = \frac{1}{2}\left(1 - \bar{h}\right). \tag{4.14}$$

We also sought to eliminate the surface energy terms in Equations (4.9) and (4.10). We first note that for a spherical particle ($\alpha = 1$) $\frac{\gamma_{2p}-\gamma_{1p}}{\gamma_{12}} = \cos\theta = \bar{h}$ is simply the cosine of the contact-angle of the particle, θ, which is also equal to the dimensionless height, $\bar{h}$, of the particle (Figure 4.2). The dimensionless height, $\bar{h} = h/R$, is the height of the particle centre-of-mass, h, normalised by the particle radius R.

We assumed that this relation is also true for prolate and oblate spheroidal particles, provided a suitable choice of the particle radius, R, is made, since there are two radii to choose from for a spheroidal particle: $R_{\perp}$ and $R_{\parallel}$.

G. B. Davies et al. Detachment Energies of Spheroidal Particles from Fluid-Fluid Interfaces, *Journal of Chemical Physics*, 141, 154902 (2014) [1]. Reproduced with permission from [1].

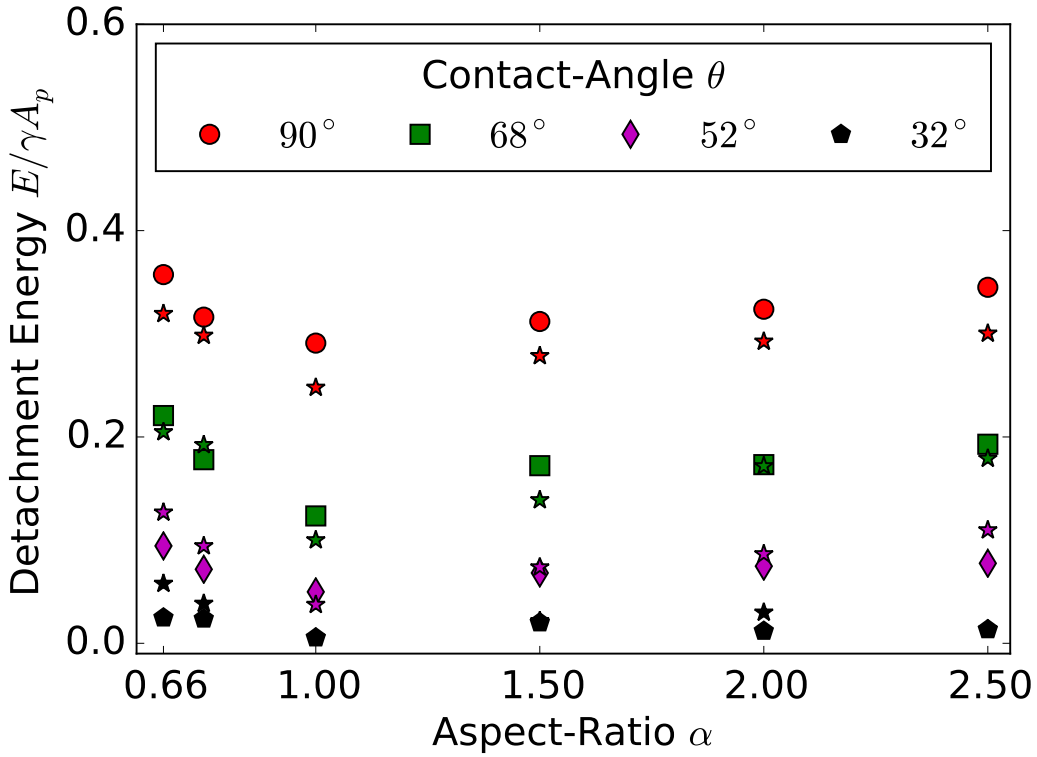

FIGURE 4.6: Dependence of the detachment energy, ΔE, on the aspect ratio, α, for several different contact angles, θ. Each set of coloured data points represents different wettabilities of the particles. Stars are theoretical calculations from our thermodynamic model in Eq. (4.15) and Eq. (4.16) and symbols are numerical data. Reproduced with permission from [1]. Copyright 2014, AIP Publishing LLC.

We use the radius that is orthogonal to the interface for a particle in its equilibrium orientation at an interface. For oblate spheroidal particles, that is $\bar{h} = \frac{h}{R_\parallel}$, and for prolate spheroidal particles, $\bar{h} = \frac{h}{R_\perp}$. These simplifications allow us to derive a simplified expressions for the detachment energy that are quadratic functions of the particle aspect-ratio, α, and its dimensionless height above the interface, $\bar{h}$, only:

$$\Delta E^\perp = \frac{\bar{h}^2}{2}\left(1 - \frac{\alpha}{2G(\alpha)}\right) - \frac{\bar{h}}{2} + \frac{\alpha}{4G(\alpha)}, \tag{4.15}$$

$$\Delta E^\parallel = \frac{\bar{h}^2}{2}\left(1 - \frac{\alpha}{2G(\alpha)}\right) - \frac{\bar{h}}{2} + \frac{1}{4G(\alpha)}, \tag{4.16}$$

where $\Delta E^\perp$ and $\Delta E^\parallel$ are the detachment energies of an oblate and prolate spheroidal particle in their equilibrium positions at an interface, respectively. For a neutrally

G. B. Davies et al. Detachment Energies of Spheroidal Particles from Fluid-Fluid Interfaces, *Journal of Chemical Physics*, 141, 154902 (2014) [1]. Reproduced with permission from [1]. Copyright 2014, AIP Publishing LLC.

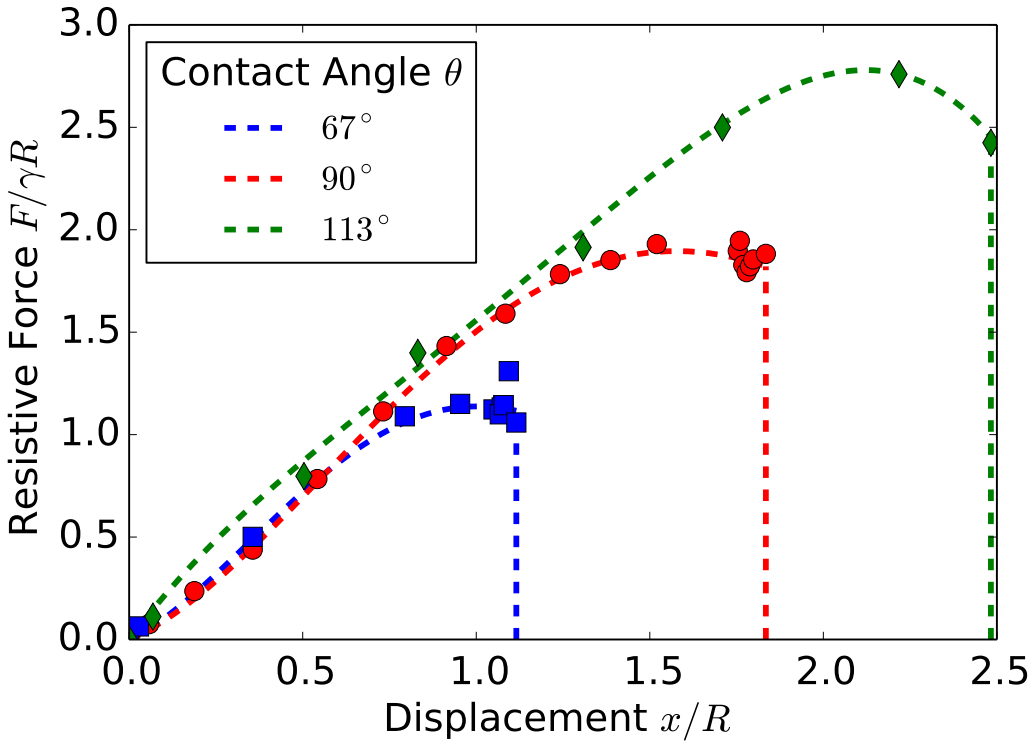

FIGURE 4.7: Sample force—distance curve for a spherical particle with radius $R = 10$ lattice units detaching from an interface with surface tension $\gamma = 0.0633$ in lattice units. We obtain the detachment energy by integrating the force—distance curves for a given set of particle parameters. We observe a previously predicted linear force regime for small particle displacements [22–26]. Reproduced with permission from [1]. Copyright 2014, AIP Publishing LLC.

wetting particle, $\bar{h} = 0$ and Equations (4.15) and (4.16) become $\Delta E^{\perp} = \frac{\alpha}{4G}$ and $\Delta E^{\parallel} = \frac{1}{4G}$ respectively. Our theoretical model exhibits several important features; firstly, it recovers the exact equations for the detachment energy of a spherical particle ($\alpha \to 1$). Secondly, it shows that for a given particle volume, spherical particles do indeed have the lowest detachment energy when compared with oblate and prolate spheroidal particles of the same volume, as shown by the star symbols in Figure 4.6.

To validate our simplified theoretical model, we performed lattice Boltzmann simulations of spherical and spheroidal particles detaching from an interface. We quasi-statically detach a particle from the interface by applying a constant force that is large enough to detach the particle from the interface. After an arbitrary time interval, we fix the position of the particle and allow the system to equilibrate and measure the force on the particle, which is purely the resistive force applied by the interface to the particle.

G. B. Davies et al. Detachment Energies of Spheroidal Particles from Fluid-Fluid Interfaces, *Journal of Chemical Physics*, 141, 154902 (2014) [1]. Reproduced with permission from [1]. Copyright 2014, AIP Publishing LLC.

Doing this, we calculate the detachment energy by integrating the force, F, as a function of the particle displacement from the interface, Δx.

Figure 4.7 shows a sample force—distance curve for a spherical particle with radius $R = 10$ lattice units detaching from a fluid-fluid interface with surface tension $\gamma = 0.0633$ in lattice units for several different contact angles. The resistive force applied to the particle by the interface is linear for small particle displacements, regardless of contact angle, agreeing with the simple spring model developed by Joanny and de Gennes [24] and others [22, 23]. Chateau and Pitois [25] experimentally investigated the detachment of spherical particles from fluid-fluid interfaces, also finding a linear force regime for small particle displacements [26].

In Figure 4.6, we compare our analytical model (stars) to our numerical results (symbols), finding broadly good agreement between them. Note that our numerical simulations measure a higher detachment energy than theoretically predicted, even for spherical particles. This is because the theoretical model we developed for the detachment energy is simply a free energy difference between a particle in the bulk and a particle adsorbed at an interface, and does not account for the energy barrier between the two states: in order to detach a particle, the particle must deform the interface and overcome the interface's resistive force.

The good agreement between our theoretical model and simulation data suggest that our various approximations, in particular our assumption that $\frac{\gamma_{2p}-\gamma_{1p}}{\gamma_{12}} \mapsto \bar{h}$ for suitably chosen dimensionless heights, are valid for the particle properties we investigated. Further investigations into the precise relationship between the balance of surface energies and the particle contact angle are needed to ascertain the exact relationship between these variables.

4.3 Conclusions

In this Chapter, we developed a simple analytical model to describe the detachment energy of anisotropic particles from a fluid-fluid interface. The model is valid for oblate spheroidal and prolate spheroidal particles adsorbed at an interface in their equilibrium orientations, which is with their symmetry axes perpendicular and parallel to the interface, respectively.

G. B. Davies et al. Detachment Energies of Spheroidal Particles from Fluid-Fluid Interfaces, *Journal of Chemical Physics*, 141, 154902 (2014) [1]. Reproduced with permission from [1].

In order to make a useful model, we made several simplifications and assumptions. Firstly, we assumed that Young's equation can be replaced by the dimensionless height of the particle. This assumption is true for spherical particles but for anisotropic particles a suitable particle radius must be chosen. We chose the axis radius that is orthogonal to the interface when the particle is adsorbed in its equilibrium orientation. Further simulations and experiments must be carried out to test the range of validity of this simplification.

Secondly, we showed that the area of immersion of the particle into one of the fluids does not deviate significantly from that of a spherical particle for experimentally accessible aspect ratios. We then simplified the calculation of these immersion areas by assuming that for a given dimensionless height of the particle, the immersion area is the same as for a spherical particle with the same dimensionless height.

Our simplified model recovered the known equations for the detachment energy of a spheroidal particle in the spherical particle limit $\alpha \to 1$. Our model predicts that for a given particle volume, spherical particles have a smaller detachment energy than for either oblate or prolate spheroidal particles of any anisotropy.

We carried out lattice Boltzmann simulations of both oblate and prolate spheroidal particles detaching from a fluid-fluid interface, and measured the detachment energy by integrating – in a quasi-static fashion – the force-distance curve as the particle detaches from the interface. We kept the particle volumes constant and varied the contact angle/dimensionless heights of the particles.

When compared with our theoretical model, we found excellent qualitative agreement with our simulation data. Quantitatively, our simulations measured a higher detachment energy than the theoretical model due to the fact that our simulation measurements capture the energy needed to deform the interface during detachment; our theoretical model takes into account only the free energy difference between a particle adsorbed at an interface and fully detached into one of the bulk fluids.

Recent experiments on the physical ageing of the contact line of spherical colloidal particles revealed a sudden breach of the contact line during initial particle adsorption at the interface followed by a logarithmic relaxation of the contact line [156, 157]. Our results present the theoretical foundations for carrying out such a study using oblate

G. B. Davies et al. Detachment Energies of Spheroidal Particles from Fluid-Fluid Interfaces, *Journal of Chemical Physics*, 141, 154902 (2014) [1]. Reproduced with permission from [1].

and prolate spheroidal particles, which could help to isolate the relevant mechanisms for the unexpected contact line ageing.

G. B. Davies et al. Detachment Energies of Spheroidal Particles from Fluid-Fluid Interfaces, *Journal of Chemical Physics*, 141, 154902 (2014) [1].

Chapter 5

How Much Energy Does it Take to Rotate a Particle at a Fluid-Fluid Interface?

"The dipole would dominate if the particles were under the effect of an external torque with vanishing net external force; so far there does not seem to be any clear experimental realisation of this possibility" — Alvaro Domínguez [158].

5.1 Introduction

Our study of prolate and oblate spheroidal particles detaching from an interface leads to a natural question: since anisotropic particles have more than one possible orientation at an interface, how does the free energy of the particle change as its orientation at the interface changes?

Bresme and Faraudo [27] investigated the behaviour of a magnetic prolate spheroidal particle with its dipole-axis, $\boldsymbol{\mu}$, aligned with its symmetry axis influenced by a magnetic field, $\mathbf{H}$, applied perpendicular to the interface (Figure 5.1) [27, 159]. The particle experiences a torque $\mathbf{T} = \boldsymbol{\mu} \times \mathbf{H}$ that tries to align the particle's dipole moment, $\boldsymbol{\mu}$, with the external magnetic field, $\mathbf{H}$. But, surface tension forces oppose the rotation, and so for a given dipole-field strength, $B = |\boldsymbol{\mu}||\mathbf{H}|$, the particle tilts with respect to the

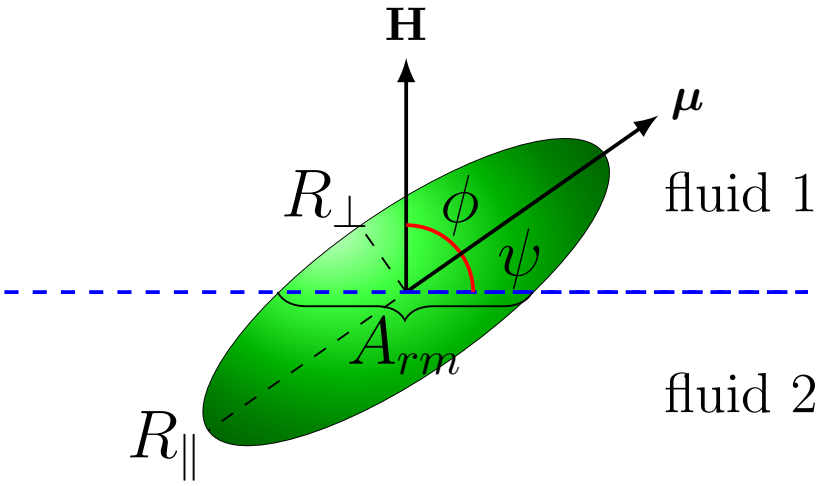

FIGURE 5.1: A single prolate spheroidal magnetic particle with dipole-moment $\boldsymbol{\mu}$ adsorbed at a fluid-fluid interface under the influence of an external magnetic field $\mathbf{H}$ applied normal to the interface. The tilt-angle ψ is related to the dipole-angle, $\phi = \pi/2 - \psi$. A_{rm} is the area removed from the interface by the particle, and the ratio of the long-axis radius, $R_{\parallel}$, to the short-axis radius, $R_{\perp}$, determines the aspect-ratio, $\alpha = R_{\parallel}/R_{\perp}$.

interface. They developed a free energy model that assumes that the interface remains flat and undeformed during tilting:

$$\Delta\bar{F}_{int} = \frac{\Delta F_{int}}{A_p\gamma_{12}} = -\frac{B\sin(\psi)}{A_p\gamma_{12}} - \frac{\alpha}{4G(\alpha)}\sqrt{\frac{1}{\cos^2(\psi)+\alpha^2\sin^2(\psi)}} \tag{5.1}$$

where $\alpha = R_{\parallel}/R_{\perp}$ is the particle aspect ratio, ψ is the particle tilt-angle, A_p is the total surface area of the particle, and γ_{12} is the surface tension of the fluid-fluid interface.

Bresme and Faraudo [27] minimised the free energy of the particle with respect to the tilt angle ψ as a function of both aspect-ratio for a given dipole-field strength (Figure 5.2a) and dipole-field strength for a given aspect ratio (Figure 5.2b). Figure 5.2a shows that the equilibrium tilt-angle ψ (They denote the tilt-angle by θ, which is equal to ψ in Equation (5.1) and Figure 5.1) for a given dipole-field strength depends on the particle aspect-ratio i.e. particles with different aspect ratios will assume a different tilt angle at the interface for the same dipole-field strength.

G. B. Davies et al. Interface Deformations Affect the Orientation Transition of Magnetic Ellipsoidal Particles Adsorbed at Fluid-Fluid Interfaces, *Soft Matter*, 10, 6742-6748 (2014) [2]. Reproduced from Ref. [2] with permission from The Royal Society of Chemistry.

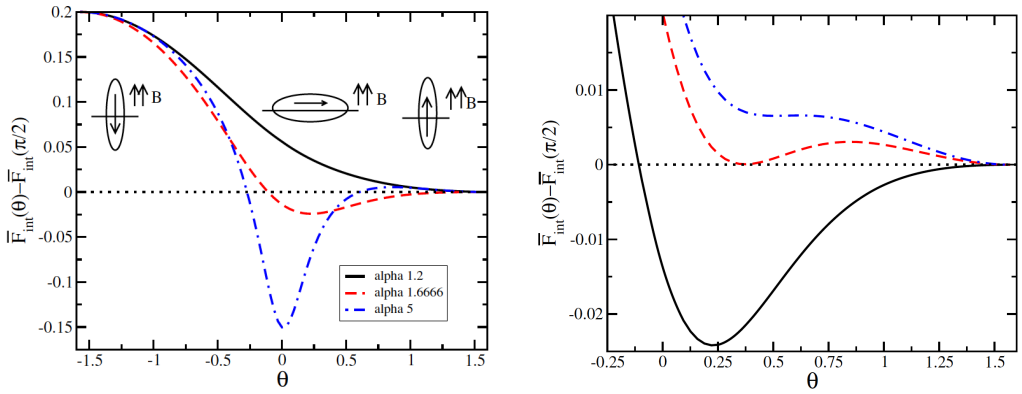

(A) (B)

FIGURE 5.2: Figure 5.2a shows that the equilibrium tilt-angle, θ, which is the tilt-angle that minimises the free energy for a given dipole-field strength, B, decreases as the aspect-ratio, α, increases, for a given dipole-field strength. Figure 5.2b shows that the tilt-angle increases as the dipole-field strength increases for a given aspect ratio $\alpha = 1.66$, and we can clearly see the first order nature of the transition. Additionally, we observe a meta-stable state for certain dipole-field strengths. Note that we denote the tilt angle by ψ instead of θ. Reprinted from [27] with permission from IOP.

Additionally, Figure 5.2b shows that for a given aspect-ratio, the equilibrium tilt-angle increases as the dipole-field strength increases, until a metastable state forms (red dashed lines). At the onset of the metastable state the tilted and vertical configurations are equal in energy, but an energy barrier prevents the particle transitioning to the vertical state. Eventually, the dipole-field strength reaches a critical value, B_c (blue dashed line in Figure 5.2b), and the free energy barrier characteristic of a metastable state disappears, causing the particle to *flip* from a tilted orientation to a vertical orientation aligned with the external field: the particle undergoes a first order phase transition.

Bresme and Faraudo [27] and Bresme [159] carried out Monte-Carlo simulations to confirm the predictions of their model, which showed good agreement. However, identifying the transition proved difficult due to the increasing relevance of thermal fluctuations in their simulations. We set out to see whether the predicted first-order orientation phase transition exists using our lattice Boltzmann model described in Chapter 3.

5.2 Results: Interface Deformations Affect the Orientation Transition

We carried out lattice Boltzmann simulations of magnetic particles adsorbed at fluid-fluid interfaces under the influence of an external magnetic field as described above

G. B. Davies et al. Interface Deformations Affect the Orientation Transition of Magnetic Ellipsoidal Particles Adsorbed at Fluid-Fluid Interfaces, *Soft Matter*, 10, 6742-6748 (2014) [2]. Reproduced from Ref. [2] with permission from The Royal Society of Chemistry.

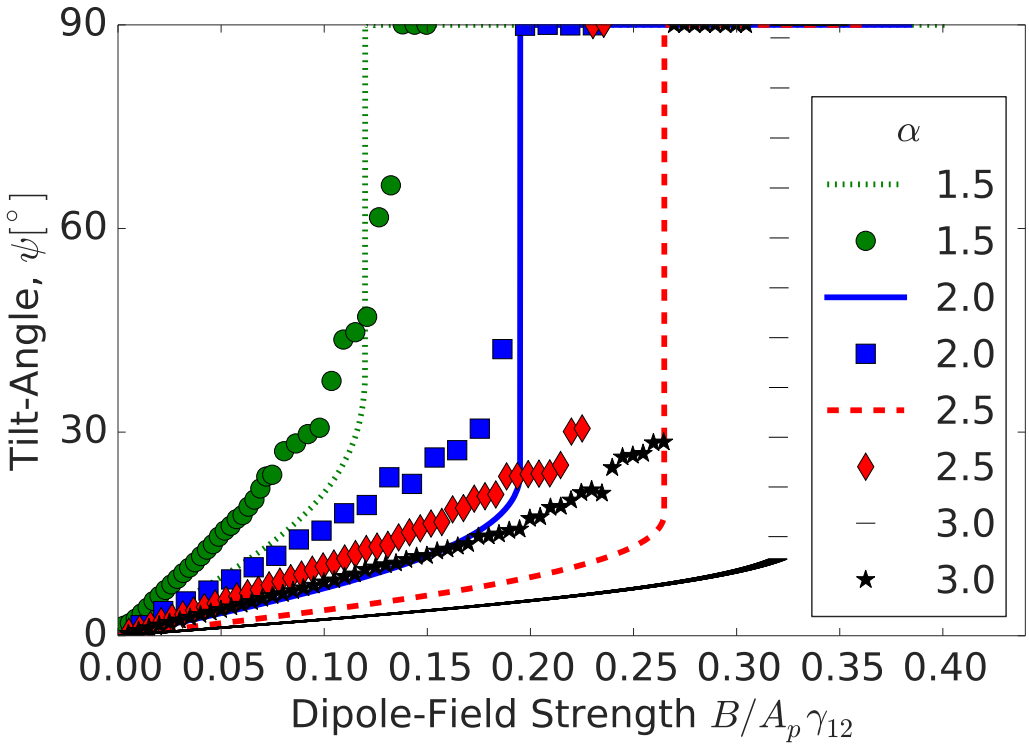

FIGURE 5.3: We confirmed that the first order orientation transition exists, but there are large differences in tilt angle for a given dipole-field strength, critical tilt angle, and critical dipole-field strength between our numerical data and the theoretical predictions. The differences get larger as the particle aspect-ratio increases. Reproduced from Ref. [2] with permission from The Royal Society of Chemistry.

(Figure 5.1), for several different aspect-ratios. We observed that the particle tilt angle ψ discontinuously jumps for a critical dipole-field strength B_c for all aspet-ratios we investigated ($\alpha = 1.5$, 2.0, 2.5, and 3.0), confirming that the first-order orientation phase transition exists, as shown by the symbols in Figure 5.3.

However, we found large differences between the theoretically predicted tilt angles for a given dipole-field strength, as well as the theoretically predicted critical dipole-field strengths and critical tilt angles, as shown in (Figure 5.3). Furthermore, we found that these differences increased as the particle aspect-ratio increased, with aspect ratio $\alpha = 3$ particles showing the largest discrepancy between theory and simulation.

In order to find the cause of this difference, we looked at the contact line and interface deformation as the particle tilts on the interface. Figure 5.4 shows both (A) a snapshot of the interface deformation profile from our numerical simulations and (B) a schematic illustrating the difference between the predicted contact line according to the model

G. B. Davies et al. Interface Deformations Affect the Orientation Transition of Magnetic Ellipsoidal Particles Adsorbed at Fluid-Fluid Interfaces, *Soft Matter*, 10, 6742-6748 (2014) [2]. Reproduced from Ref. [2] with permission from The Royal Society of Chemistry.

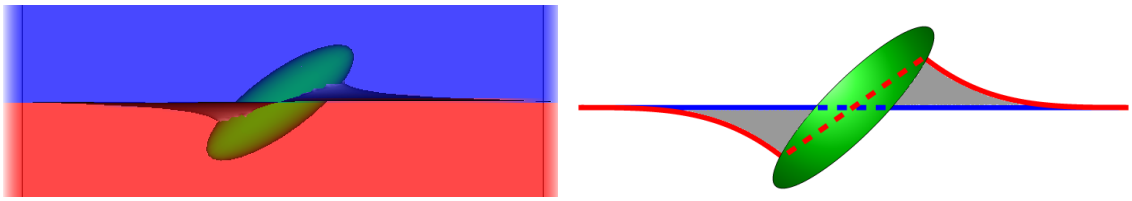

(A) (B)

FIGURE 5.4: (A) Snapshot of interface deformation from numerical lattice Boltzmann simulations during particle tilting. Significant interface deformation can be seen. (B) Schematic of the theoretically predicted interface profile (blue) compared with the interface profile observed in simulations (red). The particle removes more interface area than theoretically predicted, while at the same time it creates more interface area due to the pinning of the contact line to the particle. Reproduced from Ref. [2] with permission from The Royal Society of Chemistry.

of Bresme and Faraudo [27] (blue solid and dashed lines) and a representation of the real contact line (red solid and dashed lines).

Figure 5.4 shows that the particle removes more interface area during tilting than theoretically predicted. However, at the same time, the particle causes the interface to curve, creating additional interface area. It is the balance of these two effects that determines the total interface area removed by the presence of the particle including the deformations, $A_{rm,d}$.

We quantitatively investigated the total interface area $\Delta A = A_{rm,d}(\psi = 0°) - A_{rm,d}(\psi)$ as a function of the tilt angle, as shown in Figure 5.5. $A_{rm,d} = A_{12} - A_{12,d}$ is the area removed by the particle including the additional interface area due to curvature, where A_{12} is the area of the undeformed interface and $A_{12,d}$ is the total area of the interface including interface deformation. $A_{rm,d}$ converges to A_{rm} in the flat interface limit, i.e. $\psi = 0°$ or $90°$, and we therefore recover Equation (5.1) in these limits. Figure 5.5 shows that during tilting the particle reduces the total area of the interface compared with the analytical predictions that assume no interface deformations i.e. the particle removes more interface area, even when we account for the additional interface area due to curvature. Additionally, we found that these differences increased with the particle aspect ratio α, suggesting that these differences in predicted and realised interface area could be the cause of the differences observed in Figure 5.3.

We adapted the free energy model in Equation (5.1) to include interface deformations:

G. B. Davies et al. Interface Deformations Affect the Orientation Transition of Magnetic Ellipsoidal Particles Adsorbed at Fluid-Fluid Interfaces, *Soft Matter*, 10, 6742-6748 (2014) [2]. Reproduced from Ref. [2] with permission from The Royal Society of Chemistry.

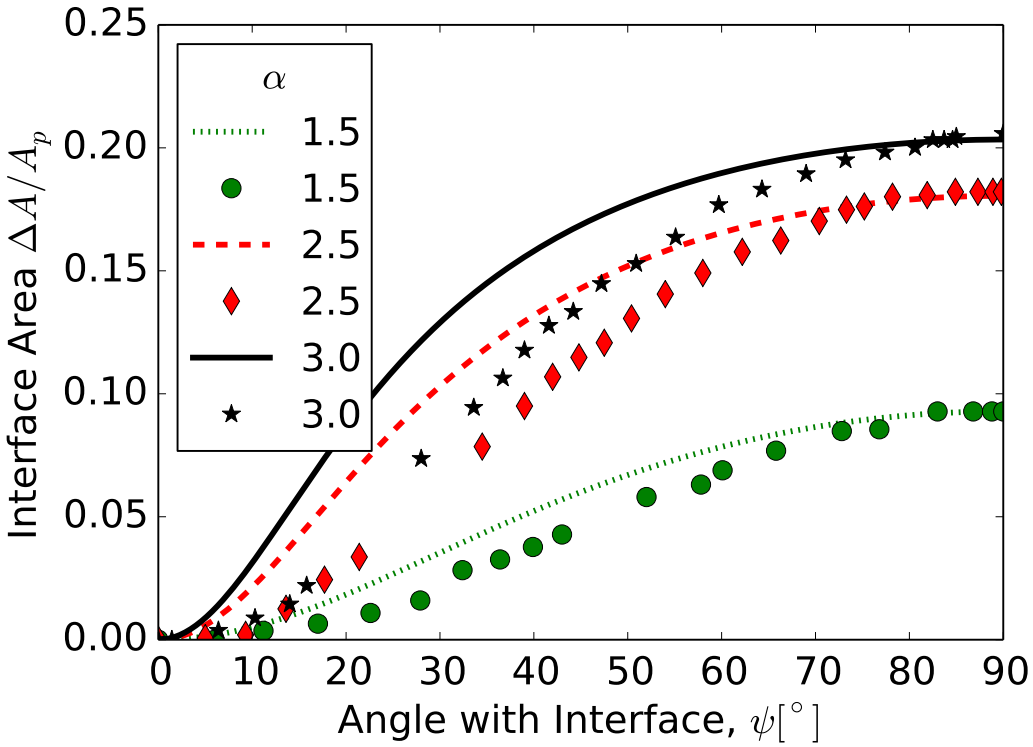

FIGURE 5.5: We compare the numerically measured total interface area ΔA including deformations (symbols) with the analytically predicted interface area (lines) as the particle tilt angle varies. We find that when we include interface deformations, the total interface area is smaller: the particle removes more interface area than theoretically predicted. Reproduced from Ref. [2] with permission from The Royal Society of Chemistry.

$$\Delta F_{int,d}(\psi) = -\gamma_{12}\left(A_{12} - A_{12,d}(\psi)\right) - B\sin\psi \tag{5.2}$$

We then fitted the numerically measured interface area removed $A_{rm,d}(\psi)$ shown in Figure 5.5 to a slightly modified analytical model based on Equation 5.1, $A_{rm,d} = c + \frac{\pi a b^2}{\sqrt{a^2\cos^2\psi + b^2\sin^2\psi}}$, where a, b, and c are free fitting parameters. The equilibrium tilt angle for a given dipole-field strength can then be obtained by minimizing $\Delta F_{int,d}$ with respect to ψ. Upon doing so, we obtained nearly perfect agreement between our numerical data and the theoretical predictions, as shown in Figure 5.6.

Therefore, we showed that interface deformations significantly affect the orientation of the particle as it rotates at the interface. The crucial point is that since we obtain the equilibrium tilt angle by minimising the free energy with respect to the tilt angle,

G. B. Davies et al. Interface Deformations Affect the Orientation Transition of Magnetic Ellipsoidal Particles Adsorbed at Fluid-Fluid Interfaces, *Soft Matter*, 10, 6742-6748 (2014) [2]. Reproduced from Ref. [2] with permission from The Royal Society of Chemistry.

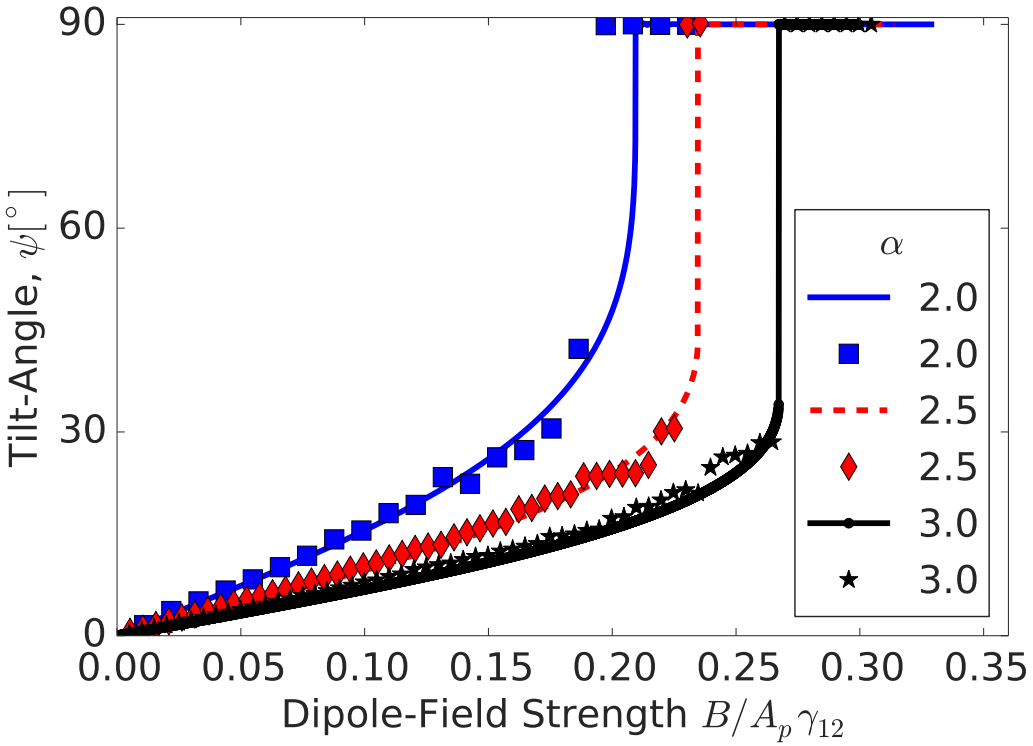

FIGURE 5.6: When comparing numerically measured data (symbols) against our new free energy model in Equation (5.1) (lines), the model and the data agree nearly perfectly. We conclude that Interface deformations explain the difference between the theoretical model and the numerical data. Reproduced from Ref. [2] with permission from The Royal Society of Chemistry.

$\frac{\partial F}{\partial \psi} = 0$, the tilt angle strongly depends on how the area removed changes with respect to the tilt angle:

$$\frac{1}{\cos\psi}\frac{dA_{rm}(\psi)}{d\psi} = \frac{B}{\gamma} \tag{5.3}$$

and not the absolute value of the removed area.

Finally, we noticed that during tilting, the particle deforms the interface in a dipolar manner, as shown in Figure 5.7. The particle depresses the interface on one tip and elevates it on the other, with equal deformation magnitude at each tip. These deformations act as capillary charges that attract and repel each other depending on whether they depress or elevate the interface, as described in Chapter 2 and shown in Figure 2.5.

G. B. Davies et al. Interface Deformations Affect the Orientation Transition of Magnetic Ellipsoidal Particles Adsorbed at Fluid-Fluid Interfaces, *Soft Matter*, 10, 6742-6748 (2014) [2]. Reproduced from Ref. [2] with permission from The Royal Society of Chemistry.

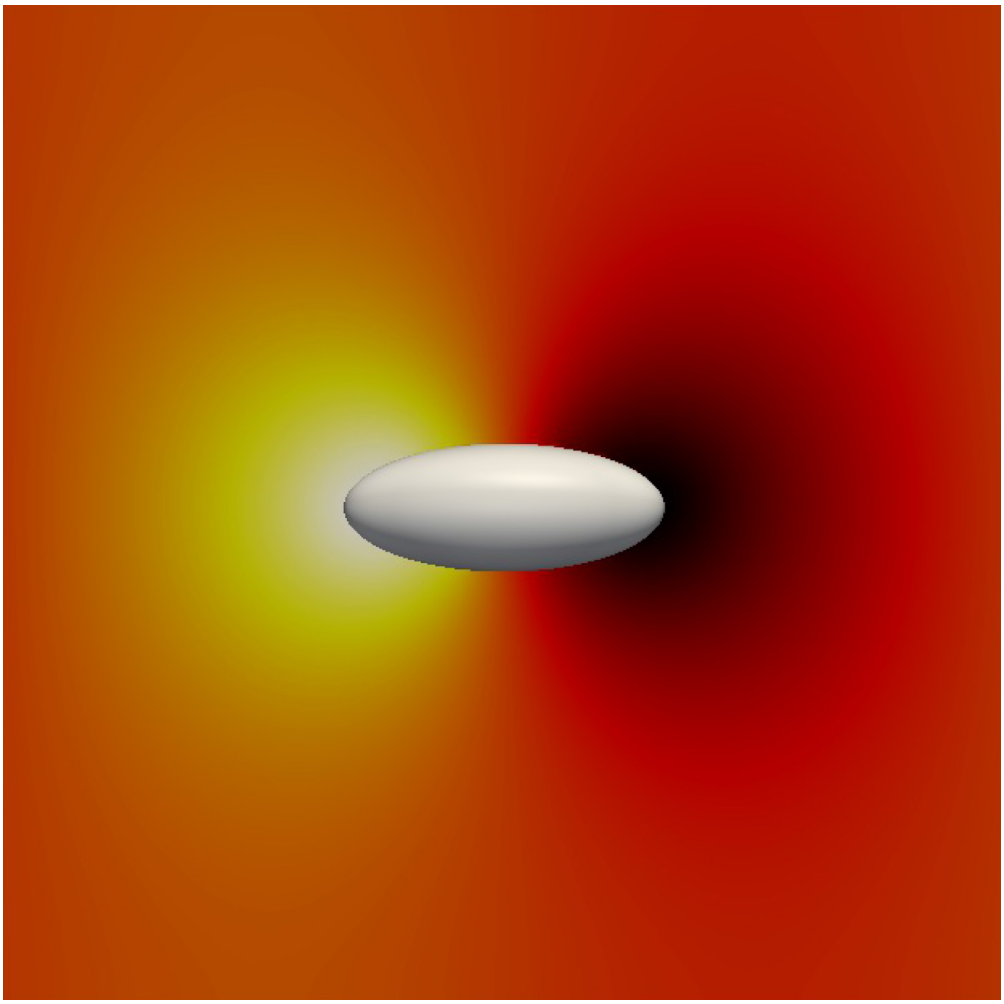

FIGURE 5.7: As the particle tilts with respect to the interface in response to the external magnetic field, it deforms the interface in a dipolar fashion. The colours denote the height profile of the interface: black represents elevations and yellow represents depressions. Reproduced from Ref. [2] with permission from The Royal Society of Chemistry.

A significant difference between the dipolar interactions that we discovered and previously discovered capillary interactions is that our dipolar capillary interactions are tunable: Figure 5.5 shows that the magnitude of the interface deformations increases with tilt angle until we reach the critical tilt angle, ψ_c. Controlling the magnitude of the interface deformations allows you to control the magnitude of the capillary interactions between the particles, since the capillary interaction energy between two polar dipoles depends on the maximal particle-induced interface deformation height for the two particles, H_A and H_B:

G. B. Davies et al. Interface Deformations Affect the Orientation Transition of Magnetic Ellipsoidal Particles Adsorbed at Fluid-Fluid Interfaces, *Soft Matter*, 10, 6742-6748 (2014) [2]. Reproduced from Ref. [2] with permission from The Royal Society of Chemistry.

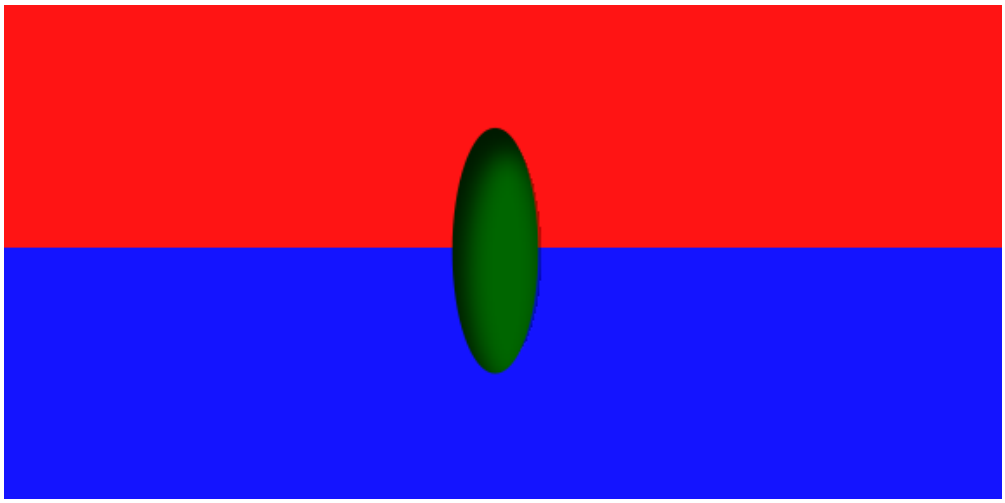

FIGURE 5.8: Simulation snapshot showing the lack of interface deformation when the particle transitions into the vertical state.

$$E_{AB} = 2\pi\gamma_{12} H_A H_B r_c^2 r_{AB}^{-2} \cos(\psi_A + \psi_B) \tag{5.4}$$

where the other parameters are defined in Chapter 2 and the full derivation of this result is included in Appendix B.

One final point of significance is that when the particle transitions into the vertical state aligned with the external magnetic field, the interface deformations disappear due to the symmetry of the contact line, as shown in Figure 5.8. Therefore, we can turn capillary interactions between particles on and off by exceeding the critical dipole-field strength, which causes the particles to transition into the vertical state.

Our work has therefore uncovered the prospect of dynamically controlling the assembly of particles at fluid-fluid interfaces using induced dipolar capillary interactions, which we discuss in Chapter 4.

5.3 Recent Advances

Shortly after we published our paper, Newton et al. [28] followed up with some significant and interesting new results. They used Surface Evolver [74] simulations to fix the orientation of a particle and measure the resulting interface area for a given tilt angle.

G. B. Davies et al. Interface Deformations Affect the Orientation Transition of Magnetic Ellipsoidal Particles Adsorbed at Fluid-Fluid Interfaces, *Soft Matter*, 10, 6742-6748 (2014) [2]. Reproduced from Ref. [2] with permission from The Royal Society of Chemistry.

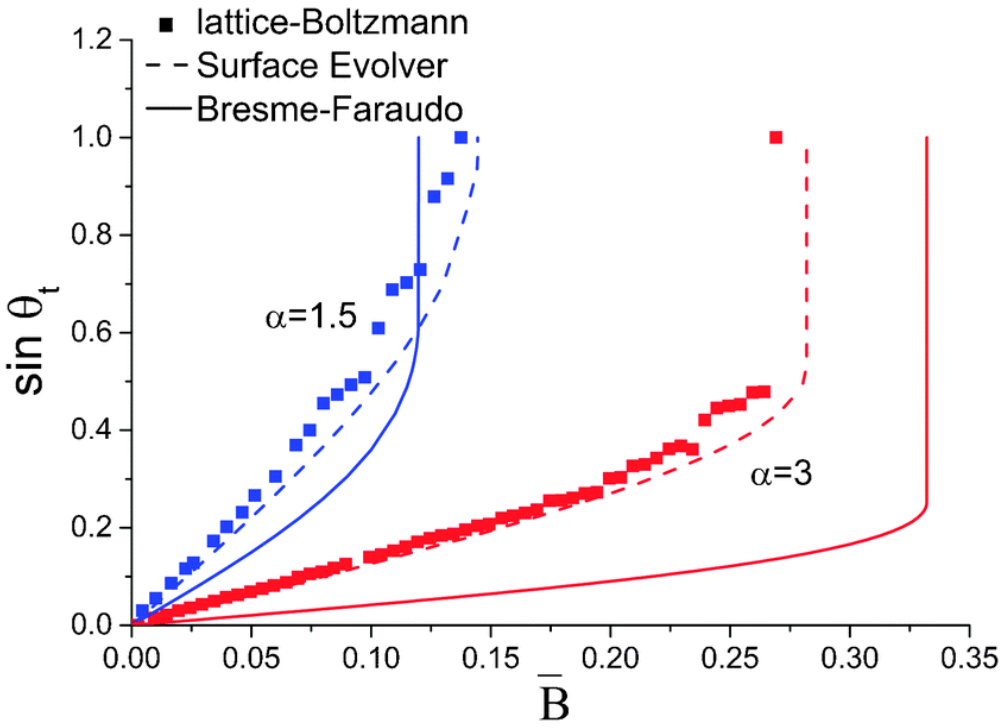

FIGURE 5.9: Comparison of Bresme-Faraudo theory (solid lines) with Surface Evolver numerical simulations (dotted lines) and our lattice Boltzmann simulations (symbols). They found good agreement between the Surface Evolver simulations, which include interface deformations, and our lattice Boltzmann simulations, which also include deformations. In this Figure, $\theta_t = \psi$ in our model (Equation (5.1)). Reproduced from Ref [28] with permission of the PCCP Owner Societies.

They noted that since the left hand side of the free energy minimum in Equation (5.3) is independent of the dipole-field strength, B, one can calculate the equilibrium tilt angle as a function of the dipole-field strength. They found excellent agreement with our lattice Boltzmann simulations, as shown in Figure 5.9. Secondly, they showed that hysteresis should exist due to the first order transition. Since there is a metastable state during particle tilting (Figure 5.2b), the equilibrium tilt angle depends on whether the field increases from a tilt angle $\psi = 0°$ or decreases from a tilt angle $\psi = 90°$, because of the free energy barrier separating the lowest energy orientations. Therefore, two critical dipole-field strengths, B_{c1} and B_{c2}, and two critical tilt angles ψ_{c1} and ψ_{c2} emerge, respectively. They showed that the interface deformations significantly decrease the amount of hysteresis predicted by Bresme-Faraudo theory (i.e. the area enclosed by the hysteresis curves), as shown in Figure 5.10.

They investigated the dependence of the critical tilt angles on the aspect ratio, as shown in Figure 5.11a. They found that both critical tilt angles decrease as the aspect ratio

G. B. Davies et al. Interface Deformations Affect the Orientation Transition of Magnetic Ellipsoidal Particles Adsorbed at Fluid-Fluid Interfaces, *Soft Matter*, 10, 6742-6748 (2014) [2]. Reproduced from Ref. [2] with permission from The Royal Society of Chemistry.

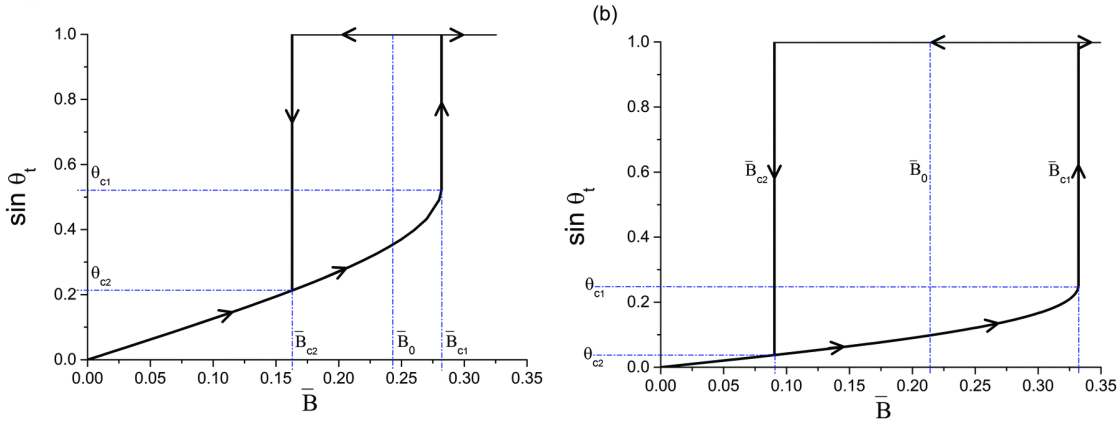

(A) Surface Evolver simulations (B) Bresme-Faraudo theory

FIGURE 5.10: Sample hysteresis loops for a neutrally wetting particle with aspect ratio $\alpha = 3$ according to Surface Evolver simulations (A) and Bresme-Faraudo theory (B). When interface deformations are included (A), the hysteresis loop encloses a smaller area than Bresme-Faraudo theory predicts (B). Reproduced from Ref [28] with permission of the PCCP Owner Societies.

increases to $\alpha = 6$, both in Bresme-Faraudo theory and in their numerical simulations, as shown in Figure 5.11a. Intriguingly, the difference between their Surface Evolver numerical simulations and Bresme-Faraudo theory predictions for the critical angle ψ_{c2} decreases as the aspect ratio increases. Since Bresme-Faraudo theory suggests that this

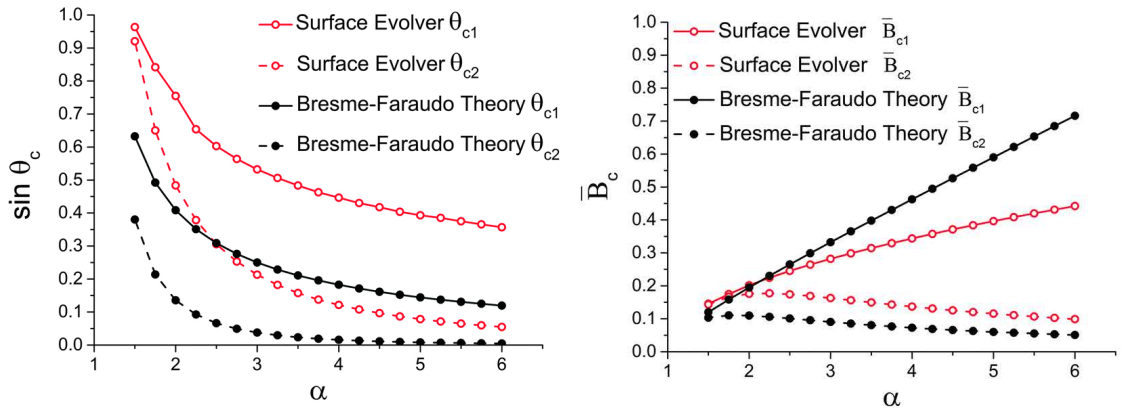

(A) (B)

FIGURE 5.11: (A) Dependence of the critical tilt angles ψ_{c1} and ψ_{c2} on the particle aspect ratio. Both critical tilt angles decrease with increasing aspect ratio. The second critical tilt angle $\psi_{c2} \to 0$ as $\alpha \to 6$ in Bresme-Faraudo theory, suggesting that the metastable state may disappear for large aspect ratios. (B) Dependence of the critical dipole-field strengths B_{c1} and B_{c2} on the particle aspect ratio. Bresme-Faraudo theory predicts a linear increase for the first critical dipole-field strength B_{c1} with increasing aspect ratio but Surface Evolver simulations show a sub-linear dependence. The second critical dipole-field strength B_{c2} initially increases as the aspect ratio increases until $\alpha = 2$ before it begins decreasing. The second critical dipole-field strength $B_{c2} \to 0$ again suggesting the disappearance of the metastable state. Reproduced from Ref [28] with permission of the PCCP Owner Societies.

G. B. Davies et al. Interface Deformations Affect the Orientation Transition of Magnetic Ellipsoidal Particles Adsorbed at Fluid-Fluid Interfaces, *Soft Matter*, 10, 6742-6748 (2014) [2]. Reproduced from Ref. [2] with permission from The Royal Society of Chemistry.

critical angle $\psi_{c2} \to 0$ as $\alpha \to 6$, this could indicate the disappearance of the metastable state and therefore hysteresis at large aspect ratios.

They also investigated the dependence of the critical dipole-field strengths as a function of the aspect-ratio, as shown in Figure 5.11b. Bresme-Faraudo theory predicts a linear increase in the first critical dipole-field strength B_{c1} as the aspect ratio increases, but Surface Evolver simulations show a sub-linear dependence. Interestingly, the second critical dipole-field strength B_{c2} increases until the aspect ratio reaches $\alpha = 2$ before decreasing in both Bresme-Faraudo theory and their numerical simulations. Again, the difference between the numerically measured second critical dipole-field strengths and the Bresme-Faraudo theory predictions decreases as the aspect ratio increases, and the second critical dipole-field strength appears to tend to zero $B_{c2} \to 0$ with increasing aspect ratio.

Finally, they studied the effect of particle wettability on the transition, for which no analytical theory currently exists. They found that as the contact angle moves further away from neutrally wetting $\theta = 90°$, both critical dipole-field strengths and critical tilt angles decrease.

5.4 Conclusions

In this Chapter, we investigated the response of a magnetic prolate spheroidal particle (with dipole moment aligned with its major axis) adsorbed at a fluid-fluid interface to an external magnetic field applied normal to the fluid-fluid interface.

The external field induces a torque that attempts to align the particle with the external field, but surface tension resists this rotation. Therefore the particle tilts with respect to the interface for a given dipole-field strength.

We found that when the dipole-field strength reaches a critical dipole-field strength, the particle discontinuously jumps from a tilted orientation to a vertical orientation i.e. undergoes a first-order phase transition, confirming previous theoretical predictions.

However, when we compared our numerical data with the theoretical predictions, we found large discrepancies: our simulations measured a higher tilt angle for a given

G. B. Davies et al. Interface Deformations Affect the Orientation Transition of Magnetic Ellipsoidal Particles Adsorbed at Fluid-Fluid Interfaces, *Soft Matter*, 10, 6742-6748 (2014) [2]. Reproduced from Ref. [2] with permission from The Royal Society of Chemistry.

dipole-field strength and therefore a smaller critical tilt angle, and a corresponding smaller critical dipole-field strength.

We showed that these differences are due to the theoretical assumption that the interface remains flat as the particle tilts. In reality, as we showed in our simulations, the interface deforms significantly. These deformations create more fluid-fluid interface area due to the additional interface curvature, which increases the free energy, but at the same time the particle removes more interface area than theoretically predicted due to contact line repositioning, which reduces the free energy. It is the interplay of these two effects that determines the equilibrium tilt angle.

Finally, we showed that during tilting the particle causes a dipolar deformation of the interface. Furthermore, the magnitude of these deformations can be controlled by varying tilt angle of the particle. Overlapping interface deformations lead to capillary interactions. Our results therefore allow the realisation of using dipolar capillary interactions to assemble particles at fluid-fluid interfaces, which has never been investigated before.

G. B. Davies et al. Interface Deformations Affect the Orientation Transition of Magnetic Ellipsoidal Particles Adsorbed at Fluid-Fluid Interfaces, *Soft Matter*, 10, 6742-6748 (2014) [2]. Reproduced from Ref. [2] with permission from The Royal Society of Chemistry.

Chapter 6

Assembling Ellipsoidal Particles at Fluid-Fluid Interfaces using Dipolar Capillary Interactions

6.1 Introduction

Our discovery that magnetic prolate spheroidal particles influenced by an external magnetic field deform the interface in a dipolar manner presents the intriguing possibility of creating novel particle arrangements at interfaces using our induced dipolar capillary interactions to control the assembly of particles at fluid-fluid interfaces, as described in Chapter 3. The assembly of particles in which dipolar capillary interactions are the dominant inter-particle interactions have never been investigated before.

6.2 Results

We investigated the behaviour of monolayers of neutrally wetting magnetic prolate spheroidal particles with aspect ratio $\alpha = 2.0$ adsorbed at a fluid-fluid interface influenced by an external magnetic field directed normal to the interface. We neglected magnetic dipole-dipole interactions between the particles to highlight the role played by capillary interactions.

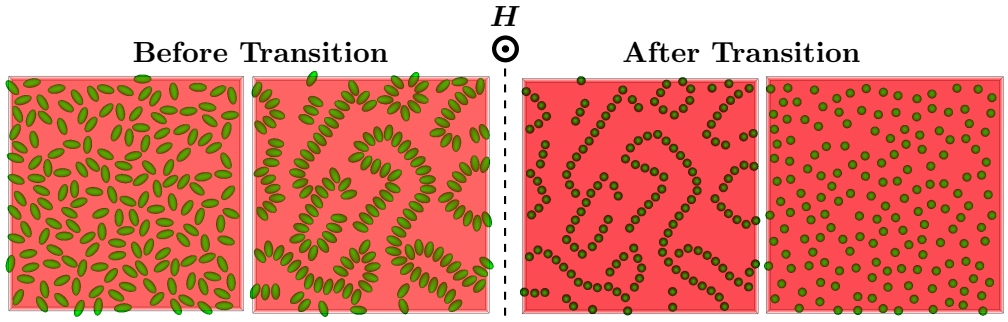

(A) $B = 0, t = 0$ (B) $B = \frac{1}{2}B_c, t \to \infty$ (C) $B > B_c, t = 0$ (D) $B > B_c, t \to \infty$

FIGURE 6.1: (A) The particles are distributed randomly in their equilibrium orientations with surface fraction $\phi = 0.38$. (B) Applying a magnetic field parallel to the interface normal, $\boldsymbol{H}$, causes them to self-assemble due to dipolar capillary interactions. (C) Once the critical field strength is reached, particles transition to the vertical state, halting dipolar capillary interactions. (D) Illustration: once capillary interactions have been turned off, the particles may order randomly if magnetic dipole-dipole and van der Waals interactions are weak compared to thermal fluctuations.

Figure 6.1 shows the phenomenology of the induced dipolar capillary interactions for a given surface packing fraction $\phi = NA_{rm}/A = 0.38$, where N is the number of particles, A_{rm} is area removed from the interface by a single particle in its equilibrium orientation, and A is the total fluid-fluid interface area. The particles begin randomly oriented at the interface with no external field applied (Figure 6.1a). In this orientation, the particles' align with their symmetry axis parallel to the interface and they do not deform the interface. We then apply an external field directed normal to the interface, which causes each particle to tilt with respect to the interface and deform the interface in a dipolar fashion (Figure 6.1b), as described in Chapter 3. The structures that form at the interface during this stage depend on the dipole-field strength, as shown in Figure 6.2, which we discuss shortly. We increase the field until we reach a critical dipole-field strength, B_c, at which the particles undergo a first order orientation phase transition into the vertical state. In this orientation, interface deformations, and therefore capillary interactions, are absent (as shown in Figure 5.8), halting the assembly of the particles (Figure 6.1c). Finally, once the particles transition into the vertical state and capillary interactions turn off due to the lack of interface deformations, the particles will order according to the balance of other interactions, such as thermal fluctuations, magnetic dipole-dipole forces, and van der Waals forces. Figure 6.1d is an illustration of a situation in which thermal fluctuations dominate and the particles arrange randomly on the interface.

Figure 6.2 shows that the particles arrange into different structures at the interface depending on the number of particles adsorbed at the interface and the dipole-field

G. B. Davies et al. Assembling Ellipsoidal Particles at Fluid Interfaces using Switchable Dipolar Capillary Interactions, *Advanced Materials*, 26: 6715-6719 (2014) [3].

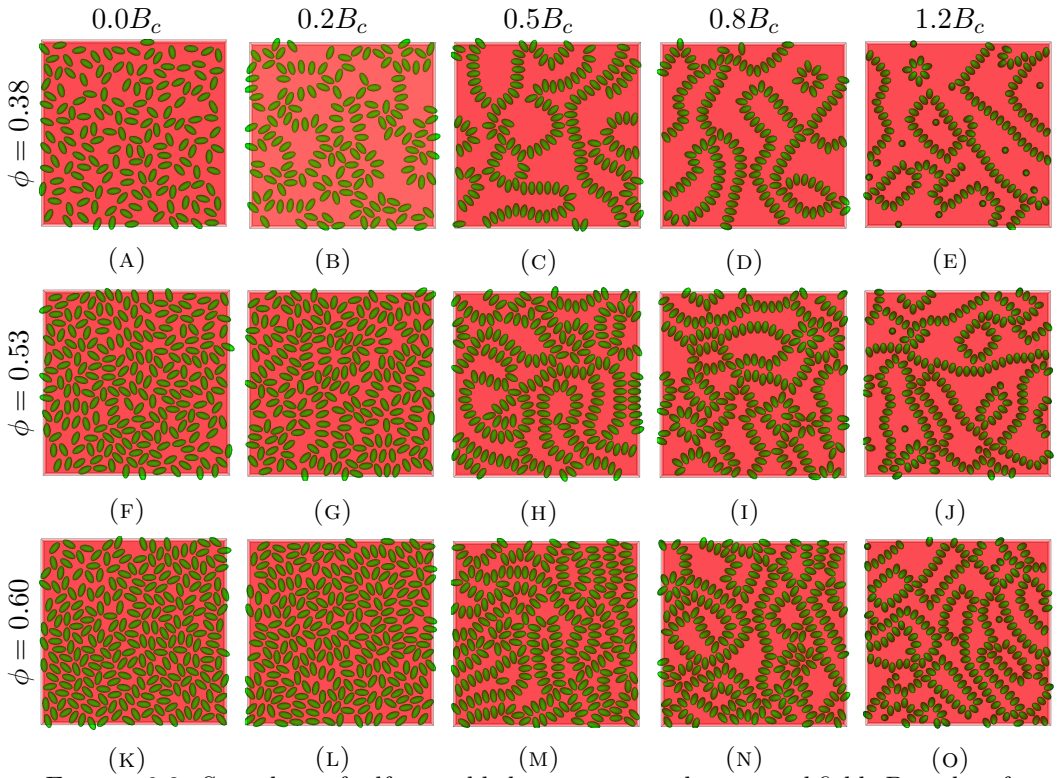

FIGURE 6.2: Snapshots of self-assembled structures as the external field, B, and surface fraction of particles, ϕ, is varied, showing a strong dependence on both parameters. At small applied fields, $B = 0.2B_c$, we see some particle ordering where particles prefer to be in a side-by-side or tip-to-tip state (B), (G), (L). For $B = 0.5B_c$ we observed the formation of curved "capillary caterpillars", in which the particles are oriented side-by-side and separate caterpillars prefer to face each other tip-to-tip (C), (H), (M). As the field strength is increased to $0.8B_c$, the caterpillars begin to prefer sharper, 90° corners instead of curved chains (D), (I), (N). We see a further increase in corner sharpness for field strengths of $B = 1.2B_c$, and some particles are in the vertical state for $\phi = 0.38$ (E). As the number of particles increases to $\phi = 0.53$ (J) and $\phi = 0.60$ (O), fewer flipped particles are observed.

strength. For low-dipole field strengths $B = 0.2B_c$, (B), (G), and (L), there is some ordering between particles but no distinctive structures. As we increase the dipole-field strength to $B = 0.5B_c$, (C), (H), (M), we see the formation of "capillary caterpillars" where particles within each chain organise side-by-side into curved chains. The particles between individual chains arrange in a tip—tip fashion, as shown in Figure 6.3. Our simulations therefore show interesting particle arrangements at the interface that have not been observed before. As the field strength increases further, $B = 0.8B_c$, (D), (I), (N), and $B = 1.2B_c$, (E), (J), (O), the chains become more rigid with right-angled corners.

For a dipole-field strength $B = 1.2B_c$ that exceeds the single-particle critical dipole-field strength, B_c, we expect the particles to have transitioned into the vertical state.

G. B. Davies et al. Assembling Ellipsoidal Particles at Fluid Interfaces using Switchable Dipolar Capillary Interactions, *Advanced Materials*, 26: 6715-6719 (2014) [3].

However, we find that only some particles transition into the vertical state for a packing fraction $\phi = 0.38$, (E), and as the packing fraction increases for a given dipole-field strength, (J), (O), fewer particles transition into the vertical state. This clearly indicates that many-body effects affect the phase transition.

6.3 Conclusions

Our work uncovers a new way of assembling particles at interfaces using induced dipolar capillary interactions. Compared with monopolar and quadrupolar capillary interactions that have been investigated before, as described in Chapter 2, induced dipolar capillary interactions offer much more control over the assembly process. For monopolar and quadrupolar interactions, particle properties such as particle weight, shape, and aspect-ratio, as well as interface properties, such as surface tension, determine the interactions: once the particles adsorb at the interface, one has little control over the assembly process.

In contrast, with the induced dipolar capillary interactions that we discovered, one has control over the dynamics of the interaction, the arrangement of the particles at the interface, and the existence of the capillary interactions altogether purely by changing the particle tilt angle, which is controlled by the external field. Our work therefore uncovers a new way of achieving reconfigurable structures at a fluid-fluid interface.

G. B. Davies et al. Assembling Ellipsoidal Particles at Fluid Interfaces using Switchable Dipolar Capillary Interactions, *Advanced Materials*, 26: 6715-6719 (2014) [3].

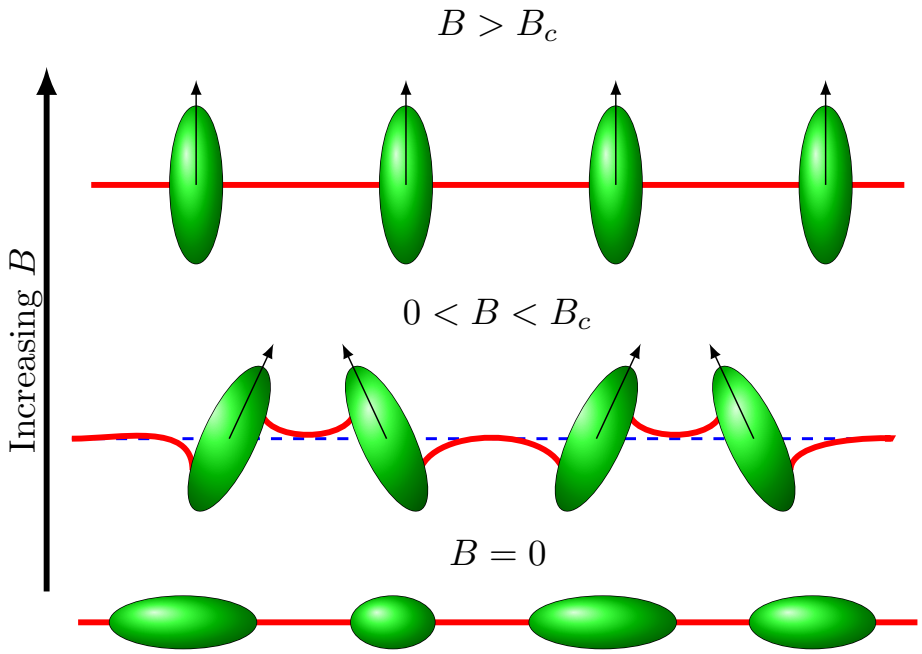

FIGURE 6.3: Bottom: Particles uninfluenced by an external field have a tilt angle $\psi = 0$ and do not deform the interface. Middle: Applying an external field normal to the interface causes the particles to tilt and deform the interface in a dipolar fashion, leading to particle—particle interactions. During tilting, the particles preferentially align in a side—side orientation in chains, but particles between chains prefer to align tip—tip, as shown here. Top: In the vertical state, the particles do not deform the interface and capillary interactions are absent once again.

Chapter 7

Conclusions

In this thesis, we presented a new analytical model describing the detachment energy of prolate and oblate spheroidal particles from fluid-fluid interfaces in Chapter 4. We found that both oblate and prolate spheroidal particles have higher detachment energies than spherical particles due to the increased fluid-fluid interface area they remove for a given particle volume. This suggests that spheroidal particles may be better stabilisers of particle-stabilised macro-emulsions than spherical particles. We verified the model using lattice Boltzmann simulations, finding good agreement. Our findings highlight the validity and utility of using the Shan-Chen lattice Boltzmann BGK model with immersed rigid particles for simulating particle-fluid-fluid mixtures.

We studied the behaviour of a magnetic prolate spheroidal particle, with its dipole moment aligned along the particle long axis, adsorbed at a fluid-fluid interface influenced by an external magnetic field directed normal to the interface in Chapter 5. The particle experiences a torque attempting to align its dipole moment with the external field, but surface tension resists this torque. Hence, for a given external field strength, the particle tilts with respect to the interface. We found that during tilting, the particle deforms the fluid-fluid interface in a dipolar fashion.

We then confirmed previous predictions that for a given dipole-field strength, the particle jumps from a tilted orientation to a vertical orientation aligned with the external field i.e. the particle undergoes a first-order phase transition. In the vertical orientation, the particle does not deform the interface. Therefore, capillary interactions arising from particle-induced interface deformations disappear in the vertical orientation. Since the

degree of particle tilt determines how much the particle deforms the interface, which affects the strength of the capillary interactions between two or more particles, the external field can be used to dynamically tune and control the strength of capillary interactions between particles.

In Chapter 6, we investigated the behaviour of many particles adsorbed at a fluid-fluid interface interacting via induced capillary interactions, finding that the structures that the particles form depends on the dipole-field strength applied. Small dipole-field strengths tend to produce curved chains, and larger dipole-field strengths tend to create rigid chains. In both cases, the particles prefer to orient side–by–side with each other in individual chains, but the particles in the chains prefer to orient tip–to–tip with particles in other chains. Our work opens up the possibility of using induced dipolar capillary interactions to manufacture novel, reconfigurable materials composed of colloidal particles.

Chapter 8

Future Direction

After our study of the detachment energy of spheroidal particles from flat fluid-fluid interfaces in Chapter 4, studying the detachment energy of anisotropic particles from curved droplets is an extremely interesting extension of this thesis, since little is known either experimentally or theoretically about how droplet curvature affects the detachment energy of anisotropic particles from curved fluid-fluid interfaces. Even a full understanding of spherical particles detaching from fluid-fluid interfaces is currently elusive. In particular, developing theoretical techniques in order to calculate the true work of detachment rather than just the free energy differences between various particle configurations should be a focus of future research.

A natural extension to the work carried out in this thesis in Chapter 5 and 6 is the experimental realisation of the induced capillary dipolar system. Once realised, it should be possible to investigate, for example, the rheological or optical properties of monolayers of ellipsoidal particles interacting via induced capillary dipoles, with potential implications for emulsion stability. Experimental particles have a range of aspect-ratios and sizes, allowing the possibility to investigate the formation of interesting structures analogous to the capillary-arrows discussed in Chapter 2. Further, experimental particles also have a range of contact angles, and it would be interesting to see whether monolayers of induced capillary dipoles change their preferred orientation from the side—side to the tip—tip state as has been previously observed in monolayers of quadrupolar ellipsoidal particles.

Having discovered a completely new way of assembling particles at interfaces, there are also still many unanswered questions based just on the work we have carried out so far. For example, how do thermal fluctuations, van der Waals forces, and magnetic dipole-dipole forces compete with capillary interactions, and what effect do they have on the structures that form as well as the phase transition? Why do particles preferentially align side–by–side and not tip–to–tip? Why do the particle chains become more rigid with increasing dipole-field strength? Answering these questions may provide further surprising insights into the behaviour of monolayers of ellipsoidal particles interacting via induced capillary dipolar interactions.

Appendix A

List of Publications

A.1 G. B. Davies, T. Krüger, P. V. Coveney, and J. Harting, Detachment Energies of Spheroidal Particles from Fluid-Fluid Interfaces, Journal of Chemical Physics, 141, 154902 (2014). Reproduced with permission from [1]. Copyright 2014, AIP Publishing LLC.

A.2 G. B. Davies, T. Krüger, P. V. Coveney, J. Harting and F. Bresme, Interface Deformations Affect the Orientation Transition of Magnetic Ellipsoidal Particles Adsorbed at Fluid-Fluid Interfaces, Soft Matter, 10, 6742-6748 (2014). Reproduced from Ref. [2] with permission from The Royal Society of Chemistry.

A.3 G. B. Davies, T. Krüger, P. V. Coveney, J. Harting, F. Bresme, Assembling Ellipsoidal Particles at Fluid Interfaces using Switchable Dipolar Capillary Interactions, Advanced Materials, 26, 6715-6719 (2014). Reproduced from Ref. [3] with permission.

Appendix B

Derivation of Interaction Energy between Polar Dipoles

In this Appendix, we show how to derive the far-field pair interaction potential between two polar capillary dipoles (Equation (5.4)). This derivation follows a similar derivation given in the thesis of Lewandowski [160], who shows how to derive Equation (2.24) from Stamou et al. [12].

The leading-order polar dipole term in the solution of Laplace's equation (Equation (2.19)) is:

$$\begin{aligned} h &= H\cos((\psi-\psi_0))\left(\frac{r_c}{r}\right) \\ \Rightarrow h_A &= H_A\cos((\psi-\psi_A))\left(\frac{r_c}{r_A}\right) \\ \Rightarrow h_B &= H_B\cos((\psi-\psi_B))\left(\frac{r_c}{r_B}\right) \end{aligned} \tag{B.1}$$

where r_c is the contact radius. Particle A is centred on a coordinate system (r_A, θ_A) and particle B is centred on a coordinate system (r_B, θ_B).

B.1 Coordinate Change

$$x_A = r_A \cos\theta_A \tag{B.2}$$

$$y_A = r_A \sin\theta_A \tag{B.3}$$

$$\theta_A = \tan^{-1}\frac{y_A}{x_A} \tag{B.4}$$

$$r_A^2 = y_A^2 + x_A^2 \tag{B.5}$$

B.2 Change Coordinates of h_A to Cartesians

$$\Rightarrow h_A = H_A r_c \cos((\tan^{-1}\left(\frac{y_A}{x_A}\right) - \psi_A))\frac{1}{\sqrt{y_A^2 + x_A^2}} \tag{B.6}$$

B.3 Write h_A in Terms of the B Coordinates

Note that $r_{AB} = x_A - x_B \Rightarrow x_A = r_{AB} + x_B$ and $y_B = y_A$

$$\Rightarrow h_A = H_A r_c \cos((\tan^{-1}\left(\frac{y_B}{r_{AB} + x_B}\right) - \psi_A))\frac{1}{\sqrt{y_A^2 + (r_{AB} + x_B)^2}} \tag{B.7}$$

B.4 Define Two Variables

Define $\beta = y_B^2 + (r_{AB} + x_B)^2$ and $\alpha = \tan^{-1}\left(\frac{y_B}{r_{AB}+x_B}\right) - \psi_A$

$\beta|_{0,0} = r_{AB}^2$

$\frac{\partial\beta}{\partial x_B} = 2(r_{AB} + x_B)$

$\frac{\partial\beta}{\partial y_B} = 2y_B$

$\alpha|_{0,0} = -\psi_A$

$\frac{\partial\alpha}{\partial x_B} = \frac{-y_b}{\beta}$

$\frac{\partial\alpha}{\partial y_B} = \frac{x_B + r_{AB}}{\beta}$

$$\Rightarrow h_A = H_A r_c \cos\alpha \ \beta^{-\frac{1}{2}} \tag{B.8}$$

B.5 First Dipole Derivatives

$$\begin{aligned}
\frac{\partial h_A}{x_B} =& H_a r_c \left[-\sin\alpha\beta^{-\frac{1}{2}} \frac{\partial\alpha}{\partial x_B} - \frac{1}{2}\beta^{-\frac{3}{2}} \cos\alpha \frac{\partial\beta}{\partial x_B} \right] \\
=& H_a r_c \left[y_B \sin\alpha\beta^{-\frac{3}{2}} - (r_{AB} + x_B)\beta^{-\frac{3}{2}} \cos\alpha \right] \qquad \text{(B.9)} \\
\frac{\partial h_A}{y_B} =& H_a r_c \left[-\sin\alpha\beta^{-\frac{1}{2}} \frac{\partial\alpha}{\partial y_B} - \frac{1}{2}\beta^{-\frac{3}{2}} \cos\alpha \frac{\partial\beta}{\partial y_B} \right] \\
=& H_a r_c \left[-\sin\alpha\beta^{-\frac{3}{2}} (x_B + r_{AB}) - y_B\beta^{-\frac{3}{2}} \cos\alpha \right] \qquad \text{(B.10)}
\end{aligned}$$

B.5.1 Evaluate First Derivatives at $(x_B = 0, y_B = 0)$

$$\frac{\partial h_A}{\partial x_B}|_{0,0} = - H_A r_c r_{AB}^{-2} \cos\psi_A \tag{B.11}$$

$$\frac{\partial h_A}{\partial y_B}|_{0,0} = H_A r_c r_{AB}^{-2} \sin\psi_A \tag{B.12}$$

B.6 Second Dipole Derivatives

$$\frac{\partial h_A}{\partial x_B} = H_A r_c \beta^{-\frac{3}{2}} \left[y_B \sin\alpha - (r_{AB} + x_B)\cos\alpha \right] \tag{B.13}$$

$$\begin{aligned}
\Rightarrow \frac{\partial^2 h_A}{\partial x_B^2} =& -\frac{3}{2} H_A r_c \beta^{-\frac{5}{2}} \frac{\partial\beta}{\partial x_B} \left[y_B \sin\alpha - (r_{AB} + x_B)\cos\alpha \right] \\
&+ H_A r_c \beta^{-\frac{3}{2}} \left[y_B \cos\alpha \frac{\partial\alpha}{\partial x_B} - \cos\alpha + (x_B + r_{AB}) \sin\alpha \frac{\partial\alpha}{\partial x_B} \right] \\
=& -3(r_{AB} + x_B) H_A r_c \beta^{-\frac{5}{2}} \left[y_B \sin\alpha - (r_{AB} + x_B)\cos\alpha \right] \\
&- H_A r_c \beta^{-\frac{3}{2}} \left[\cos\alpha \frac{y_B^2}{\beta} + \cos\alpha + (x_B + r_{AB}) \sin\alpha \frac{y_B}{\beta} \right] \qquad \text{(B.14)}
\end{aligned}$$

$$\frac{\partial h_A}{y_B} = - H_A r_c \beta^{-\frac{3}{2}} \left[\sin\alpha(x_B + r_{AB}) + y_B \cos\alpha\right] \tag{B.15}$$

$$\begin{aligned}\Rightarrow \frac{\partial^2 h_A}{\partial y_B^2} =& \frac{3}{2} H_A r_c \beta^{-\frac{5}{2}} \frac{\partial \beta}{\partial y_B} \left[(x_B + r_{AB})\sin\alpha + y_B\cos\alpha\right] \\ & - H_A r_c \beta^{-\frac{3}{2}} \left[(x_B + r_{AB})\cos\alpha \frac{\partial \alpha}{\partial y_B} + \cos\alpha - y_B \sin\alpha \frac{\partial \alpha}{\partial y_B}\right] \\ =& 3 y_B H_A r_c \beta^{-\frac{5}{2}} \left[(x_B + r_{AB})\sin\alpha + y_B\cos\alpha\right] \\ & - H_A r_c \beta^{-\frac{3}{2}} \left[\cos\alpha \frac{(x_B + r_{AB})^2}{\beta} + \cos\alpha - y_B \sin\alpha \frac{x_B + r_{AB}}{\beta}\right]\end{aligned} \tag{B.16}$$

B.6.1 Evaluate Second Derivatives at $(x_B = 0, y_B = 0)$

$$\begin{aligned}\frac{\partial^2 h_A}{\partial x_B^2}|_{0,0} =& -3(r_{AB} + x_B) H_A r_c \beta|_{0,0}^{-\frac{5}{2}} \left[y_B \sin\alpha|_{0,0} - (r_{AB} + x_B)\cos\alpha|_{0,0}\right] \\ & - H_A r_c \beta|_{0,0}^{-\frac{3}{2}} \left[\cos\alpha|_{0,0} \frac{y_B^2}{\beta|_{0,0}} + \cos\alpha|_{0,0} + (x_B + r_{AB})\sin\alpha|_{0,0} \frac{y_B}{\beta|_{0,0}}\right] \\ =& 3 H_A r_c r_{AB}^{-3} \cos\psi_A - H_A r_c r_{AB}^{-3} \cos\psi_A = 2 H_A r_c r_{AB}^{-3} \cos\psi_A\end{aligned} \tag{B.17}$$

$$\begin{aligned}\frac{\partial^2 h_A}{\partial y_B^2}|_{0,0} =& \; 3 y_B H_A r_c \beta|_{0,0}^{-\frac{5}{2}} \left[(x_B + r_{AB})\sin\alpha|_{0,0} + y_B \cos\alpha|_{0,0}\right] \\ & - H_A r_c \beta|_{0,0}^{-\frac{3}{2}} \left[\cos\alpha|_{0,0} \frac{(x_B + r_{AB})^2}{\beta|_{0,0}} + \cos\alpha|_{0,0} - y_B \sin\alpha|_{0,0} \frac{x_B + r_{AB}}{\beta|_{0,0}}\right] \\ =& -2 H_A r_c r_{AB}^{-3} \cos\psi_A\end{aligned} \tag{B.18}$$

B.6.2 Mixed Derivative

$$\frac{\partial h_A}{\partial x_B} = H_A r_c \beta^{-\frac{3}{2}} \left[y_B \sin\alpha - (r_{AB} + x_B)\cos\alpha\right] \tag{B.19}$$

$$\begin{aligned}\Rightarrow \frac{\partial^2 h_A}{\partial y_B \partial x_B} =& -\frac{3}{2} H_A r_c \beta^{-\frac{5}{2}} \frac{\partial \beta}{\partial y_B} \left[y_B \sin\alpha - (r_{AB} + x_B)\cos\alpha\right] \\ & + H_A r_c \beta^{-\frac{3}{2}} \left[\sin\alpha + y_B \cos\alpha \frac{\partial \alpha}{\partial y_B} + \frac{\partial \alpha}{\partial y_B}(r_{AB} + x_B)\sin\alpha\right] \\ =& -3 y_B H_A r_c \beta^{-\frac{5}{2}} \left[y_B \sin\alpha - (r_{AB} + x_B)\cos\alpha\right] \\ & + H_A r_c \beta^{-\frac{3}{2}} \left[\sin\alpha + y_B \cos\alpha \frac{x_B + r_{AB}}{\beta} + \frac{(x_B + r_{AB})^2}{\beta}\sin\alpha\right]\end{aligned} \tag{B.20}$$

B.6.3 Evaluate Mixed Derivatives at $(x_B = 0, y_B = 0)$

$$\begin{aligned}\Rightarrow \frac{\partial^2 h_A}{\partial y_B \partial x_B}|_{0,0} =& -3 y_B H_A r_c \beta|_{0,0}^{-\frac{5}{2}} \left[y_B \sin\alpha|_{0,0} - (r_{AB} + x_B)\cos\alpha|_{0,0} \right] \\ &+ H_A r_c \beta|_{0,0}^{-\frac{3}{2}} \left[\sin\alpha|_{0,0} + y_B \cos\alpha|_{0,0} \frac{x_B + r_{AB}}{\beta|_{0,0}} + \frac{(x_B + r_{AB})^2}{\beta|_{0,0}} \sin\alpha|_{0,0} \right] \\ =& -2 H_A r_c r_{AB}^{-3} \sin\psi_A \end{aligned} \tag{B.21}$$

B.7 Tensor Product of Gradients in Cartesian Coordinates

$$\begin{aligned}(\nabla \otimes \nabla) h|_{0,0} &= \begin{pmatrix} \frac{\partial^2}{\partial x^2} & \frac{\partial^2}{\partial x \partial y} \\ \frac{\partial^2}{\partial y \partial x} & \frac{\partial^2}{\partial y^2} \end{pmatrix} h|_{0,0} \\ &= \begin{pmatrix} 2 H_A r_c r_{AB}^{-3} \cos\psi_A & -2 H_A r_c r_{AB}^{-3} \sin\psi_A \\ -2 H_A r_c r_{AB}^{-3} \sin\psi_A & -2 H_A r_c r_{AB}^{-3} \cos\psi_A \end{pmatrix} \end{aligned} \tag{B.22}$$

B.8 Dot Product with Tensor Product

$$\begin{aligned}\mathbf{r} \cdot (\nabla \otimes \nabla) h|_{0,0} =& (r_B \cos\theta_B, r_B \sin\theta_B) \cdot \begin{pmatrix} 2 H_A r_c r_{AB}^{-3} \cos\psi_A & -2 H_A r_c r_{AB}^{-3} \sin\psi_A \\ -2 H_A r_c r_{AB}^{-3} \sin\psi_A & -2 H_A r_c r_{AB}^{-3} \cos\psi_A \end{pmatrix} \\ =& \begin{pmatrix} 2 r_B H_A r_c r_{AB}^{-3} \cos\psi_A \cos\theta_B - 2 r_B H_A r_c r_{AB}^{-3} \sin\psi_A \sin\theta_B \\ -2 r_B H_A r_c r_{AB}^{-3} \sin\psi_A \cos\theta_B - 2 r_B H_A r_c r_{AB}^{-3} \cos\psi_A \sin\theta_B \end{pmatrix} \\ =& 2 r_B H_A r_c r_{AB}^{-3} \begin{pmatrix} \cos\psi_A \cos\theta_B - \sin\psi_A \sin\theta_B \\ -\sin\psi_A \cos\theta_B - \cos\psi_A \sin\theta_B \end{pmatrix} \\ =& 2 H_A r_c^2 r_{AB}^{-3} \begin{pmatrix} \cos(\theta_B + \psi_A) \\ -\sin(\theta_B + \psi_A) \end{pmatrix} \end{aligned} \tag{B.23}$$

Using $r_B = r_c$.

B.9 Gradient Term

$$= H_A r_c r_{AB}^{-2} \begin{pmatrix} -\cos\psi_A \\ \sin\psi_A \end{pmatrix} \tag{B.24}$$

B.10 Full Matrix

$$\begin{aligned} =& 2H_A r_c^2 r_{AB}^{-3} \begin{pmatrix} \cos(\theta_B + \psi_A) \\ -\sin(\theta_B + \psi_A) \end{pmatrix} + H_A r_c r_{AB}^{-2} \begin{pmatrix} -\cos\psi_A \\ \sin\psi_A \end{pmatrix} \\ =& H_A r_c \begin{pmatrix} 2r_c \cos(\theta_B + \psi_A) r_{AB}^{-3} - r_{AB}^{-2} \cos\psi_A \\ -2r_c \sin(\theta_B + \psi_A) r_{AB}^{-3} + r_{AB}^{-2} \sin\psi_A \end{pmatrix} \end{aligned} \tag{B.25}$$

B.11 Calculate Integral

$$\begin{aligned} &\int_{C_B} h_B(\mathbf{n} \cdot \nabla h_A) = H_A r_c^2 \int_0^{2\pi} \begin{pmatrix} -\cos\theta_B \\ -\sin\theta_B \end{pmatrix} \begin{pmatrix} 2r_c \cos(\theta_B + \psi_A) r_{AB}^{-3} - r_{AB}^{-2} \cos\psi_A \\ -2r_c \sin(\theta_B + \psi_A) r_{AB}^{-3} + r_{AB}^{-2} \sin\psi_A \end{pmatrix} \\ &\times H_B \cos(\theta_B - \psi_B)\, d\theta_B \\ &= 2H_A H_B r_c^3 r_{AB}^{-3} \int_0^{2\pi} (-\cos\theta_B \cos(\theta_B + \psi_A) + \sin\theta_B \sin(\theta_B + \psi_A)) \times \cos(\theta_B - \psi_B)\, d\theta_B \\ &+ H_A H_B r_c^2 r_{AB}^{-2} \int_0^{2\pi} (\cos\theta_B \cos\psi_A - \sin\psi_A \sin\theta_B) \times \cos(\theta_B - \psi_B)\, d\theta_B \\ &= 2H_A H_B r_c^3 r_{AB}^{-3} \int_0^{2\pi} -\cos(2\theta_B + \psi_A) \cos(\theta_B - \psi_B)\, d\theta_B \\ &+ H_A H_B r_c^2 r_{AB}^{-2} \int_0^{2\pi} \cos(\theta_B + \psi_A) \cos(\theta_B - \psi_B)\, d\theta_B \\ &= \pi H_A H_B r_c^2 r_{AB}^{-2} \cos(\psi_A + \psi_B) \end{aligned} \tag{B.26}$$

Bibliography

[1] Davies, G. B., Krüger, T., Coveney, P. V., and Harting, J. Detachment energies of spheroidal particles from fluid-fluid interfaces. *The Journal of Chemical Physics*, 141(15):154902, October 2014. ISSN 0021-9606, 1089-7690. doi: 10.1063/1.4898071. URL http://scitation.aip.org/content/aip/journal/jcp/141/15/10.1063/1.4898071.

[2] Davies, G. B., Krüger, T., Coveney, P. V., Harting, J., and Bresme, F. Interface deformations affect the orientation transition of magnetic ellipsoidal particles adsorbed at fluid–fluid interfaces. *Soft Matter*, 10(35):6742–6748, August 2014. ISSN 1744-6848. doi: 10.1039/C4SM01124D. URL http://pubs.rsc.org/en/content/articlelanding/2014/sm/c4sm01124d.

[3] Davies, G. B., Krüger, T., Coveney, P. V., Harting, J., and Bresme, F. Assembling Ellipsoidal Particles at Fluid Interfaces Using Switchable Dipolar Capillary Interactions. *Adv. Mater.*, 26(39):6715–6719, October 2014. ISSN 1521-4095. doi: 10.1002/adma.201402419. URL http://onlinelibrary.wiley.com/doi/10.1002/adma.201402419/abstract.

[4] Jansen, F. and Harting, J. From bijels to Pickering emulsions: A lattice Boltzmann study. *Phys. Rev. E*, 83(4):046707, April 2011. doi: 10.1103/PhysRevE.83.046707. URL http://link.aps.org/doi/10.1103/PhysRevE.83.046707.

[5] Weon, B. M., Lee, J. S., Kim, J. T., Pyo, J., and Je, J. H. Colloidal wettability probed with X-ray microscopy. *Current Opinion in Colloid & Interface Science*, 17(6):388–395, December 2012. ISSN 1359-0294. doi: 10.1016/j.cocis.2012.08.002. URL http://www.sciencedirect.com/science/article/pii/S1359029412000969.

[6] Kralchevsky, P. A., Ivanov, I. B., Ananthapadmanabhan, K. P., and Lips, A. On the Thermodynamics of Particle-Stabilized Emulsions: Curvature Effects and Catastrophic Phase Inversion. *Langmuir*, 21(1):50–63, January 2005. ISSN 0743-7463. doi: 10.1021/la047793d. URL http://dx.doi.org/10.1021/la047793d.

[7] Dinsmore, A. D., Hsu, M. F., Nikolaides, M. G., Marquez, M., Bausch, A. R., and Weitz, D. A. Colloidosomes: Selectively Permeable Capsules Composed of Colloidal Particles. *Science*, 298(5595):1006–1009, November 2002. ISSN 0036-8075, 1095-9203. doi: 10.1126/science.1074868. URL http://www.sciencemag.org/content/298/5595/1006.

[8] Manoharan, V. N., Elsesser, M. T., and Pine, D. J. Dense Packing and Symmetry in Small Clusters of Microspheres. *Science*, 301(5632):483–487, July 2003. ISSN 0036-8075, 1095-9203. doi: 10.1126/science.1086189. URL http://www.sciencemag.org/content/301/5632/483.

[9] Wang, Y., Wang, Y., Breed, D. R., Manoharan, V. N., Feng, L., Hollingsworth, A. D., Weck, M., and Pine, D. J. Colloids with valence and specific directional bonding. *Nature*, 491(7422):51–55, November 2012. ISSN 0028-0836. doi: 10.1038/nature11564. URL http://www.nature.com.libproxy.ucl.ac.uk/nature/journal/v491/n7422/full/nature11564.html.

[10] Herzig, E. M., White, K. A., Schofield, A. B., Poon, W. C. K., and Clegg, P. S. Bicontinuous emulsions stabilized solely by colloidal particles. *Nature Materials*, 6(12):966–971, 2007. ISSN 1476-1122. doi: 10.1038/nmat2055. URL http://www.nature.com.libproxy.ucl.ac.uk/nmat/journal/v6/n12/full/nmat2055.html.

[11] Butt, H.-J. Controlling the Flow of Suspensions. *Science*, 331(6019):868–869, February 2011. ISSN 0036-8075, 1095-9203. doi: 10.1126/science.1201543. URL http://www.sciencemag.org/content/331/6019/868.

[12] Stamou, D., Duschl, C., and Johannsmann, D. Long-range attraction between colloidal spheres at the air-water interface: The consequence of an irregular meniscus. *Phys. Rev. E*, 62(4):5263–5272, October 2000. doi: 10.1103/PhysRevE.62.5263. URL http://link.aps.org/doi/10.1103/PhysRevE.62.5263.

[13] Fournier, J.-B. and Galatola, P. Anisotropic capillary interactions and jamming of colloidal particles trapped at a liquid-fluid interface. *Phys. Rev. E*, 65(3):031601, February 2002. doi: 10.1103/PhysRevE.65.031601. URL http://link.aps.org/doi/10.1103/PhysRevE.65.031601.

[14] Brown, A. B. D., Smith, C. G., and Rennie, A. R. Fabricating colloidal particles with photolithography and their interactions at an air-water interface. *Phys. Rev. E*, 62(1):951–960, July 2000. doi: 10.1103/PhysRevE.62.951. URL http://link.aps.org/doi/10.1103/PhysRevE.62.951.

[15] Loudet, J. C., Alsayed, A. M., Zhang, J., and Yodh, A. G. Capillary Interactions Between Anisotropic Colloidal Particles. *Phys. Rev. Lett.*, 94(1):018301, January 2005. doi: 10.1103/PhysRevLett.94.018301. URL http://link.aps.org/doi/10.1103/PhysRevLett.94.018301.

[16] Loudet, J. C. and Pouligny, B. Self-assembled capillary arrows. *EPL*, 85(2): 28003, January 2009. ISSN 0295-5075. doi: 10.1209/0295-5075/85/28003. URL http://iopscience.iop.org/0295-5075/85/2/28003.

[17] Loudet, J. C. and Pouligny, B. How do mosquito eggs self-assemble on the water surface? *Eur. Phys. J. E*, 34(8):1–17, August 2011. ISSN 1292-8941, 1292-895X. doi: 10.1140/epje/i2011-11076-9. URL http://link.springer.com/article/10.1140/epje/i2011-11076-9.

[18] Lewandowski, E. P., Cavallaro, M., Botto, L., Bernate, J. C., Garbin, V., and Stebe, K. J. Orientation and Self-Assembly of Cylindrical Particles by Anisotropic Capillary Interactions. *Langmuir*, 26(19):15142–15154, October 2010. ISSN 0743-7463. doi: 10.1021/la1012632. URL http://dx.doi.org/10.1021/la1012632.

[19] Botto, L., Lewandowski, E. P., Cavallaro, M., and Stebe, K. J. Capillary interactions between anisotropic particles. *Soft Matter*, 8(39):9957–9971, September 2012. ISSN 1744-6848. doi: 10.1039/C2SM25929J. URL http://pubs.rsc.org/en/content/articlelanding/2012/sm/c2sm25929j.

[20] Yunker, P. J., Durian, D. J., and Yodh, A. G. Coffee rings and coffee disks: Physics on the edge. *Physics Today*, 66(8):60–61, July 2013. ISSN 0031-9228, 1945-0699. doi: 10.1063/PT.3.2093. URL http://scitation.aip.org.libproxy.ucl.ac.uk/content/aip/magazine/physicstoday/article/66/8/10.1063/PT.3.2093.

[21] Hu, D. L. and Bush, J. W. M. Meniscus-climbing insects. *Nature*, 437(7059):733–736, September 2005. ISSN 0028-0836. doi: 10.1038/nature03995. URL http://www.nature.com/nature/journal/v437/n7059/abs/nature03995.html.

[22] O'Brien, S. B. G. The Meniscus near a Small Sphere and Its Relationship to Line Pinning of Contact Lines. *Journal of Colloid and Interface Science*, 183 (1):51–56, October 1996. ISSN 0021-9797. doi: 10.1006/jcis.1996.0517. URL http://www.sciencedirect.com/science/article/pii/S0021979796905172.

[23] de Gennes, P. G. Wetting: statics and dynamics. *Rev. Mod. Phys.*, 57(3):827–863, July 1985. doi: 10.1103/RevModPhys.57.827. URL http://link.aps.org/doi/10.1103/RevModPhys.57.827.

[24] Joanny, J. F. and de Gennes, P. G. A model for contact angle hysteresis. *The Journal of Chemical Physics*, 81(1):552–562, July 1984. ISSN 0021-9606, 1089-7690. doi: 10.1063/1.447337. URL http://scitation.aip.org.libproxy.ucl.ac.uk/content/aip/journal/jcp/81/1/10.1063/1.447337.

[25] Chateau, X. and Pitois, O. Quasistatic detachment of a sphere from a liquid interface. *Journal of Colloid and Interface Science*, 259(2):346–353, March 2003. ISSN 0021-9797. doi: 10.1016/S0021-9797(02)00219-9. URL http://www.sciencedirect.com/science/article/pii/S0021979702002199.

[26] Pitois, O. and Chateau, X. Small Particle at a Fluid Interface: Effect of Contact Angle Hysteresis on Force and Work of Detachment. *Langmuir*, 18(25):9751–9756, December 2002. ISSN 0743-7463. doi: 10.1021/la020300p. URL http://dx.doi.org/10.1021/la020300p.

[27] Bresme, F. and Faraudo, J. Orientational transitions of anisotropic nanoparticles at liquid–liquid interfaces. *J. Phys.: Condens. Matter*, 19(37):375110, September 2007. ISSN 0953-8984. doi: 10.1088/0953-8984/19/37/375110. URL http://iopscience.iop.org/0953-8984/19/37/375110.

[28] Newton, B. J., Brakke, K. A., and Buzza, D. M. A. Influence of magnetic field on the orientation of anisotropic magnetic particles at liquid interfaces. *Phys. Chem. Chem. Phys.*, October 2014. ISSN 1463-9084. doi: 10.1039/C4CP04270K. URL http://pubs.rsc.org/en/content/articlelanding/2014/cp/c4cp04270k.

[29] Scriven, L. E. Equilibrium bicontinuous structure. *Nature*, 263(5573):123–125, September 1976. doi: 10.1038/263123a0. URL http://www.nature.com.libproxy.ucl.ac.uk/nature/journal/v263/n5573/abs/263123a0.html.

[30] Langevin, D. Micelles and Microemulsions. *Annual Review of Physical Chemistry*, 43(1):341–369, 1992. doi: 10.1146/annurev.pc.43.100192.002013. URL http://dx.doi.org/10.1146/annurev.pc.43.100192.002013.

[31] Ramsden, W. Separation of Solids in the Surface-Layers of Solutions and 'Suspensions' (Observations on Surface-Membranes, Bubbles, Emulsions, and Mechanical Coagulation). – Preliminary Account. *Proc. R. Soc. Lond.*, 72(477-486): 156–164, January 1903. ISSN 0370-1662,. doi: 10.1098/rspl.1903.0034. URL http://rspl.royalsocietypublishing.org/content/72/477-486/156.

[32] Pickering, S. U. CXCVI.—Emulsions. *J. Chem. Soc., Trans.*, 91(0):2001–2021, January 1907. ISSN 0368-1645. doi: 10.1039/CT9079102001. URL http://pubs.rsc.org/en/content/articlelanding/1907/ct/ct9079102001.

[33] Aveyard, R., Binks, B. P., and Clint, J. H. Emulsions stabilised solely by colloidal particles. *Advances in Colloid and Interface Science*, 100–102:503–546, February 2003. ISSN 0001-8686. doi: 10.1016/S0001-8686(02)00069-6. URL http://www.sciencedirect.com/science/article/pii/S0001868602000696.

[34] Sacanna, S., Kegel, W. K., and Philipse, A. P. Thermodynamically Stable Pickering Emulsions. *Phys. Rev. Lett.*, 98(15):158301, April 2007. doi: 10.1103/PhysRevLett.98.158301. URL http://link.aps.org/doi/10.1103/PhysRevLett.98.158301.

[35] Kraft, D. J., de Folter, J. W. J., Luigjes, B., Castillo, S. I. R., Sacanna, S., Philipse, A. P., and Kegel, W. K. Conditions for Equilibrium Solid-Stabilized Emulsions. *J. Phys. Chem. B*, 114(32):10347–10356, August 2010. ISSN 1520-6106. doi: 10.1021/jp102659b. URL http://dx.doi.org/10.1021/jp102659b.

[36] Aveyard, R., Clint, J. H., and Horozov, T. S. Aspects of the stabilisation of emulsions by solid particles: Effects of line tension and monolayer curvature energy. *Phys. Chem. Chem. Phys.*, 5(11):2398–2409, May 2003. ISSN 1463-9084. doi: 10.1039/B210687F. URL http://pubs.rsc.org/en/content/articlelanding/2003/cp/b210687f.

[37] Binks, B. P. and Lumsdon, S. O. Influence of Particle Wettability on the Type and Stability of Surfactant-Free Emulsions†. *Langmuir*, 16(23):8622–8631, November 2000. ISSN 0743-7463. doi: 10.1021/la000189s. URL http://dx.doi.org/10.1021/la000189s.

[38] Binks, B. P. and Lumsdon, S. O. Transitional Phase Inversion of Solid-Stabilized Emulsions Using Particle Mixtures. *Langmuir*, 16(8):3748–3756, April 2000. ISSN 0743-7463. doi: 10.1021/la991427q. URL http://dx.doi.org/10.1021/la991427q.

[39] Binks, B. P. and Lumsdon, S. O. Catastrophic Phase Inversion of Water-in-Oil Emulsions Stabilized by Hydrophobic Silica. *Langmuir*, 16(6):2539–2547, March 2000. ISSN 0743-7463. doi: 10.1021/la991081j. URL http://dx.doi.org/10.1021/la991081j.

[40] Binks, B. P. and Lumsdon, S. O. Effects of oil type and aqueous phase composition on oil–water mixtures containing particles of intermediate hydrophobicity. *Phys. Chem. Chem. Phys.*, 2(13):2959–2967, January 2000. ISSN 1463-9084. doi: 10.1039/B002582H. URL http://pubs.rsc.org/en/content/articlelanding/2000/cp/b002582h.

[41] Binks, B. P. and Horozov, T. S. *Colloidal Particles at Liquid Interfaces*. Cambridge University Press, August 2006. ISBN 9781139458184.

[42] Levine, S., Bowen, B. D., and Partridge, S. J. Stabilization of emulsions by fine particles I. Partitioning of particles between continuous phase and oil/water interface. *Colloids and Surfaces*, 38(2):325–343, 1989. ISSN 0166-6622. doi: 10.1016/0166-6622(89)80271-9. URL http://www.sciencedirect.com/science/article/pii/0166662289802719.

[43] Tambe, D. E. and Sharma, M. M. Factors Controlling the Stability of Colloid-Stabilized Emulsions: I. An Experimental Investigation. *Journal of Colloid and Interface Science*, 157(1):244–253, April 1993. ISSN 0021-9797. doi: 10.1006/jcis.1993.1182. URL http://www.sciencedirect.com/science/article/pii/S0021979783711823.

[44] Ivanov, I. B., Radoev, B., Manev, E., and Scheludko, A. Theory of the critical thickness of rupture of thin liquid films. *Trans. Faraday Soc.*, 66(0):1262–1273,

January 1970. ISSN 0014-7672. doi: 10.1039/TF9706601262. URL http://pubs.rsc.org/en/content/articlelanding/1970/tf/tf9706601262.

[45] Kaptay, G. On the equation of the maximum capillary pressure induced by solid particles to stabilize emulsions and foams and on the emulsion stability diagrams. *Colloids and Surfaces A: Physicochemical and Engineering Aspects*, 282–283:387–401, July 2006. ISSN 0927-7757. doi: 10.1016/j.colsurfa.2005.12.021. URL http://www.sciencedirect.com/science/article/pii/S0927775705009775.

[46] Kruglyakov, P. M., Nushtayeva, A. V., and Vilkova, N. G. Experimental investigation of capillary pressure influence on breaking of emulsions stabilized by solid particles. *Journal of Colloid and Interface Science*, 276(2):465–474, August 2004. ISSN 0021-9797. doi: 10.1016/j.jcis.2004.03.059. URL http://www.sciencedirect.com/science/article/pii/S002197970400339X.

[47] Nushtaeva, A. V. and Kruglyakov, P. M. Capillary Pressure in Thinning Emulsion Film Stabilized with Solid Spherical Particles. *Colloid Journal*, 65(3):341–349, May 2003. ISSN 1061-933X, 1608-3067. doi: 10.1023/A:1024262924419. URL http://link.springer.com/article/10.1023/A%3A1024262924419.

[48] Denkov, N. D., Ivanov, I. B., Kralchevsky, P. A., and Wasan, D. T. A possible mechanism of stabilization of emulsions by solid particles. *Journal of Colloid and Interface Science*, 150(2):589–593, May 1992. ISSN 0021-9797. doi: 10.1016/0021-9797(92)90228-E. URL http://www.sciencedirect.com/science/article/pii/002197979290228E.

[49] Tcholakova, S., Denkov, N. D., and Lips, A. Comparison of solid particles, globular proteins and surfactants as emulsifiers. *Phys. Chem. Chem. Phys.*, 10(12):1608–1627, March 2008. ISSN 1463-9084. doi: 10.1039/B715933C. URL http://pubs.rsc.org/en/content/articlelanding/2008/cp/b715933c.

[50] Fan, H. and Striolo, A. Mechanistic study of droplets coalescence in Pickering emulsions. *Soft Matter*, 8(37):9533–9538, August 2012. ISSN 1744-6848. doi: 10.1039/C2SM26416A. URL http://pubs.rsc.org/en/content/articlelanding/2012/sm/c2sm26416a.

[51] Tambe, D. E. and Sharma, M. M. The effect of colloidal particles on fluid-fluid interfacial properties and emulsion stability. *Advances in Colloid*

and Interface Science, 52:1–63, September 1994. ISSN 0001-8686. doi: 10.1016/0001-8686(94)80039-1. URL http://www.sciencedirect.com/science/article/pii/0001868694800391.

[52] Tambe, D. E. and Sharma, M. M. Factors Controlling the Stability of Colloid-Stabilized Emulsions: II. A Model for the Rheological Properties of Colloid-Laden Interfaces. *Journal of Colloid and Interface Science*, 162(1):1–10, January 1994. ISSN 0021-9797. doi: 10.1006/jcis.1994.1001. URL http://www.sciencedirect.com/science/article/pii/S0021979784710010.

[53] Ostwald, W., Bodenstein, M., Clusius, K., Bonhoeffer, K. F., and Falkenhagen, H. *Zeitschrift für physikalische Chemie*. Akademische Verlagsgesellschaft Geest & Portig, 1897.

[54] Lifshitz, I. M. and Slyozov, V. V. The kinetics of precipitation from supersaturated solid solutions. *Journal of Physics and Chemistry of Solids*, 19(1–2):35–50, April 1961. ISSN 0022-3697. doi: 10.1016/0022-3697(61)90054-3. URL http://www.sciencedirect.com/science/article/pii/0022369761900543.

[55] Wagner, C. Theorie der Alterung von Niederschlägen durch Umlösen (Ostwald-Reifung). *Zeitschrift für Elektrochemie, Berichte der Bunsengesellschaft für physikalische Chemie*, 65(7-8):581–591, September 1961. ISSN 0005-9021. doi: 10.1002/bbpc.19610650704. URL http://onlinelibrary.wiley.com/doi/10.1002/bbpc.19610650704/abstract.

[56] Robins, M. M. Emulsions — creaming phenomena. *Current Opinion in Colloid & Interface Science*, 5(5–6):265–272, November 2000. ISSN 1359-0294. doi: 10.1016/S1359-0294(00)00065-0. URL http://www.sciencedirect.com/science/article/pii/S1359029400000650.

[57] Shields, M., Ellis, R., and Saunders, B. R. A creaming study of weakly flocculated and depletion flocculated oil-in-water emulsions. *Colloids and Surfaces A: Physicochemical and Engineering Aspects*, 178(1–3):265–276, March 2001. ISSN 0927-7757. doi: 10.1016/S0927-7757(00)00715-9. URL http://www.sciencedirect.com/science/article/pii/S0927775700007159.

[58] Herk, A. M. v. *Chemistry and Technology of Emulsion Polymerisation*. Wiley, October 2005. ISBN 9781405121132.

[59] Bowick, M. J., Nelson, D. R., and Travesset, A. Interacting topological defects on frozen topographies. *Phys. Rev. B*, 62(13):8738–8751, October 2000. doi: 10.1103/PhysRevB.62.8738. URL http://link.aps.org/doi/10.1103/PhysRevB.62.8738.

[60] Umbanhowar, P. B., Prasad, V., and Weitz, D. A. Monodisperse Emulsion Generation via Drop Break Off in a Coflowing Stream. *Langmuir*, 16(2):347–351, January 2000. ISSN 0743-7463. doi: 10.1021/la990101e. URL http://dx.doi.org/10.1021/la990101e.

[61] Sloane, N. J. A., Hardin, R. H., Duff, T. D. S., and Conway, J. H. Minimal-energy clusters of hard spheres. *Discrete & Computational Geometry*, 14(1):237–259, December 1995. ISSN 0179-5376, 1432-0444. doi: 10.1007/BF02570704. URL http://link.springer.com/article/10.1007/BF02570704.

[62] Lauga, E. and Brenner, M. P. Evaporation-Driven Assembly of Colloidal Particles. *Phys. Rev. Lett.*, 93(23):238301, December 2004. doi: 10.1103/PhysRevLett.93.238301. URL http://link.aps.org/doi/10.1103/PhysRevLett.93.238301.

[63] Ho, K. M., Chan, C. T., and Soukoulis, C. M. Existence of a photonic gap in periodic dielectric structures. *Phys. Rev. Lett.*, 65(25):3152–3155, December 1990. doi: 10.1103/PhysRevLett.65.3152. URL http://link.aps.org/doi/10.1103/PhysRevLett.65.3152.

[64] Zhang, Keys, A. S., Chen, T., and Glotzer, S. C. Self-Assembly of Patchy Particles into Diamond Structures through Molecular Mimicry. *Langmuir*, 21(25):11547–11551, December 2005. ISSN 0743-7463. doi: 10.1021/la0513611. URL http://dx.doi.org/10.1021/la0513611.

[65] Stratford, K., Adhikari, R., Pagonabarraga, I., Desplat, J.-C., and Cates, M. E. Colloidal Jamming at Interfaces: A Route to Fluid-Bicontinuous Gels. *Science*, 309(5744):2198–2201, September 2005. ISSN 0036-8075, 1095-9203. doi: 10.1126/science.1116589. URL http://www.sciencemag.org/content/309/5744/2198.

[66] Clegg, P. S., Herzig, E. M., Schofield, A. B., Egelhaaf, S. U., Horozov, T. S., Binks, B. P., Cates, M. E., and Poon, W. C. K. Emulsification of Partially Miscible Liquids Using Colloidal Particles: Nonspherical and Extended Domain Structures.

Langmuir, 23(11):5984–5994, May 2007. ISSN 0743-7463. doi: 10.1021/la063707t. URL http://dx.doi.org/10.1021/la063707t.

[67] Sanz, E., White, K. A., Clegg, P. S., and Cates, M. E. Colloidal Gels Assembled via a Temporary Interfacial Scaffold. *Phys. Rev. Lett.*, 103(25):255502, December 2009. doi: 10.1103/PhysRevLett.103.255502. URL http://link.aps.org/doi/10.1103/PhysRevLett.103.255502.

[68] McGorty, R., Fung, J., Kaz, D., and Manoharan, V. N. Colloidal self-assembly at an interface. *Materials Today*, 13(6):34–42, June 2010. ISSN 1369-7021. doi: 10.1016/S1369-7021(10)70107-3. URL http://www.sciencedirect.com/science/article/pii/S1369702110701073.

[69] Koos, E. and Willenbacher, N. Capillary Forces in Suspension Rheology. *Science*, 331(6019):897–900, February 2011. ISSN 0036-8075, 1095-9203. doi: 10.1126/science.1199243. URL http://www.sciencemag.org/content/331/6019/897.

[70] Van Kao, S., Nielsen, L. E., and Hill, C. T. Rheology of concentrated suspensions of spheres. I. Effect of the liquid—solid interface. *Journal of Colloid and Interface Science*, 53(3):358–366, December 1975. ISSN 0021-9797. doi: 10.1016/0021-9797(75)90051-X. URL http://www.sciencedirect.com/science/article/pii/002197977590051X.

[71] Kruyt, H. R. and van Selms, F. G. The influence of a third phase on the rheology of suspensions. *Recl. Trav. Chim. Pays-Bas*, 62(6):415–426, January 1943. ISSN 0165-0513. doi: 10.1002/recl.19430620612. URL http://onlinelibrary.wiley.com/doi/10.1002/recl.19430620612/abstract.

[72] Koos, E., Johannsmeier, J., Schwebler, L., and Willenbacher, N. Tuning suspension rheology using capillary forces. *Soft Matter*, 8(24):6620–6628, May 2012. ISSN 1744-6848. doi: 10.1039/C2SM25681A. URL http://pubs.rsc.org/en/content/articlelanding/2012/sm/c2sm25681a.

[73] Koos, E. and Willenbacher, N. Particle configurations and gelation in capillary suspensions. *Soft Matter*, 8(14):3988–3994, March 2012. ISSN 1744-6848. doi: 10.1039/C2SM07347A. URL http://pubs.rsc.org/en/content/articlelanding/2012/sm/c2sm07347a.

[74] Brakke, K. A. The Surface Evolver. *Experimental Mathematics*, 1(2):141–165, January 1992. ISSN 1058-6458. doi: 10.1080/10586458.1992.10504253. URL http://dx.doi.org/10.1080/10586458.1992.10504253.

[75] Danov, K. D., Kralchevsky, P. A., and Boneva, M. P. Electrodipping Force Acting on Solid Particles at a Fluid Interface. *Langmuir*, 20(15):6139–6151, 2004. ISSN 0743-7463. doi: 10.1021/la0497090. URL http://dx.doi.org/10.1021/la0497090.

[76] Paunov, V. N. On the Analogy between Lateral Capillary Interactions and Electrostatic Interactions in Colloid Systems. *Langmuir*, 14(18):5088–5097, 1998. ISSN 0743-7463. doi: 10.1021/la980389s. URL http://dx.doi.org/10.1021/la980389s.

[77] Nicolson, M. M. The interaction between floating particles. *Mathematical Proceedings of the Cambridge Philosophical Society*, 45(02):288–295, April 1949. ISSN 1469-8064. doi: 10.1017/S0305004100024841. URL http://journals.cambridge.org/article_S0305004100024841.

[78] Chan, D. Y. C., Henry jr., J. D., and White, L. R. The interaction of colloidal particles collected at fluid interfaces. *Journal of Colloid and Interface Science*, 79(2):410–418, February 1981. ISSN 0021-9797. doi: 10.1016/0021-9797(81)90092-8. URL http://www.sciencedirect.com/science/article/pii/0021979781900928.

[79] Liang, G., Zeng, Z., Chen, Y., Onishi, J., Ohashi, H., and Chen, S. Simulation of self-assemblies of colloidal particles on the substrate using a lattice Boltzmann pseudo-solid model. *Journal of Computational Physics*, 248:323–338, September 2013. ISSN 0021-9991. doi: 10.1016/j.jcp.2013.04.007. URL http://www.sciencedirect.com/science/article/pii/S0021999113002568.

[80] Shinto, H., Komiyama, D., and Higashitani, K. Lateral Capillary Forces between Solid Bodies on Liquid Surface: A Lattice Boltzmann Study. *Langmuir*, 22(5):2058–2064, 2006. ISSN 0743-7463. doi: 10.1021/la0512751. URL http://dx.doi.org/10.1021/la0512751.

[81] Onishi, J., Kawasaki, A., Chen, Y., and Ohashi, H. Lattice Boltzmann simulation of capillary interactions among colloidal particles. *Computers & Mathematics*

with Applications, 55(7):1541–1553, April 2008. ISSN 0898-1221. doi: 10.1016/j.camwa.2007.08.027. URL http://www.sciencedirect.com/science/article/pii/S0898122107006463.

[82] Vella, D. and Mahadevan, L. The "Cheerios effect". *American Journal of Physics*, 73(9):817–825, August 2005. ISSN 0002-9505, 1943-2909. doi: 10.1119/1.1898523. URL http://scitation.aip.org/content/aapt/journal/ajp/73/9/10.1119/1.1898523.

[83] Lucassen, J. Capillary forces between solid particles in fluid interfaces. *Colloids and Surfaces*, 65(2–3):131–137, August 1992. ISSN 0166-6622. doi: 10.1016/0166-6622(92)80268-7. URL http://www.sciencedirect.com/science/article/pii/0166662292802687.

[84] Ruiz-Garcia, J., Gámez-Corrales, R., and Ivlev, B. I. Foam and cluster structure formation by latex particles at the air/water interface. *Physica A: Statistical Mechanics and its Applications*, 236(1–2):97–104, February 1997. ISSN 0378-4371. doi: 10.1016/S0378-4371(96)00399-8. URL http://www.sciencedirect.com/science/article/pii/S0378437196003998.

[85] Ruiz-García, R.-G., Gámez-Corrales, R., and Ivlev, B. I. Formation of two-dimensional colloidal voids, soap froths, and clusters. *Phys. Rev. E*, 58(1):660–663, July 1998. doi: 10.1103/PhysRevE.58.660. URL http://link.aps.org/doi/10.1103/PhysRevE.58.660.

[86] Ghezzi, F. and Earnshaw, J. C. Formation of meso-structures in colloidal monolayers. *J. Phys.: Condens. Matter*, 9(37):L517, September 1997. ISSN 0953-8984. doi: 10.1088/0953-8984/9/37/004. URL http://iopscience.iop.org/0953-8984/9/37/004.

[87] Ruiz-García, R.-G. and Ivlev, B. I. Formation of colloidal clusters and chains at the air/water interface. *Molecular Physics*, 95(2):371–375, October 1998. ISSN 0026-8976. doi: 10.1080/00268979809483169. URL http://dx.doi.org/10.1080/00268979809483169.

[88] Danov, K. D., Kralchevsky, P. A., Naydenov, B. N., and Brenn, G. Interactions between particles with an undulated contact line at a fluid interface: Capillary multipoles of arbitrary order. *Journal of Colloid and Interface Science*, 287(1):

121–134, July 2005. ISSN 0021-9797. doi: 10.1016/j.jcis.2005.01.079. URL http://www.sciencedirect.com/science/article/pii/S0021979705000895.

[89] Danov, K. D. and Kralchevsky, P. A. Capillary forces between particles at a liquid interface: General theoretical approach and interactions between capillary multipoles. *Advances in Colloid and Interface Science*, 154(1–2):91–103, February 2010. ISSN 0001-8686. doi: 10.1016/j.cis.2010.01.010. URL http://www.sciencedirect.com/science/article/pii/S0001868610000242.

[90] Bowden, N., Terfort, A., Carbeck, J., and Whitesides, G. M. Self-Assembly of Mesoscale Objects into Ordered Two-Dimensional Arrays. *Science*, 276(5310):233–235, April 1997. ISSN 0036-8075, 1095-9203. doi: 10.1126/science.276.5310.233. URL http://www.sciencemag.org/content/276/5310/233.

[91] Nierop, E. A. v., Stijnman, M. A., and Hilgenfeldt, S. Shape-induced capillary interactions of colloidal particles. *EPL*, 72(4):671, November 2005. ISSN 0295-5075. doi: 10.1209/epl/i2005-10279-7. URL http://iopscience.iop.org/0295-5075/72/4/671.

[92] Israelachvili, J. N. Chapter 13 - Van der Waals Forces between Particles and Surfaces. In Israelachvili, J. N., editor, *Intermolecular and Surface Forces (Third Edition)*, pages 253–289. Academic Press, San Diego, 2011. ISBN 978-0-12-375182-9. URL http://www.sciencedirect.com/science/article/pii/B9780123751829100132.

[93] Loudet, J. C., Yodh, A. G., and Pouligny, B. Wetting and Contact Lines of Micrometer-Sized Ellipsoids. *Phys. Rev. Lett.*, 97(1):018304, July 2006. doi: 10.1103/PhysRevLett.97.018304. URL http://link.aps.org/doi/10.1103/PhysRevLett.97.018304.

[94] Lehle, H., Noruzifar, E., and Oettel, M. Ellipsoidal particles at fluid interfaces. *Eur. Phys. J. E*, 26(1-2):151–160, May 2008. ISSN 1292-8941, 1292-895X. doi: 10.1140/epje/i2007-10314-1. URL http://link.springer.com/article/10.1140/epje/i2007-10314-1.

[95] Oettel, M. and Dietrich, S. Colloidal Interactions at Fluid Interfaces†. *Langmuir*, 24(4):1425–1441, February 2008. ISSN 0743-7463. doi: 10.1021/la702794d. URL http://dx.doi.org/10.1021/la702794d.

[96] Dasgupta, S., Katava, M., Faraj, M., Auth, T., and Gompper, G. Capillary Assembly of Microscale Ellipsoidal, Cuboidal, and Spherical Particles at Interfaces. *Langmuir*, 30(40):11873–11882, October 2014. ISSN 0743-7463. doi: 10.1021/la502627h. URL http://dx.doi.org/10.1021/la502627h.

[97] Madivala, B., Fransaer, J., and Vermant, J. Self-Assembly and Rheology of Ellipsoidal Particles at Interfaces. *Langmuir*, 25(5):2718–2728, March 2009. ISSN 0743-7463. doi: 10.1021/la803554u. URL http://dx.doi.org/10.1021/la803554u.

[98] Basavaraj, M. G., Fuller, G. G., Fransaer, J., and Vermant, J. Packing, Flipping, and Buckling Transitions in Compressed Monolayers of Ellipsoidal Latex Particles. *Langmuir*, 22(15):6605–6612, July 2006. ISSN 0743-7463. doi: 10.1021/la060465o. URL http://dx.doi.org/10.1021/la060465o.

[99] Madivala, B., Vandebril, S., Fransaer, J., and Vermant, J. Exploiting particle shape in solid stabilized emulsions. *Soft Matter*, 5(8):1717–1727, April 2009. ISSN 1744-6848. doi: 10.1039/B816680C. URL http://pubs.rsc.org/en/content/articlelanding/2009/sm/b816680c.

[100] Deegan, R. D., Bakajin, O., Dupont, T. F., Huber, G., Nagel, S. R., and Witten, T. A. Capillary flow as the cause of ring stains from dried liquid drops. *Nature*, 389(6653):827–829, October 1997. ISSN 0028-0836. doi: 10.1038/39827. URL http://www.nature.com.libproxy.ucl.ac.uk/nature/journal/v389/n6653/full/389827a0.html.

[101] Yunker, P. J., Still, T., Lohr, M. A., and Yodh, A. G. Suppression of the coffee-ring effect by shape-dependent capillary interactions. *Nature*, 476(7360):308–311, August 2011. ISSN 0028-0836. doi: 10.1038/nature10344. URL http://www.nature.com/nature/journal/v476/n7360/full/nature10344.html?WT.ec_id=NATURE-20110818.

[102] Kardar, M., Parisi, G., and Zhang, Y.-C. Dynamic Scaling of Growing Interfaces. *Phys. Rev. Lett.*, 56(9):889–892, March 1986. doi: 10.1103/PhysRevLett.56.889. URL http://link.aps.org/doi/10.1103/PhysRevLett.56.889.

[103] Yunker, P. J., Lohr, M. A., Still, T., Borodin, A., Durian, D. J., and Yodh, A. G. Effects of Particle Shape on Growth Dynamics at Edges of Evaporating Drops of Colloidal Suspensions. *Phys. Rev. Lett.*, 110(3):035501, January

2013. doi: 10.1103/PhysRevLett.110.035501. URL http://link.aps.org/doi/10.1103/PhysRevLett.110.035501.

[104] Wakita, J.-i., Itoh, H., Matsuyama, T., and Matsushita, M. Self-Affinity for the Growing Interface of Bacterial Colonies. *J. Phys. Soc. Jpn.*, 66(1):67–72, January 1997. ISSN 0031-9015. doi: 10.1143/JPSJ.66.67. URL http://journals.jps.jp.libproxy.ucl.ac.uk/doi/abs/10.1143/JPSJ.66.67.

[105] Maunuksela, J., Myllys, M., Kähkönen, O.-P., Timonen, J., Provatas, N., Alava, M. J., and Ala-Nissila, T. Kinetic Roughening in Slow Combustion of Paper. *Phys. Rev. Lett.*, 79(8):1515–1518, August 1997. doi: 10.1103/PhysRevLett.79.1515. URL http://link.aps.org/doi/10.1103/PhysRevLett.79.1515.

[106] Verlet, L. Computer "Experiments" on Classical Fluids. I. Thermodynamical Properties of Lennard-Jones Molecules. *Phys. Rev.*, 159(1):98–103, July 1967. doi: 10.1103/PhysRev.159.98. URL http://link.aps.org/doi/10.1103/PhysRev.159.98.

[107] Happel, J. and Brenner, H. *Low Reynolds Number Hydrodynamics: With Special Applications to Particulate Media*. Springer Science & Business Media, September 1983. ISBN 9789024728770.

[108] Purcell, E. M. Life at low Reynolds number. *American Journal of Physics*, 45(1):3–11, January 1977. ISSN 0002-9505, 1943-2909. doi: 10.1119/1.10903. URL http://scitation.aip.org/content/aapt/journal/ajp/45/1/10.1119/1.10903.

[109] Frisch, U., Hasslacher, B., and Pomeau, Y. Lattice-Gas Automata for the Navier-Stokes Equation. *Phys. Rev. Lett.*, 56(14):1505–1508, April 1986. doi: 10.1103/PhysRevLett.56.1505. URL http://link.aps.org/doi/10.1103/PhysRevLett.56.1505.

[110] McNamara, G. R. and Zanetti, G. Use of the Boltzmann Equation to Simulate Lattice-Gas Automata. *Phys. Rev. Lett.*, 61(20):2332–2335, November 1988. doi: 10.1103/PhysRevLett.61.2332. URL http://link.aps.org/doi/10.1103/PhysRevLett.61.2332.

[111] Wolfram, S. Cellular automaton fluids 1: Basic theory. *J Stat Phys*, 45(3-4):471–526, November 1986. ISSN 0022-4715, 1572-9613. doi: 10.1007/BF01021083. URL http://link.springer.com/article/10.1007/BF01021083.

[112] Maxwell, J. C. On the Dynamical Theory of Gases. *Phil. Trans. R. Soc. Lond.*, 157:49–88, January 1867. ISSN 0261-0523,. doi: 10.1098/rstl.1867.0004. URL http://rstl.royalsocietypublishing.org/content/157/49.

[113] Higuera, F. J. and Jiménez, J. Boltzmann Approach to Lattice Gas Simulations. *EPL*, 9(7):663, August 1989. ISSN 0295-5075. doi: 10.1209/0295-5075/9/7/009. URL http://iopscience.iop.org/0295-5075/9/7/009.

[114] Higuera, F. J., Succi, S., and Benzi, R. Lattice Gas Dynamics with Enhanced Collisions. *EPL*, 9(4):345, June 1989. ISSN 0295-5075. doi: 10.1209/0295-5075/9/4/008. URL http://iopscience.iop.org/0295-5075/9/4/008.

[115] Bhatnagar, P. L., Gross, E. P., and Krook, M. A Model for Collision Processes in Gases. I. Small Amplitude Processes in Charged and Neutral One-Component Systems. *Phys. Rev.*, 94(3):511–525, May 1954. doi: 10.1103/PhysRev.94.511. URL http://link.aps.org/doi/10.1103/PhysRev.94.511.

[116] Benzi, R., Succi, S., and Vergassola, M. The lattice Boltzmann equation: theory and applications. *Physics Reports*, 222(3):145–197, December 1992. ISSN 0370-1573. doi: 10.1016/0370-1573(92)90090-M. URL http://www.sciencedirect.com/science/article/pii/037015739290090M.

[117] Qian, Y. H., D'Humières, D., and Lallemand, P. Lattice BGK Models for Navier-Stokes Equation. *EPL*, 17(6):479, February 1992. ISSN 0295-5075. doi: 10.1209/0295-5075/17/6/001. URL http://iopscience.iop.org/0295-5075/17/6/001.

[118] Chapman, S. On the Law of Distribution of Molecular Velocities, and on the Theory of Viscosity and Thermal Conduction, in a Non-Uniform Simple Monatomic Gas. *Philosophical Transactions of the Royal Society of London A: Mathematical, Physical and Engineering Sciences*, 216(538-548):279–348, January 1916. ISSN 0264-3952. doi: 10.1098/rsta.1916.0006. URL http://rsta.royalsocietypublishing.org/content/216/538-548/279.

[119] Chapman, S. On the Kinetic Theory of a Gas. Part II: A Composite Monatomic Gas: Diffusion, Viscosity, and Thermal Conduction. *Philosophical Transactions of the Royal Society of London. Series A, Containing Papers of a Mathematical or Physical Character*, 217:115–197, January 1918. ISSN 0264-3952. URL http://www.jstor.org/stable/91120.

[120] *The Mathematical Theory of Non-uniform Gases: An Account of the Kinetic Theory of Viscosity, Thermal Conduction and Diffusion in Gases*. Cambridge University Press, 1970. ISBN 9780521408448.

[121] Wolf-Gladrow, D. A. *Lattice Gas Cellular Automata and Lattice Boltzmann Models*, volume 1725 of *Lecture Notes in Mathematics*. Springer Berlin Heidelberg, Berlin, Heidelberg, 2000. ISBN 978-3-540-66973-9, 978-3-540-46586-7. URL http://link.springer.com/10.1007/b72010.

[122] Chen, S. and Doolen, G. D. Lattice Boltzmann Method for Fluid Flows. *Annual Review of Fluid Mechanics*, 30(1):329–364, 1998. doi: 10.1146/annurev.fluid.30.1.329. URL http://www.annualreviews.org/doi/abs/10.1146/annurev.fluid.30.1.329.

[123] Junk, M., Klar, A., and Luo, L.-S. Asymptotic analysis of the lattice Boltzmann equation. *Journal of Computational Physics*, 210(2):676–704, December 2005. ISSN 0021-9991. doi: 10.1016/j.jcp.2005.05.003. URL http://www.sciencedirect.com/science/article/pii/S0021999105002573.

[124] Chen, H., Chen, S., and Matthaeus, W. H. Recovery of the Navier-Stokes equations using a lattice-gas Boltzmann method. *Phys. Rev. A*, 45(8):R5339–R5342, April 1992. doi: 10.1103/PhysRevA.45.R5339. URL http://link.aps.org/doi/10.1103/PhysRevA.45.R5339.

[125] Philippi, P. C., Hegele, L. A., dos Santos, L. O. E., and Surmas, R. From the continuous to the lattice Boltzmann equation: The discretization problem and thermal models. *Phys. Rev. E*, 73(5):056702, May 2006. doi: 10.1103/PhysRevE.73.056702. URL http://link.aps.org/doi/10.1103/PhysRevE.73.056702.

[126] Chen, H., Goldhirsch, I., and Orszag, S. A. Discrete Rotational Symmetry, Moment Isotropy, and Higher Order Lattice Boltzmann Models. *J Sci Comput*, 34(1):87–112, October 2007. ISSN 0885-7474, 1573-7691. doi: 10.1007/s10915-007-9159-3. URL http://link.springer.com/article/10.1007/s10915-007-9159-3.

[127] Cornubert, R., d'Humières, D., and Levermore, D. A Knudsen layer theory for lattice gases. *Physica D: Nonlinear Phenomena*, 47(1–2):241–259, January 1991. ISSN 0167-2789. doi: 10.1016/0167-2789(91)90295-K. URL http://www.sciencedirect.com/science/article/pii/016727899190295K.

[128] Ginzbourg, I. and Adler, P. M. Boundary flow condition analysis for the three-dimensional lattice Boltzmann model. *Journal de Physique II*, 4(2):191–214, February 1994. ISSN 1155-4312, 1286-4870. doi: 10.1051/jp2:1994123. URL http://www.edpsciences.org/10.1051/jp2:1994123.

[129] Shan, X. and Chen, H. Lattice Boltzmann model for simulating flows with multiple phases and components. *Phys. Rev. E*, 47(3):1815–1819, March 1993. doi: 10.1103/PhysRevE.47.1815. URL http://link.aps.org/doi/10.1103/PhysRevE.47.1815.

[130] Shan, X. and Chen, H. Simulation of nonideal gases and liquid-gas phase transitions by the lattice Boltzmann equation. *Phys. Rev. E*, 49(4):2941–2948, April 1994. doi: 10.1103/PhysRevE.49.2941. URL http://link.aps.org/doi/10.1103/PhysRevE.49.2941.

[131] Sbragaglia, M., Benzi, R., Biferale, L., Succi, S., Sugiyama, K., and Toschi, F. Generalized lattice Boltzmann method with multirange pseudopotential. *Phys. Rev. E*, 75(2):026702, February 2007. doi: 10.1103/PhysRevE.75.026702. URL http://link.aps.org/doi/10.1103/PhysRevE.75.026702.

[132] Yuan, P. and Schaefer, L. Equations of state in a lattice Boltzmann model. *Physics of Fluids (1994-present)*, 18(4):042101, April 2006. ISSN 1070-6631, 1089-7666. doi: 10.1063/1.2187070. URL http://scitation.aip.org/content/aip/journal/pof2/18/4/10.1063/1.2187070.

[133] Sbragaglia, M. and Belardinelli, D. Interaction pressure tensor for a class of multicomponent lattice Boltzmann models. *Phys. Rev. E*, 88(1):013306, July 2013. doi: 10.1103/PhysRevE.88.013306. URL http://link.aps.org/doi/10.1103/PhysRevE.88.013306.

[134] Frijters, S., Günther, F., and Harting, J. Effects of nanoparticles and surfactant on droplets in shear flow. *Soft Matter*, 8(24):6542–6556, May 2012. ISSN 1744-6848. doi: 10.1039/C2SM25209K. URL http://pubs.rsc.org/en/content/articlelanding/2012/sm/c2sm25209k.

[135] Günther, F., Janoschek, F., Frijters, S., and Harting, J. Lattice Boltzmann simulations of anisotropic particles at liquid interfaces. *Computers & Fluids*, 80: 184–189, July 2013. ISSN 0045-7930. doi: 10.1016/j.compfluid.2012.03.020. URL http://www.sciencedirect.com/science/article/pii/S004579301200117X.

[136] Günther, F., Frijters, S., and Harting, J. Timescales of emulsion formation caused by anisotropic particles. *Soft Matter*, 10(27):4977–4989, June 2014. ISSN 1744-6848. doi: 10.1039/C3SM53186D. URL http://pubs.rsc.org/en/content/articlelanding/2014/sm/c3sm53186d.

[137] Ladd, A. J. C. Numerical simulations of particulate suspensions via a discretized Boltzmann equation. Part 1. Theoretical foundation. *Journal of Fluid Mechanics*, 271:285–309, 1994. doi: 10.1017/S0022112094001771.

[138] Ladd, A. J. C. Numerical simulations of particulate suspensions via a discretized Boltzmann equation. Part 2. Numerical results. *Journal of Fluid Mechanics*, 271: 311–339, 1994. doi: 10.1017/S0022112094001783.

[139] Aidun, C. K., Lu, Y., and Ding, E.-J. Direct analysis of particulate suspensions with inertia using the discrete Boltzmann equation. *Journal of Fluid Mechanics*, 373:287–311, October 1998. ISSN 1469-7645. doi: 10.1017/S0022112098002493. URL http://journals.cambridge.org/article_S0022112098002493.

[140] Ladd, A. J. C. and Verberg, R. Lattice-Boltzmann Simulations of Particle-Fluid Suspensions. *Journal of Statistical Physics*, 104(5-6):1191–1251, September 2001. ISSN 0022-4715, 1572-9613. doi: 10.1023/A:1010414013942. URL http://link.springer.com/article/10.1023/A%3A1010414013942.

[141] Berne, B. J. and Pechukas, P. Gaussian Model Potentials for Molecular Interactions. *The Journal of Chemical Physics*, 56(8):4213–4216, April 1972. ISSN 0021-9606, 1089-7690. doi: 10.1063/1.1677837. URL http://scitation.aip.org.libproxy.ucl.ac.uk/content/aip/journal/jcp/56/8/10.1063/1.1677837.

[142] Stratford, K., Adhikari, R., Pagonabarraga, I., and Desplat, J.-C. Lattice Boltzmann for Binary Fluids with Suspended Colloids. *J Stat Phys*, 121(1-2):163–178, October 2005. ISSN 0022-4715, 1572-9613. doi: 10.1007/s10955-005-8411-1. URL http://link.springer.com/article/10.1007/s10955-005-8411-1.

[143] Swift, M. R., Orlandini, E., Osborn, W. R., and Yeomans, J. M. Lattice Boltzmann simulations of liquid-gas and binary fluid systems. *Phys. Rev. E*, 54(5):5041–5052, November 1996. doi: 10.1103/PhysRevE.54.5041. URL http://link.aps.org/doi/10.1103/PhysRevE.54.5041.

[144] Kendon, V. M., Cates, M. E., Pagonabarraga, I., Desplat, J.-C., and Bladon, P. Inertial effects in three-dimensional spinodal decomposition of a symmetric binary fluid mixture: a lattice Boltzmann study. *Journal of Fluid Mechanics*, 440: 147–203, August 2001. ISSN 1469-7645. doi: 10.1017/S0022112001004682. URL http://journals.cambridge.org/article_S0022112001004682.

[145] Orlandini, E., Swift, M. R., and Yeomans, J. M. A Lattice Boltzmann Model of Binary-Fluid Mixtures. *EPL*, 32(6):463, November 1995. ISSN 0295-5075. doi: 10.1209/0295-5075/32/6/001. URL http://iopscience.iop.org/0295-5075/32/6/001.

[146] Nguyen, N.-Q. and Ladd, A. J. C. Lubrication corrections for lattice-Boltzmann simulations of particle suspensions. *Phys. Rev. E*, 66(4):046708, October 2002. doi: 10.1103/PhysRevE.66.046708. URL http://link.aps.org/doi/10.1103/PhysRevE.66.046708.

[147] Kim, E., Stratford, K., Adhikari, R., and Cates, M. E. Arrest of Fluid Demixing by Nanoparticles: A Computer Simulation Study. *Langmuir*, 24(13):6549–6556, July 2008. ISSN 0743-7463. doi: 10.1021/la800263n. URL http://dx.doi.org/10.1021/la800263n.

[148] Kim, E., Stratford, K., and Cates, M. E. Bijels Containing Magnetic Particles: A Simulation Study. *Langmuir*, 26(11):7928–7936, June 2010. ISSN 0743-7463. doi: 10.1021/la904809g. URL http://dx.doi.org/10.1021/la904809g.

[149] Kim, E., Stratford, K., Camp, P. J., and Cates, M. E. Hydrodynamic Interactions in Colloidal Ferrofluids: A Lattice Boltzmann Study†. *J. Phys. Chem. B*, 113

(12):3681–3693, March 2009. ISSN 1520-6106. doi: 10.1021/jp806678m. URL http://dx.doi.org/10.1021/jp806678m.

[150] Frijters, S., Günther, F., and Harting, J. Domain and droplet sizes in emulsions stabilized by colloidal particles. *Phys. Rev. E*, 90(4):042307, October 2014. doi: 10.1103/PhysRevE.90.042307. URL http://link.aps.org/doi/10.1103/PhysRevE.90.042307.

[151] Arditty, S., Whitby, C. P., Binks, B. P., Schmitt, V., and Leal-Calderon, F. Some general features of limited coalescence in solid-stabilized emulsions. *Eur. Phys. J. E*, 11(3):273–281, July 2003. ISSN 1292-8941, 1292-895X. doi: 10.1140/epje/i2003-10018-6. URL http://link.springer.com/article/10.1140/epje/i2003-10018-6.

[152] Cates, M. E., Henrich, O., Marenduzzo, D., and Stratford, K. Lattice Boltzmann simulations of liquid crystalline fluids: active gels and blue phases. *Soft Matter*, 5(20):3791–3800, October 2009. ISSN 1744-6848. doi: 10.1039/B908659P. URL http://pubs.rsc.org/en/content/articlelanding/2009/sm/b908659p.

[153] Hasimoto, H. On the periodic fundamental solutions of the Stokes equations and their application to viscous flow past a cubic array of spheres. *Journal of Fluid Mechanics*, 5(02):317–328, February 1959. ISSN 1469-7645. doi: 10.1017/S0022112059000222. URL http://journals.cambridge.org/article_S0022112059000222.

[154] Kunert, C. and Harting, J. Lattice Boltzmann simulations of liquid film drainage between smooth surfaces. *IMA J Appl Math*, page hxr001, March 2011. ISSN 0272-4960, 1464-3634. doi: 10.1093/imamat/hxr001. URL http://imamat.oxfordjournals.org/content/early/2011/03/01/imamat.hxr001.

[155] Faraudo, J. and Bresme, F. Stability of particles adsorbed at liquid/fluid interfaces: Shape effects induced by line tension. *The Journal of Chemical Physics*, 118(14):6518–6528, March 2003. ISSN 0021-9606, 1089-7690. doi: 10.1063/1.1559728. URL http://scitation.aip.org.libproxy.ucl.ac.uk/content/aip/journal/jcp/118/14/10.1063/1.1559728.

[156] Kaz, D. M., McGorty, R., Mani, M., Brenner, M. P., and Manoharan, V. N. Physical ageing of the contact line on colloidal particles at liquid interfaces. *Nat*

Mater, 11(2):138–142, February 2012. ISSN 1476-1122. doi: 10.1038/nmat3190. URL http://www.nature.com/nmat/journal/v11/n2/full/nmat3190.html.

[157] Colosqui, C. E., Morris, J. F., and Koplik, J. Colloidal Adsorption at Fluid Interfaces: Regime Crossover from Fast Relaxation to Physical Aging. *Phys. Rev. Lett.*, 111(2):028302, July 2013. doi: 10.1103/PhysRevLett.111.028302. URL http://link.aps.org/doi/10.1103/PhysRevLett.111.028302.

[158] Hidalgo-Alvarez, R. *Structure and Functional Properties of Colloidal Systems*. CRC Press, November 2009. ISBN 9781420084474.

[159] Bresme, F. Computer simulations and thermodynamics of anisotropic nanoparticles at fluid interfaces. *Eur. Phys. J. B*, 64(3-4):487–491, August 2008. ISSN 1434-6028, 1434-6036. doi: 10.1140/epjb/e2008-00032-2. URL http://link.springer.com/article/10.1140/epjb/e2008-00032-2.

[160] Lewandowski, E. P. *Directed assembly of complex shaped particles at fluid interfaces*. PhD thesis, The Johns Hopkins University, 2009. URL http://gradworks.umi.com/33/39/3339900.html.